5-2018

STRUCTURE BASED DRUG DESIGN OF HIGH AFFINITY KRAS INHIBITORS

Michael McCarthy

STRUCTURE BASED DRUG DESIGN OF HIGH AFFINITY KRAS INHIBITORS

by

Michael McCarthy, B.S., M.S.

APPROVED:

_____
Alemayehu A. Gorfe, Ph.D.
Advisory Professor

_____
John F. Hancock, M.B., B.Chir., Ph.D.

_____
John A. Putkey, Ph.D.

_____
Shane R. Cunha, Ph.D.

_____
Jeffrey T. Chang, Ph.D.

APPROVED:

_____
Dean, The University of Texas Graduate School of
Biomedical Sciences at Houston

STRUCTURE BASED DRUG DESIGN OF HIGH AFFINITY KRAS INHIBITORS

A

DISSERTATION

Presented to the Faculty of

The University of Texas

M. D. Anderson Cancer Center UTHealth

Graduate School of Biomedical Sciences

in Partial Fulfillment

of the Requirements

for the Degree of

DOCTOR OF PHILOSOPHY

by

Michael McCarthy, B.S., M.S.

Houston, Texas

May 2018

Dedication

To my loving and supportive wife and family.

Acknowledgements

I would like to thank my thesis advisor, Dr. Alex Gorfe, for his guidance and advice during my graduate work. Under his guidance I learned how to be an independent researcher and work harder to achieve more than I thought I could. I would like to thank the other members of my lab, Pri, Cynthia, Nabina, Suparna, Amit, Vinay, Zuhal, and Abdullah for their constant willingness to help me and for our many interesting and fruitful conversations.

I would like to thank my thesis committee, Drs. John Hancock, Shane Cunha, Jeff Cheng, and John Putkey, for their thoughtful comments and advice throughout my thesis work. Their input was instrumental to the success of my research. Dr. Putkey, not only gave me guidance but facilitated the research presented in this thesis. He and his lab members, particularly Dr. Xu Wang, tested some compounds in NMR experiments, generating the data described in chapter 4. They also provided KRAS and SOS to the Gorfe lab to conduct the biophysical assays presented as part of this work. I would also like to thank the members of the Hancock lab for providing their expertise, mentorship, reagents and lab space during my graduate work. I would particularly like to thank Dr. Jin Cho for teaching me the finer points of running westerns, providing me with invaluable advice and for his friendship.

I would like to acknowledge my friends and family for their ongoing support while I was completing my Ph.D. work. Particularly I would like to thank my parents for always encouraging me and believing in me. I would like to thank my sister, Stephanie, for always being available to talk and my sister, Valerie, for always providing me with comic relief. Lastly, I would like to thank my loving wife Katie for being the wind in my sails and constantly supporting and loving me no matter what.

STRUCTURE BASED DRUG DESIGN OF HIGH AFFINITY KRAS INHIBITORS

Michael McCarthy, M.S.

Advisory Professor: Alemayehu A. Gorfe, Ph.D

RAS, one of the most well characterized membrane-associated small GTPases, is a notorious oncogene with >15% of all tumors harboring RAS mutations. When RAS is mutated it becomes constitutively active sending cell growth, survival and proliferation into overdrive, which subsequently leads to cancer. Although, RAS has been aggressively targeted with drug design efforts for more than 30 years an FDA approved direct inhibitor has not yet been developed. There are three isoforms of RAS in cells; HRAS, NRAS and KRAS. We focused on KRAS since it is the most frequently mutated isoform in cancer. To identify novel non-covalent small molecules that bind to mutant KRAS, we conducted a high-throughput virtual screen of drug-like compounds against a previously characterized allosteric pocket on a molecular dynamics simulation-derived KRAS^{G12D} structure. The *in silico* predicted hits were then validated with a battery of cell-based and biophysical assays. Specifically, the hits effects on KRAS signaling, binding affinities for KRAS and mechanisms of activity were evaluated. We found two key hit compounds (i) a pyrazolopyrimidine based molecule compound **11** and (ii) a indazole based molecule compound **M1**. Compound **11** exhibited a monotonous dose-dependent inhibition of KRAS signaling, however compound **M1** demonstrated a biphasic dose-depended effect. With the potential to elucidate the structure-activity relationships between these molecules and their unique structures we tested both in cell-based and

biophysical assays. We found that compound **11** binds to KRAS with nanomolar affinity and completely abolishes CRaf binding *in vitro*, subsequently leading to a significant reduction in RAS dependent CRaf/ERK activation and son of sevenless (SOS) mediated nucleotide exchange. Moreover, treatment at low micromolar concentrations of compound **11** reduced cell proliferation in six cancer cell lines.

Further, compound **M1**, binds to KRAS in NMR-based studies and both reduced and enhanced signaling in cell-based assays as indicated by western blotting. We attributed this to **M1** enhancing and disrupting nucleotide exchange through different mechanisms. Additionally, we noted that **M1** showed remarkable selectivity towards inhibiting proliferation of MiaPaCa-2 cells.

We then screened a second small-molecule library based on **M1** and generated additional hits which decreased mutant KRAS signaling. Likewise, we generated two derivatives of compound **11** which were tested and gave insights to critical functional groups. Combining our results with detailed structural analysis, we are able to describe key ligand-receptor interactions that correlate with activity. Thus, showing that our screening techniques were very successful at generating KRAS binders that have effects on signaling in cells.

To our knowledge compound **11** is the first known nanomolar binder of KRAS that disrupts interaction with CRaf resulting in decreased p-ERK levels and cell proliferation. Therefore, compound **11** is a promising hit for the development of novel non-covalent KRAS inhibitors.

Table of Contents

List of Illustrations

List of Tables

Abbreviations

ADMET	Absorption distribution, metabolism excretion, and minimize toxicity
BHK	Baby hamster kidney
CADD	Computer aided drug design
RAF	Rapidly Accelerated Fibrosarcoma
DCAI	4,6-dichloro-2-methyl-3-aminoethyl-indole
EGFR	Epidermal growth factor receptor
ELISA	Enzyme-linked immunosorbent assays
ERK	Extarcellular signal-regulated kinase
FTI	Farnesyltransferase inhibitor
GAP	GTPase Activating Proteins
GEF	Guanine nucleotide Exchange Factors
GNP	Guanylyl imidodiphosphate
GST	Glutathione S-transferase
GTP	Guanosine triphosphate
ITC	Isothermal titration calorimetry
HSQC	Heteronuclear Single Quantum Coherence
HTVS	High throughput virtual screening
HVR	Hyper variable regions

MAPK	Mitogen-activated protein kinase
MD	Molecular dynamics
MST	Microscale thermophoresis
NAMD	Nanoscale Molecular Dynamics
NMR	Nuclear magnetic resonance spectroscopy
PFA	Paraformaldehyde
PI3K	Phosphatidylinositol-4,5-bisphosphate 3-kinase
PVDF	Polyvinylidene fluoride membrane
RICS	Raster image correlation spectroscopy
RMSD	Root-mean-square deviation
SASA	Solvent exposed surface area
SPR	Surface plasmon resonance
SOS	Son of sevenless

Chapter 1: Introduction

Portions of this chapter are reproduced with permission from the review article McCarthy M., Prakash P., Gorfe A. A., 2016 Computational allosteric ligand binding site identification on Ras proteins. *Acta Biochimica et Biophysica Sinica.*

1.1 Cancer and RAt Sarcoma (RAS)

Cancer has a major impact on public health with over 15 million Americans living with some form of the disease in 2016 and about 1,700,000 new cases of cancer diagnosed in 2017 [1]. Broadly, cancer is defined as unrestrained cell growth that becomes invasive to the organ of origin and eventually spreads to other tissues. Specifically, there are 10 hallmarks of cancer; evading the immune system, enhancing inflammation (promotes tumor growth), metastasis (spreading), angiogenesis (generating blood supply), suppressing growth restriction, genome instability, immortality (activated telomerase), altered cell metabolism, insensitivity to death signaling and enhanced proliferative and survival signaling [2]. Molecularly, cancer can be driven by the alteration of a single gene. Genes with the potential to cause cancer when mutated are referred to as oncogenes. The first oncogene was discovered in 1970 in a chicken virus, later termed *src*, and fundamentally changed our understanding of the molecular biology of cancers [3]. Then came the discovery of other major oncogenes that drive cancer. In 1982 the RAS family of genes, which were originally discovered in a virus in rats in the 1960s, was identified in human cancer cells by their ability to transform mouse fibroblasts [4; 5]. Since their discovery, the RAS family of genes has been one of the most widely studied genes for their role as a driver of cancer in a variety of different types of tumors [6].

1.1.1 RAS proteins overview

RAS is a membrane-anchored 21 kDa guanosine triphosphate (GTP) binding protein, which transduces extracellular signals from trans-membrane receptors, such as the epidermal growth factor receptor (EGFR), to numerous downstream effectors thereby activating cell growth, survival and proliferation. RAS is oncogenic when mutations render it constitutively active [6-8]. There are three major RAS proteins in humans: N-, H- and KRAS and all share essentially the same catalytic machinery, but a divergent C-terminal hyper variable region (HVR). RAS is a globular protein with a catalytic domain that consists of 5 α-helices, a 6 strand β-sheet and 10 loops. The HVR of KRAS contains a polybasic stretch of 6 lysines, and is post-translationally modified at a putative CAAX box to attach a farnesyl group. Both the polybasic domain and the farnesylated domain play a critical role in anchoring and localization of KRAS to the cytosolic side of the plasma membrane [9-11]. Once localized, KRAS functions as a switch cycling between two states; GTP-active and GDP-inactive [12]. When GTP bound, KRAS exists in two conformational states either an active state with high affinity for effectors or an inactive state with low affinity for effectors. GTPase Activating Proteins (GAP) facilitate the hydrolysis of GTP to GDP, which stops KRAS signaling [13]. Guanine nucleotide Exchange Factors (GEF) such as son of sevenless (SOS) catalyzes nucleotide exchange by causing conformational changes in the switches that allows GDP to dissociate from RAS, so that another GTP molecule can bind [14]. When active, KRAS binds to effectors and triggers the auto-phosphorylation of effectors, such as Rapidly Accelerated Fibrosarcoma (CRaf) in the mitogen-activated protein kinase (MAPK)-extracellular signal-regulated kinase (ERK) pathway or phosphatidylinositol-4,5-

bisphosphate 3-kinase (PI3K) in the PI3K/AKT (protein kinase B) pathway, activating them [15-17]. Therefore, Ras plays an integral role in many cellular processes that range from development and differentiation to calcium regulation and apoptosis [11; 18].

1.1.2 RAS isoforms in cancer

Activating somatic mutations in RAS proteins occur in >15% of all human tumors [19]. However, the three RAS isoforms also differ in their ability to drive cancer formation [20]. KRAS mutations represent ~84% of all oncogenic RAS mutations and are frequently found in lung, colorectal, and pancreatic carcinomas [21-24]. NRAS mutations are common in melanomas, hepatocellular carcinomas, and hematologic malignancies [25-27]. Although less frequent, HRAS mutations are found in bladder, kidney, and thyroid carcinomas [19; 28; 29]. Frequently mutated residues of RAS are G12 and G13 in the phosphate binding loop (p-loop). Mutations at these positions in the p-loop inhibit the function of GTPase-activating proteins (GAPs), such as p120 GAP [30]. Common examples include G to D, G to V or G to A mutations, which block R789 of GAP proteins from being inserted into the nucleotide binding pocket, a requirement of GAP catalyzed GTP hydrolysis [31; 32]. Another common site for activating mutations is amino acid Q61, which also inhibits GAP activity [32]. In either case RAS becomes constitutively active and drives cell signaling, subsequently resulting in cancer. Therefore, RAS proteins remain one of the most crucial anti-cancer drug targets [33].

1.1.3: Towards inhibiting KRAS signaling

Over the years, a number of different approaches have been used to inhibit KRAS. These include indirectly perturbing membrane binding of KRAS, thereby blocking the

activity of KRAS, and inhibiting downstream effectors directly [34-37]. Examples of the former include development of farnesyltransferase inhibitors (FTIs) [38-41] and farnesyl analogues [42-44], compounds that modulate plasma membrane lipid distribution [45-47], as well as inhibition of trafficking proteins responsible for localizing KRAS on membranes, such as PDEδ [48; 49]. The goal is to disrupt KRAS membrane binding, which is required for its biological activity. While the impact of the latter three classes of compounds is yet to be determined, FTIs turned out to be a major disappointment [50]. This is because KRAS and NRAS can be alternately prenylated by geranyl-geranyl transferase, thus bypassing FTI treatment [51], and combination therapy with multiple prenylation inhibitors led to severe toxicity [40]. Some success has been achieved in inhibiting BRaf, a downstream effector of RAS, with sorafenib, vemurafenib [52] and dabrafenib [53], and MEK with trametinib, which treats some forms of melanoma and renal cancer [54]. However, in some studies inhibition of BRaf has also led to a paradoxical activation of the RAS signaling pathway by enhancing heterodimerization between CRaf and BRaf at therapeutically relevant concentrations. However, efforts are still ongoing to inhibit other MEK and ERK related pathways [55].

1.1.4: KRAS as a druggable target

Studies have shown that inhibition of KRAS signaling can cause mutant KRAS dependent tumors to shrink, making it an attractive drug target [56]. The nucleotide-binding site would have been a logical target for structure-based ligand design for KRAS. However, that ligand binding pocket is conserved in other families of GTPases and therefore targeting that site would likely lead to problems of selectivity and toxicity. Although there are ongoing efforts toward developing GDP analogues for covalent

binding to KRAS[G12C] [57; 58], such an inhibitor would not be applicable to the majority of oncogenic KRAS mutations since the other mutated residues cannot covalently bind small molecules [59]. Even if selective inhibitors of the active site were identified, the high intracellular concentrations of GTP and GDP and their high (picomolar) affinity for KRAS would make competitive inhibition impractical [31]. Further, it is apparent in many crystal structures that KRAS has a surface that is relatively smooth and without obvious allosteric pockets to target, thus it has proven to be a challenging target. Alternative strategies are needed to target abnormal RAS function.

1.2 Discovery and validation of four allosteric binding sites on RAS

In the recent past our group [60-63] as well as others [64-70] demonstrated that RAS is an allosteric enzyme with multiple surface pockets, which opened up a promising new direction towards inhibiting RAS directly (see [71; 72] for recent reviews). These discoveries were significantly facilitated by computational methods [60; 61], which provided the initial clues into the potential "druggability" of RAS [20]. This conceptual advance led to the prediction of four allosteric ligand binding sites based on different computational approaches, primarily ensemble-based blind docking and FTMap [70; 73]. The ensemble-based approach accounts for RAS flexibility and conformational transitions using molecular dynamics (MD) sampling of configurational space, followed by blind docking of drug-like molecules on the entire surface of each receptor conformation to search for allosteric binding sites. FTMap uses a continuum approach for docking of molecular fragments on the surface of a rigid receptor [74].

The four allosteric ligand binding sites predicted by these methods were subsequently confirmed by NMR or X-ray crystal structures of RAS in complex with

small-molecule ligands [64; 67; 75-78]. These ligands either interfere with GDP-GTP exchange [64; 68; 69], stabilize the inactive GTP-bound conformation of RAS (state 1) [66; 67] or prevent RAS-effector interaction [68] (**Figure 1.1**) [79-81]. While many small molecules that bind KRAS have been identified, so far none have been FDA approved. **Table 1.1** and **Figure 1.2** summarize the location of these pockets and the ligands that have been determined or predicted to bind to them. Because all of these sites have been discussed in detail in previous reports [64; 67; 75-78], I provided only a brief summary of their key features that will facilitate future drug design. It is important to note here that most of these ligands were discovered through *in silico* screening of ligand libraries [68] or via nuclear magnetic resonance spectroscopy (NMR)-based screening of molecular fragments [64; 66; 67].
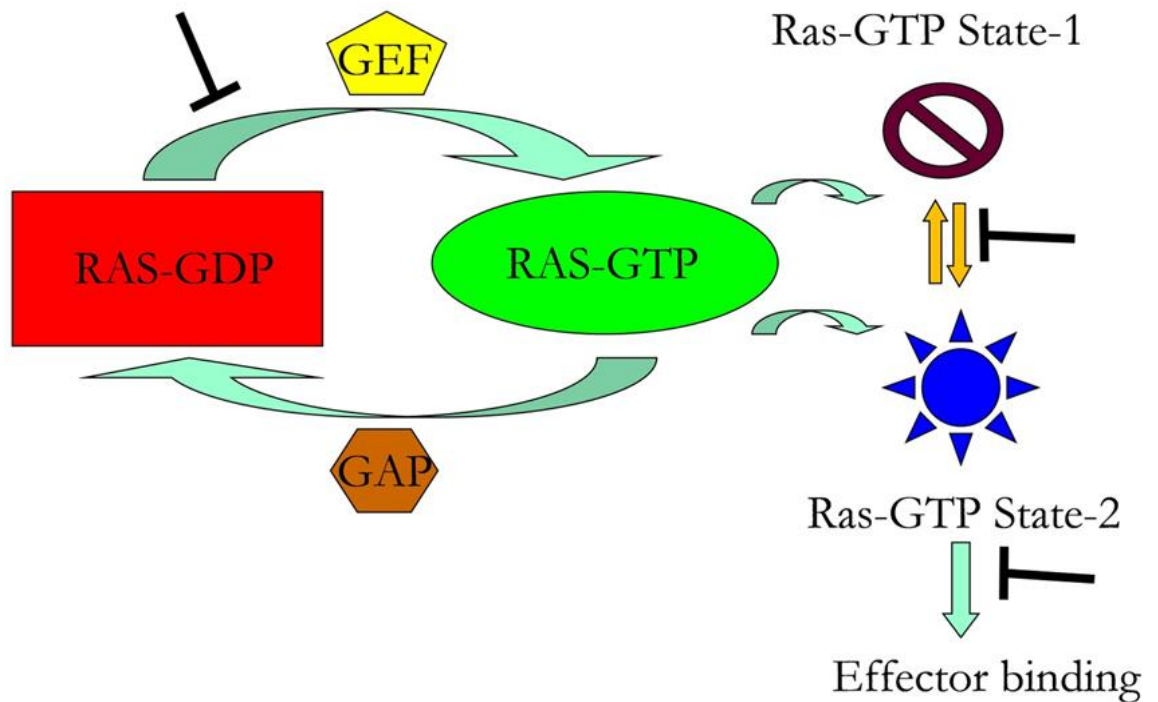
Figure 1.1: Modulation of the GTPase cycle and effector interaction of RAS by weak allosteric inhibitors that have been discovered in the past several years. The catalytic cycle of RAS (left) and the two substates of GTP-bound RAS (right) are highlighted in cartoon diagram. The inverted T sign indicates the site of action of different ligands. GEF, guanine nucleotide exchange factor; GAP, G-protein activating protein.

Three of the four pockets (p1, p2, and p4) are located near the functionally critical switch regions. Since the switch regions interact with RAS activators and effectors, ligands that target any of these pockets can be expected to directly or allosterically modulate binding to proteins either upstream or downstream of RAS. This is indeed the case [64; 67; 75-77; 82]. As indicated in Table 1, residues on switch 2 and the $\beta1$–3 strands were shown to be involved in stabilizing ligands bound to p1 [64; 75; 77], and p1 is the target site for the majority of NMR and X-ray structures of RAS-ligand complexes solved to date. These include 4,6-dichloro-2-methyl-3-aminoethyl-indole (DCAI) [64], the Kobe-family ligands [75], and other ligands with specific chemotypes including indoles, phenols, sulfonamides, and their analogs [77]. Crystal structures of ligands bound to p2 (broadly defined) that form a covalent bond to the Cys of a G12C mutant RAS have been solved recently [78]. These ligands span either of two subpockets lying toward switch 2 or α-helix 3. Evidence from NMR and MD studies suggest that p4 is a viable drug target in RAS structures with open switch 1 conformation [67; 82]. Finally, pocket p3, which has been shown to be targeted by metal-cyclens, is unique in terms of its distant location from the active site as it lies near the C-terminal end of the protein [67; 76]. Therefore, it is likely to be more significantly affected by membrane binding.

Table 1.1: Binding sites/pockets of RAS characterized by experimental and computational studies.

Binding site	Region	Ligand
p1	β1–3, switch 2	DCAI [42], Kobe ligands [46], indole, phenol, sulfonamide-containing ligands [47]
p2	Loop2, switch 2, and helix 3	Compounds specific for G12C Ras [43]
p3	Loop7 and helix 5	M^{2+}-BPA [45], M^{2+}-cyclen [44]
p4	switch 1	M^{2+}-BPA [45], Andrographolide derivatives [39]
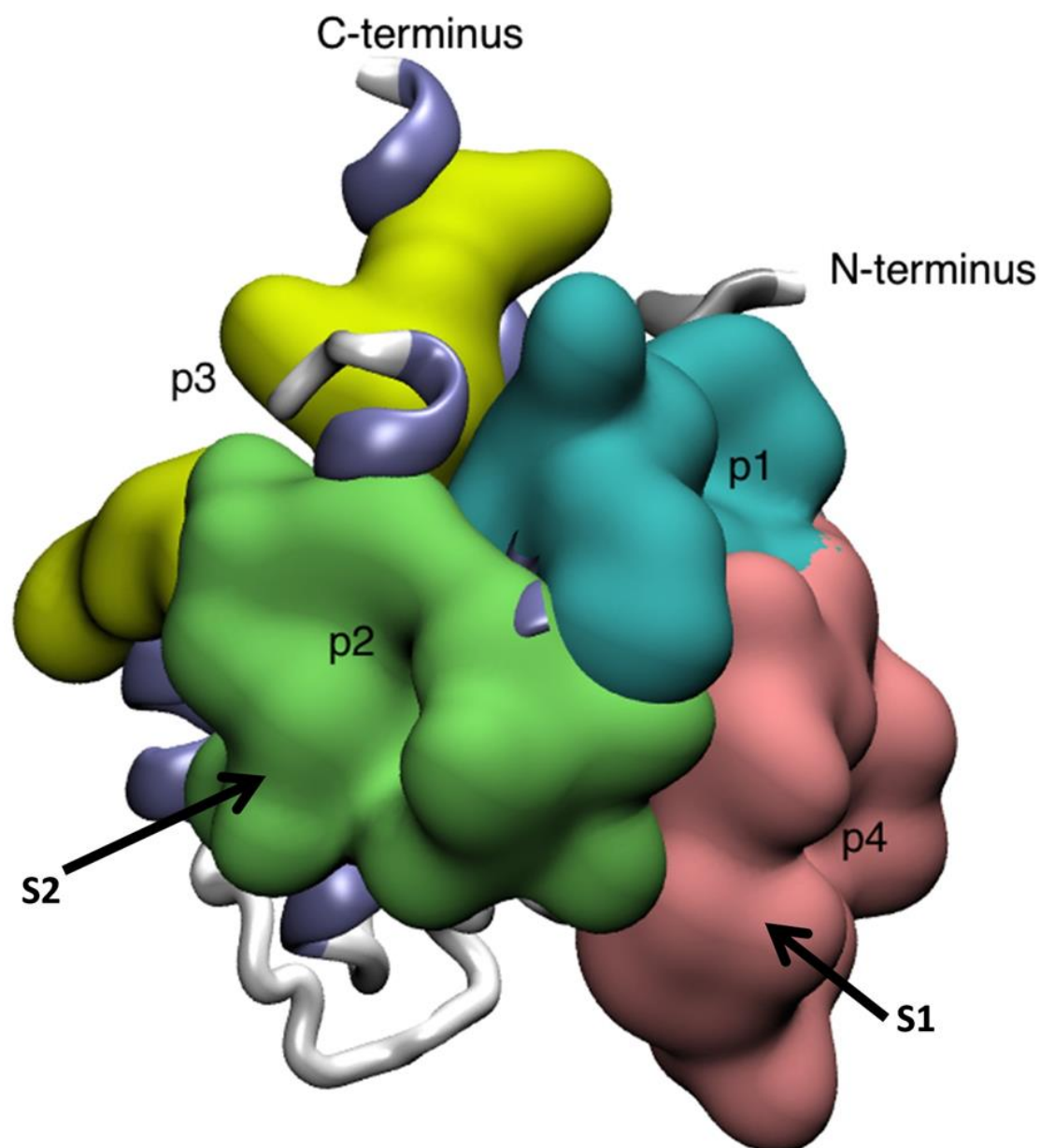
Figure 1.2: The location of allosteric ligand binding sites on RAS. Four ligand binding sites are shown in different colors and labeled as p1 (light blue), p2 (green), p3 (yellow), and p4 (pink). The residues that define these pockets are listed in [83]. Note that in this illustration I used a single structure of KRAS^{G12D} in which some of the pockets are not fully open. As discussed in the main text, opening of some pockets in RAS requires relaxing the protein through MD simulation.

1.3 Computational approaches to target RAS

Given the involvement of mutant RAS in almost every cancer type, the need for discovering drugs that inhibit activated RAS signaling cannot be overstated. Drug discovery, however, is a very complex and expensive process that takes years and costs billions of dollars [84]. Structure-based computer aided drug design (CADD) approaches can expedite the process and reduce cost [85]. As a result, high throughput virtual screening (HTVS) of ligand libraries has become an integral part of drug design programs in both industry and academic laboratories [86; 87]. A major focus of this thesis is the high throughput virtual screen we conducted to search for direct inhibitors of KRAS. In this section I begin with a general overview of structure-based computer aided drug discovery. I then discuss the four allosteric ligand binding sites obtained from computational and experimental studies, followed by rigorus biophysical and *in vitro* characterization of hits obtain in the HTVS.

1.3.1: Structure-based computer aided drug design (CADD)

The CADD workflow used for this thesis is shown below in **Figure 1.3**. One of the key starting points for CADD is a well-characterized target whose atomic structure has been determined to a sufficiently high resolution [88]. KRAS meets this condition with more than 70 high resolution crystal structures available in the protein data bank. Also of key importance is knowledge about the potential drug binding site or pocket(s) on the surface of the target [89; 90]. In most cases, the target site for docking is the functionally most responsive orthosteric site, which, for example, can be the active site of an enzyme [91] or the agonist/antagonist-binding site of a G-protein coupled receptor. In some cases, active site inhibition is either ineffective or leads to toxicity if the site is highly

conserved among related proteins. For such targets allosteric inhibition is the preferred (or only) option to achieve enhanced selectivity or reduced toxicity. Moreover, some of the most effective drugs on the market are allosteric inhibitors (e.g., Gleevec [92]). The first crucial step for a successful structure-based discovery of an allosteric inhibitor is identification of an allosteric ligand-binding site [93].

1.3.2: High-throughput virtual screening

After target selection and binding site identification, one can conduct HTVS of ligand libraries against the target site. There are a number of knowledge-based and/or physics-based algorithms to perform HTVS using various energy functions for docking and scoring. Many excellent reviews have discussed current HTVS techniques as well as their advantages, limitations and potential for improvements [85; 87; 94; 95]. In short, HTVS requires careful selection of small molecule ligand libraries [96], which involves among other things setting up criteria for molecular size, solubility and cell permeability [97-99]. There is a wealth of data on small molecule ligands in public databases such as ZINC [100] and PubChem [101]. These depositories of large numbers of drug-like small molecules provide ready-to-use, downloadable files of ligand libraries [87; 101]. A focused library biased toward a given set of compounds can also be generated based on known high affinity binders via similarity searches and knowledge-based culling [87]. Once the desired ligand library is chosen, HTVS can be conducted using a number of programs such as GLIDE, DOCK and AutoDock4 [102-112] (**Figure 1.3**). The output of these algorithms includes docking scores (typically based on an estimate of the binding free energy) and the structure of the predicted target-ligand complex. The final result is a list of predicted hits ranked by binding free energy score, ligand pose, or both. It is

often useful to obtain a consensus score from multiple docking runs and different programs to reduce false positives that usually arise from limitations in the scoring functions [113; 114]. The predicted hits can then be validated by experimental methods. If desired, promising hits can then be subjected to a series of optimization steps to generate a lead compound with the desired potency and selectivity (**Figure 1.3**).
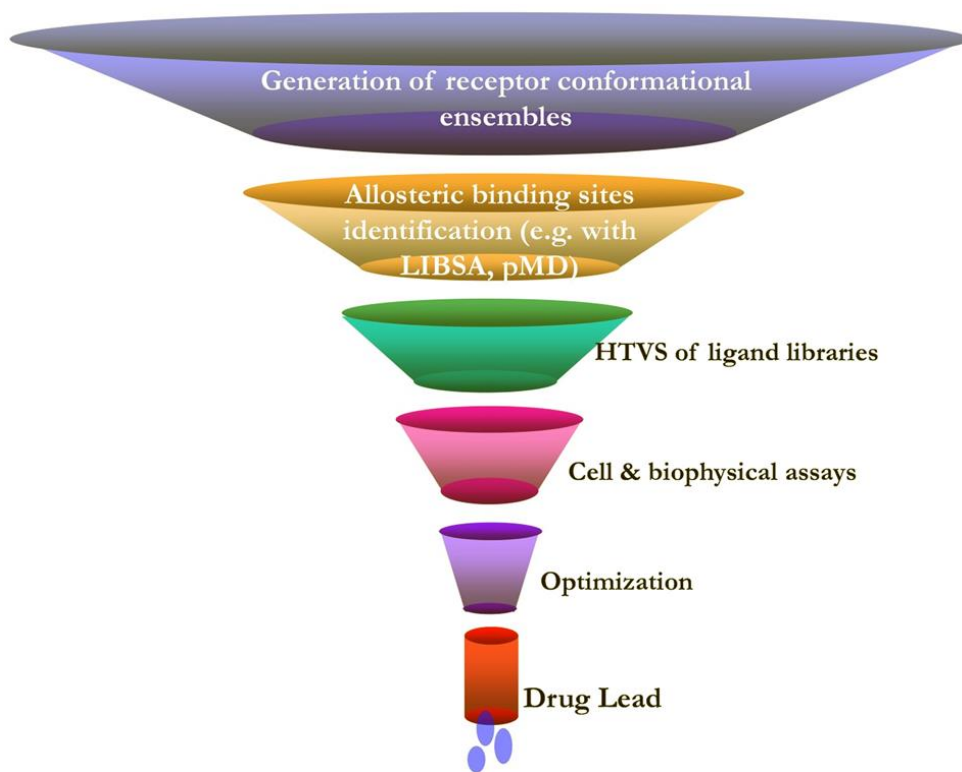
Figure 1.3: Overview of computer-aided drug design strategy used for this thesis. Shown here is a simplified workflow of a structure-based computer-aided drug design process involving target selection, binding site identification, high-throughput virtual screening of ligand libraries, experimental validation, and optimization for potency and selectivity.

1.3.3 After the screen; experimentally validating hits.

Validating hits generated by the HTVS is not an easy task but there are many biological, biochemical and biophysical approaches. Biophysical approaches when considering targets like KRAS can include microscale thermophoresis (MST), isothermal calorimetry (ITC), nuclear magnetic resonance (NMR), surface plasmon resonance (SPR), X-ray crystallography, nucleotide exchange assays, fluorescence polarization assays and fluoresence lifetime imaging (FLIM) combined with Forester resonance energy transfer (FRET), among many other techniques. For MST, ITC, NMR and SPR, binding can be monitored in real time by detecting changes in the target state following small molecule addition to the solution such as diffusion in MST or resonance shifts in SPR. The data is analyzed to confirm the significance of the changes and binding affinity can be calculated for MST, ITC and SPR. The advantage of these techniques is their simplicity, typically the protein and the molecule being tested are the only two components causing a change, thus simplifying data interpretation. For X-ray crystallography the protein is crystalized with or without the compound. If the protein will not crystalize with the compound, the crystal can be soaked in a solution with the compound, which could allow for binding. After the crystal is subject to intense X-rays, detailed structural information of the protein and ligand complex can be obtained by analyzing the X-ray scattering data. Fluorescence based assays such as nucleotide exchange or fluorescence polarization can involve endogenous ligands that are modified to fluoresce. Typically, these assays monitor a change in fluorescence which is attributed to the molecule disrupting protein-protein interactions or protein-ligand binding. Although these assays can be ambiguous by indicating multiple targets for binding, they usually require less expensive equipment and are less difficult to conduct compared to crystallography. The advantage of FLIM-

FRET assay is that they assess binding and disruption of protein-protein interactions in the native cellular environment. With KRAS and RAF as an example, a donor fluorophore can be attached to KRAS and an acceptor to RAF, such as GFP and RFP respectively. When KRAS and RAF interact the fluorescence emission lifetime of GFP will change. If the molecule disrupts that interaction that too will have an effect on the emission lifetime of GFP [115].

For biochemical experiments, alteration of the signal transduction pathway can be assessed. For KRAS disruption of effector binding can be measured by quantitative western blotting using antibodies to the activated downstream proteins, i.e. phospho-ERK and phospho-AKT.

Disruption or enhancement of protein-protein interactions can be assessed with pulldown assays. For example, I measured KRAS precipitation by a Glutathione S-Transferase (GST) fusion construct of the Ras Binding Domain (RBD) of RAF. Hit molecules can be tested in these assays to determine if the compounds will interfere with protein-protein interaction.

Alternatively, disruption of signaling for KRAS can be evaluated by enzyme-linked immunosorbent assays (ELISA). Such assays offer high throughput detection of total and phosphorylated ERK levels using common 96-well plate setup and readers. Other similar calorimetry assays such as MTT (detects cell metabolism) and the CyQuant cell proliferation assay (detects DNA content) can indicated changes to cell proliferation due to treatment with hit compounds. Finally, xenograft animal models can be used to test absorption, distribution, metabolism, excretion, and toxicity (ADMET) as well as effect of hit molecules on tumors in live animals. These are a few of the many techniques and assays available to thoroughly validate the hits generated *in silico*.

1.3.4: Summary of goals of this study

In summary, unregulated signaling from mutant KRAS can drive cancer tumor formation; therefore, abrogating constitutively active KRAS signaling could have a significant impact in many types of cancer. Previously, KRAS was considered an "undruggable" target and to-date the FDA has not approved any compounds to target KRAS in cancer. Thus, the goal of my thesis work was to identify "drug-like" small molecules that abrogate oncogenic $KRAS^{G12D}$ signaling [5]. To accomplish this, we combined an HTVS, biophysical assays and cell-based assays. First, ligand libraries containing millions of compounds were screened *in silico* against a carefully selected MD derived $KRAS^{G12D}$ conformation to identify potential hits. Next, cell-based assays were used to determine the effect of the ligands on $KRAS^{G12D}$ signaling. Finally, biophysical assays such as microscale thermophoresis (MST), nuclear magnetic resonance (NMR) and fluorescence polarization were utilized to evaluate effects of binding to KRAS and determine affinity of the molecules for KRAS.

We found five molecules that bind to KRAS and alter its interaction with effector proteins to change signaling output. Of particular interest is a pyrazolopyrimidine based molecule, compound **11**, which bound to KRAS with nanomolar affinity and completely abolished CRAF binding *in vitro*, subsequently leading to a significant reduction in RAS dependent CRAF/ERK activation and both intrinsic and SOS-mediated nucleotide exchange. Moreover, treatment at low micromolar concentrations of compound **11** reduced cell proliferation in five cancer cell lines. This work has laid a strong foundation for developing a therapeutic RAS inhibitor.

Chapter 2: Materials and Methods

2.1 High throughput virtual screen

The core of this project is a high throughput virtual screen of drug-like molecules through an experimentally validate allosteric pocket on KRAS. We started with molecular dynamics simulations to generate pocket conformations that were not available in KRAS crystal structures. This allowed us to search a wider range of molecules in terms of size and combinations of chemical group moieties. Therefore, this project had the potential to identify drug-like small molecules that had new features and more potential as viable leads.

2.1.1 Molecular dynamics simulation

Oncogenic KRAS mutants are constitutively active because their ability to hydrolyze GTP is compromised [116; 117]. An inhibitor that selectively targets GTP-bound mutant KRAS would therefore be desirable. However, there was no high-resolution experimental structure of GTP-bound KRAS (^{GTP}KRAS) when we started this project, and our target pocket p1 (**Figure 1.2**) was closed in the available GDP-bound KRAS (^{GDP}KRAS) structures. Therefore, we used molecular dynamics (MD) simulation to generate an ensemble of ^{GTP}KRAS structures. The initial structure for the simulation was a GDP-bound KRAS^{G12D} X-ray structure from the PDB (ID 4DSO) [118]. Before initiating the simulation, we made the following changes to prepared the system for KRAS^{G12D}: converted GDP to GTP, remove other molecules (i.e. benzamidine), except crystal waters, and added hydrogen atoms and solvent. After minimization and a

restrained simulation, we conducted a 300 ns production run using an identical protocol to that described in a recent report [119]. The trajectory was analyzed in terms of volume and other features of our target pocket p1 and the conformation with the most open p1 was selected for virtual screening of ligand libraries.

2.1.2 Docking

For this project molecules from the ZINC database were used. ZINC is a free resource that contains over 30 million "drug-like" molecules most of which are commercially available. The molecules in ZINC are downloadable in ready-to-dock 3D formats [120]. The philosophy behind the small molecules selected was that they fit Lipinski's criteria, which is suggested to be optimal for ADMET [97]. The HTVS used the ligand library called "drugs_now" in the ZINC database, from which we docked over 6 million commercially available compounds. With help from John Rogers, a summer student in our lab, all compounds were docked on an MD derived KRAS^{G12D} conformation. We chose pocket 1 which is located between the central beta sheet and switch 2. The residues that compose this pocket (residues 5-7, 37, 39, 50-56, 67 and 70-75) are vital to KRAS effector function. Specifically, residues 37, 38, 39, 41, 54 are important for interactions with downstream effectors, such as RAF and PI3K, while residues 36, 37, 38, 67 and 70 are important for interactions with GEFs, such as SOS [121]. Therefore, a molecule that binds to this pocket could disrupt the ability of KRAS to interact with a putative GEF or some direct effectors.

As a first run these compounds were docked by AutoDock4 v4.0.1 which was implement by DOVIS to run in parallel on our in-house cluster [122]. The AutoDock4 parameters used were 1 million energy evaluations with 150 generations with Lamarkian

genetic algorithm option. AutoDock Tools was used to add Gasteiger charges and assign atomic radii, and we docked with a flexible ligand but a rigid receptor and the gird spacing was set to 1 Å. These parameters allow us to dock around 60,000 molecule a day on 10 nodes. The molecules that scored over ΔG = -6.8 kcal/mol were re-screened with VINA [123]. Out of 6 million compounds 3,762 scored in that criteria or higher. For the VINA screen the exhaustiveness setting was 12 and an energy range setting was 4. I then quantified 8 ligand receptor interactions with a python script developed by Durant *et al.* [124]. The script evaluates the following interaction with the corresponding parameters:

Close contacts between ligand and receptor. Cutoff = 2.5Å

Contacts between ligand and receptor. Cutoff = 4.0Å

H-Bonds between ligand and receptor. Cutoff = 3.2 Å : Angle = 30.0

Salt bridges between ligand and receptor. Cutoff = 5.5 Å

Cation-pi interaction between ligand and receptor = 4.0 Å

Pi-pi interaction between ligand and receptor pi-padding = 0.75 Å : Angle tolerance 30.0

T-Stacking interaction between ligand and receptor. Closest dist cutoff = 5.0 Å : Angle = 30.0

Hydrophobic interactions between ligand and receptor. Dist-cutoff = 4.0 Å

2.2 Cell-based screen

At the start of this project we did not have a cell model that contained KRAS[G12D]. However, Dr. Cho in the Hancock lab at the time, had previously established a GFP-KRAS[G12V]-expressing baby hamster kidney (BHK) cell-line. Using a standard PCR-

based mutagenesis protocol, we changed the 12V to 12D and then confirmed the mutation by sequencing. We used the new construct to establish a KRAS[G12D]-expressing BHK cell line.

2.2.1 BHK cell line general transfection protocol

BHK cells were transfected with PEF6 plasmids containing GFP-KRAS[G12D]. 2.0×10^5 BHK cells were seeded onto a 6-well plate. In tubes 160 μL OptiMEM + 1 μg mGFP-KRAS[G12D] were mixed and then 163 μL of OptiMEM + Lipofectamine at a ratio of 1 : 20 was added. The tubes were then incubated for 20 min at room temperature. After washing the cells with PBS x 1 and OptiMEM x 1,1.28 ml of OptiMEM was applied to each well. Following incubation, the contents of each tube was applied to each well one drop at a time and then the plate was gently rocked to mix. The media was changed after a ~3 h incubation. The cells were then incubated at 37 °C and checked the next day.

2.2.2 Generating monoclonal cell line

Stably transfected polyclonal BHK cells were trypsinized (trypsin 0.05 %) for 2 min, separated by pipetting 20 x, washed by centrifuging for 5 min at 1,000 rpm, aspirating the old media and then resuspended in fresh media. The cells were then counted with trypan blue and the Countess cell counter (Invitrogen[TM]). The cells were then diluted to a concentration of 1 cell per 100 μl and plated in 96 well plates with 100 μl of cell suspension per well.   This resulted in approximately 1 cell per well and 4 plates were setup similarly. As the cells grew they were monitored visually with microscopy. Any wells with more than one colony were marked and discarded. The cells that contained only one colony were selected with a maximum of 5 wells per plate. When

cells reached confluency, the colonies transferred to larger wells for expansion. Colonies that displayed obvious changes in morphology or loss of GFP were discarded. Once the cells expanded to a T75 flask they were checked with confocal microscopy to assess morphology and GFP expression level. The cells were ranked qualitatively and the best colonies were expanded to save stocks for future experiments.

2.2.3 Making cell aliquots or cell stocks

The freezing media contained 10 % FBS and 10 % DMSO v/v in Dulbecco's Modified Eagle Medium (DMEM, Hyclone^{TM}). The media was filtered with a 0.2 micron filter to ensure sterility. The cells were then trypsinized with 2 ml of trypsin for 2 min and then 2 ml of fresh normal media was and cells were separated as described previously. The cells were centrifuged at 1,000 rpm for 5 min at room temperature to pellet and the media was carefully aspirated. Finally, the cells were resuspended in freezing media, ~15 ml. The cells were vortexed briefly to mix and 1 ml was aliquoted to each cryo-tube. The cells were frozen at -80 °C overnight and then transferred to liquid nitrogen for long term preservation.

2.3 Westerns

Two different methods were used to prepare samples for western blotting. During the initial compound screen, a quick method was used that did not involve measuring protein concentrations. After treatment with compound, cells were harvested in lysis buffer, containing 50 mM Tris-HCL, pH 7.5, 5 mM $MgCl_2$, 25 mM NaF, EGTA, 1% Nonidet P40 and Leuceptin, NaVO4, DTT and Aprotinin. To harvest cells, the media was aspirated and cells were washed with cold 1 x PBS three times. Lysis buffer was added

and cells were scraped off the plate. Before scraping a new well, the scrapper was washed with Milli-Q purified water. While keeping everything on ice the lysis buffer - cell suspension was transferred to an Eppendorf tube. To lyse the cells, the tubes were twice vortexed for 10 sec with 5 min rest on ice in between vortexing. To collect the cell lysate, the tubes were centrifuged in the cold room for 5 min at max speed (~14,000 rpm). The supernatant was transferred to a new tube and the cell pellet was discarded.

To prepare western samples, during the cell-based screen, 3 µl of 5 x sample buffer was added to 10 µl of each sample of cell lysate for a total of 13 µl. Each sample was mixed and then centrifuged at max speed for 3 sec. The samples were heat denatured for 5 mins at 95 °C. Then samples were resolved with a precast Bio-Rad polyacrylamide 10 % Tris-HCl gel at 80 mV for approximately 2 h and then transferred to a polyvinylidene fluoride (PVDF) membrane.

To prepare the membranes for transfer, the first step is to hydrate them by briefly soaking in methanol (~10 sec) and then they are transferred to 1 x transfer buffer to incubate under constant agitation until needed. Once the gel is out of the apparatus, it can be cut if needed (to use one gel with two different antibodies for detection). It is then washed with 1 x transfer buffer before placing it on the membrane. To prepare the gel for transfer a cassette of membrane, gel and filter paper is made in the following order from the anode up: filter paper, hydrated membrane, gel, filter paper and then cathode. Finally, the Bio-Rad semi-dry transfer system would run at 15 mV for 30 min per gel.

After the transfer was complete, the membrane was transferred to 6 ml of blocking solution which was either 5 % BSA or Milk and incubated under constant agitation for 1 h. After blocking, the membranes were incubated with primary antibody overnight at 4°C, again with agitation. Membranes were then washed in 1 x TBST, for 5 min in triplicate

and then the secondary antibody solution was added for a minimum 1 h incubation at room temperature.

For developing the membranes, enhanced chemiluminescence (ECL) was used. 1.6 ml of component 1 and the same volume of component 2 was added to the membrane. If needed, equal volumes (100 – 400 µl) of Dura ECL enhancer was also added. The solutions and membrane are then mixed and incubated under constant rocking for 5 minutes before imaging the membrane. Images were taken on the Bio-Rad Gel-Doc^{TM} XR+ system. After developing the membranes, equal loading of protein was checked by staining with Coomassie Blue. However, in later experiment either actin, GST or GFP was used as a loading control.

After the initial screen, a standard BCA protein assay was used to determine the protein concentration of each sample before running the western. The protein assay for each sample and standard curve was prepared and analyzed using standard protocols. For subsequent western blots preparations of ~15 µg of protein (adjusted depending on total protein recovery), 5 x sample buffer, and H_2O for a final volume of 20 µl per well, were produced.

For immunoblots I used the following antibodies pan-AKT (2920S), GFP (2956S), pAKT^{S473} (4060L), p-cRaf^{S338} (9427S), p-ERK$^{T202/Y204}$ (4370L), ERK1/2 (4695S) or β-actin antibodies (Cell Signaling Technology). The IC$_{50}$ values calculated from dose-response data described in the text were calculated with Prism 4-parameter fit.

2.4 FRET experiments

To determine if compounds disrupt the interaction between KRAS^{G12D} and CRaf we conducted FLIM-FRET experiments with FRET pairs GFP-KRAS^{G12D} and RFP-CRaf.

The cells plated on coverslips were transfected with GFP-KRAS^{G12D} and full-length RFP-CRAF^{WT} then treated with indicated concentrations of compound for indicated incubation durations in serum free media. Then the cells were fixed and imaged with the Lambert FLIM-FRET microscope. To fix cells for FRET the following reagents were gathered: cold 1 x PBS, and paraformaldehyde (PFA) (made from 16 % PFA stock that was diluted 1 : 4 with 1X PBS).

To fix the cells, first they were washed twice with cold PBS (2 ml per well for 6 well plate, 1 ml for 12 well plate). Then ~1.2 ml of 4% PFA was added and incubated for 30 min in the dark. The PFA was collected and cell were washed 2 ml PBS twice. Next, the cells were incubated for 10 min with ~1.2 ml of 50 mM ammonium chloride (NH$_4$Cl). The NH$_4$Cl will quench the autofluorescence of the PFA.

To mount the coverslips on glass slides, coverslips were first dipped with gentle agitation in a 100 ml beaker of PBS and then another beaker with Milli-Q water. To remove excess water the coverslip edges were dried with a paper towel. The coverslip was placed cell side down lowered into mounting media on the glass slide , while avoiding bubbles.

FLIM-FRET experiments were carried out using a lifetime fluorescence imaging attachment (Lambert Instruments, The Netherlands) on an inverted microscope [115]. BHK cells transiently expressing mGFP-tagged KRAS^{G12D} (donor), alone or with mRFP-tagged cRaf^{WT} (acceptor) (using 1:5 ratio), were prepared as indicated in each experiment. The samples were excited using a sinusoidally modulated 3 W 470 nm light-emitting diode at 40 MHz under epi-illumination. Fluorescein was used as a lifetime reference standard. Cells were imaged with a Plan Apo 60X 1.40 oil objective using an appropriate GFP filter set. The phase and modulation were determined from 12 phase

settings using the manufacturer's software. Resolution of two lifetimes in the frequency domain was performed using a graphical method [125] mathematically identical to global analysis algorithms [126; 127]. The analysis yields the mGFP lifetime of free mGFP donor (τ_1), and the mGFP lifetime in donor/acceptor complexes (τ_2). FLIM data were averaged on a per-cell basis.

2.5 Protein purification for pulldown

First, a plate was streaked with *E. coli* BL-21 bacteria, containing a previously generated pGEX plasmid with GST-CRaf-RBD[A85K] (from hereon GST-RBD), from a freezer stock and incubated overnight. Then, a single colony was picked from the plate to inoculate 4 ml of media that contained antibiotic. After overnight growth 3 ml of the culture was used to inoculate 100 ml of warmed fresh media with antibiotic. The density of the cell culture was monitored until it reached an OD at 600 nm of 0.5 – 1. Then IPTG at 1 : 1000 was added to the culture and the cells were grown for an additional 4 h. After 4 h 1ml of culture was saved as a sample to measure by western the protein expression after induction. The remaining culture was pelleted by centrifuging at 6,000 g for 5 min, at 4 °C. To lyse the cells, the pellet was re-suspended in lysis buffer (1 x PBS, 5 mM EGTA, 1 % Triton X, PIC 1 : 50, PMSF 1 : 100) and then frozen. Two additional freeze-thaw cycles were performed to lyse the cells. The cell lysate was then sonicated as needed and spun at 30,000 g for 20 min at 4 °C. Finally, the supernatant was combined with 400 µl of beads/buffer slurry (the buffer consists of 1 x PBS, 5 mM EGTA, 1 % Triton X, PIC 1 : 50 and PMSF 1 : 100).

2.6 Pulldown assay

Cell lysate from BHK cells expressing GPF tagged KRAS^{G12D} was incubated with GST-RBD beads with or without compound, for 2 h at 4°C. The first step to prepare the cell lysates was to trypsinize cells in a T75 flask. Next, the cells were separated and centrifuged at 1,000 rpm for 5 min and the media was aspirated. The cells were resuspended in fresh media and centrifuged again for another wash in PBS. The cells were centrifuged a third time and the PBS was aspirated. Finally, cells were resuspended in lysis buffer and lysed by vortexing with two 10 sec pulses with a 5 min rest on ice between. To prepare cell lysate samples for protein assay the same protocol as previously described for the western samples was used (Chapter 2, Section 2.3). For pulldown experiments ~420 μg of protein from the KRAS^{G12D} BHK cells and ~220 μg of protein from the HRAS^{G12V} cells were used. The samples were prepared with cell lysate, 100 μl of 1 : 50 diluted GST-RBD beads, and binding buffer (lysis buffer lacking detergent) to a final volume of 1 ml. The samples were then incubated for 2 h under constant agitation at 4 °C. Then samples were washed with buffer composed of 50 mM Tris, pH 7.4, 1 mM EDTA, 1 mM EGTA, 150 mM NaCl, 0.1 % Trition X-100 and protease inhibitors. After pulldown incubation, the samples were analyzed with western blotting using GFP rabbit (2956S) from Cell Signaling Technology and GST mouse (B-14) from Santa Cruz Biotechnology.

2.7 Cell proliferation assays

For these assays, the cells were plated at $1 * 10^3$ cell count per well in a 96 well plate. To start, the cells were trypsinized, washed and counted. After the count a 1 : 10 dilution of cells was prepared in 10 ml of fresh media, and then 100 μl of the cell

suspension was dispensed per well. The plates were then incubated for 24 h at 37 $^{\circ}$C. Then the media was replaced without washing with 100 µl of media containing compound. Media with compound was prepared by serial dilution at concentrations indicated. For the lung cancer cell lines, it was determined that cells needed at least 56 hours to double, therefore the proliferation assays were conducted for 72 h for all cell lines. After 48 h, the pH of the media can change, becoming toxic to cells. Therefore, every 24 hours the media was changed for fresh media with compound. For the pancreatic cancer cells, cells need 42 hours to double therefore we performed 48-hour incubations . At the end of the incubation the plates were washed with PBS and frozen at -80 $^{\circ}$C for a minimum of 24 h. Next plates were thawed and the CyQuant dye (in lysis buffer provided in the CyQuant^{TM} cell proliferation assay kit, Invitrogen^{TM} kit) was added, and after a five-minute incubation fluorescence (excitation: 480 nm excitation: 520 nm) was measured with a Tecan Infinite M200 plate reader.

Additionally, cell counting experiments for pancreatic cancer cell lines (Miapaca-2 and Bxpc-3) were conducted in 12-well plates. Cells were seeded at $2.6 * 10^4$ cells per well for Miapaca-2 and $5.2 * 10^4$ cells per well for Bxpc-3. Compounds were prepared in full serum media by 8-point serial dilution and the compound- or vehicle-containing media was changed every 24 h. After 72 h, the cells were trypsinized and counted in Trypan Blue using Countess (Invitrogen^{TM}).

2.8 NMR

The Putkey lab used bacteria (BL21) to express KRAS^{WT} labeled with N^{15} [82]. The gene construct was codon optimized to maximize expression and included an N-terminal His tag with a TEV cleavage site to facilitate purification. With this system they were able to

recover approximately 30 mg of KRAS per liter of culture [82]. We then took 2D [H1 N15] HSQC spectra, which showed the amide chemical shift cross-peaks, and determined the prevalence of an ordered conformation of the bacterial expressed KRAS^{WT} [82]. Compounds were added to the NMR solution with KRAS and data amide chemical shift perturbations were collected to determine compound binding.

2.9 Microscale thermophoresis (MST)

Determination of dissociation constants using MST was performed following vendor protocols. Purified KRAS was labeled with the Monolith MT^{TM} Protein Labeling Kit RED-NHS (NanoTemper Tech) through buffer-exchange in the labeling buffer (40 mM HEPES, pH 7.5, 5 mM MgCl$_2$, 500 mM NaCl). The concentration of the eluted protein was adjusted to 2-20 µM, the dye added at a 2-3-fold concentration to a final volume of 200 µL, and the mixture incubated for 30 min at room temperature in the dark. Labeled KRAS was purified using the column provided in the kit. For MST measurements, a 16-point serial dilution of ligand was prepared in an MST assay buffer (40 mM HEPES, pH 7.5, 5 mM MgCl$_2$, 100 mM NaCl, plus 0.05% Tween-20 and 2-4% DMSO), and added to a 100 nM KRAS solution. The solutions were loaded in capillaries and measurements were done at room temperature using 20% LED and 40% MST power. The data were fit in Igor Pro using the Hill equation.

2.10 Nucleotide exchange and release assays

Loading of fluorescent-labeled GDP (BODIPY-GDP; BGDP from hereon) to KRAS was conducted following previous reports [118; 128] , with minor modifications. Purified KRAS was buffer-exchanged in NAP-5 column (GE Life Sciences) in low Mg^{2+} buffer (25

mM Tris pH 7.5, 50 mM NaCl, and 0.5 mM $MgCl_2$). The eluate was incubated with 10-fold molar excess of BGDP (Life Technologies) in the presence of 5 mM EDTA and 1 mM DTT for 1.5 h at 20 °C in the dark. Then 10 mM $MgCl_2$ was added and the solution was incubated for 30 min at 20 °C. Free nucleotide was removed by gel filtration using a PD-10 column (GE Life Sciences) that had been equilibrated with the reaction buffer (25 mM Tris-HCL pH 7.5, 50 mM NaCl, 1 mM $MgCl_2$, and 1 mM DTT). The concentration of [BGDP]KRAS was determined using Bradford assay and a BGDP standard curve. Then the effect of ligands on the intrinsic rate of nucleotide release was monitored using the decrease in fluorescence with time as BGDP dissociates from KRAS in a 100 µL reaction mixture (96-well plate) of 0.5 µM [BGDP]KRAS, 100 µM GTP and varying concentrations of ligand (0 to 25 µM); GTP was added just before measurements. To measure the rate of SOS-mediated nucleotide release, 0.5 µM SOS (residues 564-1049, Cytoskeleton Inc) was added after GTP addition, and fluorescence was immediately read (excitation: 485 nm, emission: 510 nm) using Tecan Infinite M200 plate reader. Intrinsic and SOS-mediated nucleotide exchange rates were monitored with the fluorescence intensity increase of BGTP as it displaces GDP from KRAS. We used a 100 µL reaction mixture containing 0.5 µM each of [GDP]KRAS, BGTP (and SOS) plus varying concentrations of ligand (0 to 25 µM); BGTP was added just before measurements. Experiments were conducted with minimal light and the reaction was monitored for 2 h at room temperature. Fluorescence intensities were normalized at 120 s and the traces were fit with linear or single exponential functions (Igor Pro, Wavemetrics).

2.11 Fluorescence polarization

Fluorescence polarization assay was conducted following previous reports [129;

130]. KRAS was pre-loaded with the non-hydrolyzable fluorescent GTP analog BODIPY-GTP-γ-S (BGTP-γ-S; Life Technologies) using buffer-exchange in NAP-5 (GE Life Sciences) as described in the previous section. Then 0.5 µM (50 µL) of [BGTP-γ-S]KRAS was incubated with an equal volume but varying concentrations (0 to 2.5 µM) of GST-Raf[RBD] (Raf RBD residues 1-149; Life Technologies) for 30 min in the dark. To determine the effect of ligand on RAS-Raf binding, KRAS was first incubated with a fixed concentration of the ligand for 30 min and then with GST-Raf[RBD]. Fluorescence polarization was measured using PolarStar Optima plate reader (excitation: 485 nm, emission: 520 nm) at room temperature. GST-tag was used to increase the weight of Raf[RBD] for a greater polarization. The dissociation constant for KRAS-Raf binding was determined using a quadratic ligand binding equation [129].

2.12 Raster Image Correlation Spectroscopy (RICS) analysis

33 mm dishes were seeded with BHK cells expressing GFP fused KRAS[G12D] at 2 $*10^5$ cells per dish. After 24 h the cells were incubated with compound as indicated or vehicle control for 3 h in serum free media. Live cells were then imaged with a confocal microscope, the GFP was excited by laser at approximately 1.73 mW (excitation 488nm). Image analysis followed previous protocols [131].

Chapter 3: Inhibitors of Mutant KRAS Signaling

3.1 Introduction

Despite decades of effort, drugging KRAS (and RAS proteins in general) remains an unrealized goal [132]. Many studies have established the allosteric nature of RAS [73; 133], and discovered several allosteric small-molecule KRAS binders [75; 77; 82; 118; 134]. Moreover, a number of recent reports described molecular fragments [118], small-molecules [75; 77; 135; 136], peptidomimetics [137; 138] and monobodies [36] that bind KRAS and modulate its functions in various ways. While this progress towards developing a therapeutic agent to inhibit mutant KRAS function is encouraging, to the best of our knowledge these compounds have not made it to clinical trial. In this chapter I will describe our efforts to design a novel small molecule inhibitor of mutant KRAS. One of the goals of this project was to combine MD with HTVS. By doing this, we sought to eliminate the pitfall of docking directly on a protein structure generated by X-ray crystallography because surface pockets can be closed due to crystal packing. Described in this chapter are the details of the molecular dynamics simulations and how we chose a representative structure to use in a HTVS for new KRAS binders. Then the chapter will describe the results of a small cell-based screen of potential hits which yielded a new class of inhibitors. Finally, we used a range of biophysical and cell assays to characterize the new inhibitors. We found that some of these molecules bind to the p1 pocket with nanomolar (nM) affinity and abrogate KRAS signaling by directly inhibiting the interaction of KRAS with effector proteins.

3.2 Simulation analysis

Allosteric pockets on the surface of KRAS are not usually apparent or available for docking in the structural conformations generated by X-ray crystallography. To reveal pockets, Dr. Priyanka Prakash, a researcher from our lab, conducted molecular dynamic simulations of GTP bound KRAS^{G12D} with Nanoscale Molecular Dynamics (NAMD) using the Charmm27 force field [139; 140]. The simulation Dr. Prakash generated for this study, involved KRAS^{G12D} in a typical solvent environment with the addition of small probe molecules [83]. During the simulation the probes interacted with the protein, non-covalently binding to surface pockets as they open and close. By analyzing binding sites and the frequency of contacts, binding hotspots were identified. Allowing the protein to flex with MD simulations such as this can generate open pocket conformations for docking that were not initially available. Thus, we incorporated protein dynamics into the drug screening process and we ensured the HTVS included a protein conformation with largest avaialbe pockets. Therefore, with this pocket conformation we could screen a wider range of molecules in terms of size and configuration.

For the HTVS we chose to focus on pocket 1 (referred to as p1 from hereon), which is located in lobe 1 between the central beta sheet and switch 2, (see **Figure 1.2**) for two reasons. Frist, the residues that compose this pocket (residues 5-7, 37, 39, 50-56, 67 and 70-75) are vital to KRAS effector binding. Residues 37, 38, 39, 41, and 54 are important for interactions with downstream effectors, such as RAF, while residues 36, 37, 38, 67 and 70 are important for interactions with GEFs, such as SOS [1]. Therefore, a molecule that binds to this pocket could potentially interfere with the interaction between KRAS and some direct effectors or SOS. Second, the presence and location of the p1 pocket was experimentally validated by others using multi-solvent or

crystal soaking techniques to generate crystal structures with a small molecule bound to KRAS such as PDB 4DSO [69].

In the next step, we determined which conformations of the protein we would use for docking. This entailed evaluating over 27,000 conformations derived from the simulation to measure the volume of p1. To accomplish this we used a program called Fpocket, which can measure the volume of a pocket in every conformation of a typical ensemble generated by MD simulations [141]. Another method I used to determine which conformation of the pocket to use for screening was conformation-based clustering. This method is based on the number of unique conformations generated during the simulation and considers only the backbone of the protein. Using root-mean-square deviation (RMSD) and a user define cutoff value, nearest neighbors of conformations within the cutoff value are grouped together forming a cluster. This method allowed the entire simulation to be clustered into set representative conformations which contain a decreasing number of conformation members. The volume of p1 measured in the top four clusters, which represented about 90 % of the MD simulation data. We found that p1 ranges in volume from 219 $Å^3$ to 0 $Å^3$ with an average volume of 119 $Å^3$. Additionally, we found that the top four clustered conformations contained two open pocket conformations with p1 volumes of 180 and 120 $Å^3$, respectively. The KRAS conformation in which p1 has the largest volume was selected for docking. This conformation was chosen for two reasons. First it was the largest volume therefore we could increase our chemical search space and test a wider size range of molecules. Second, there are four groves between residues in which molecules could bind and interact via hydrophobic contacts. The grooves are between D54 and S39 (**Figure 3.1 blue**), S39 and E37 (**Figure 3.1, blue and green**), E37 and M67 (**Figure 3.1, green and turquoise**) and

between T74 and K75 (**Figure 3.1, purple**). With a representative conformation of KRAS^{G12D} to use for docking, the next step was to benchmark the docking program to determine parameters for the HTVS.
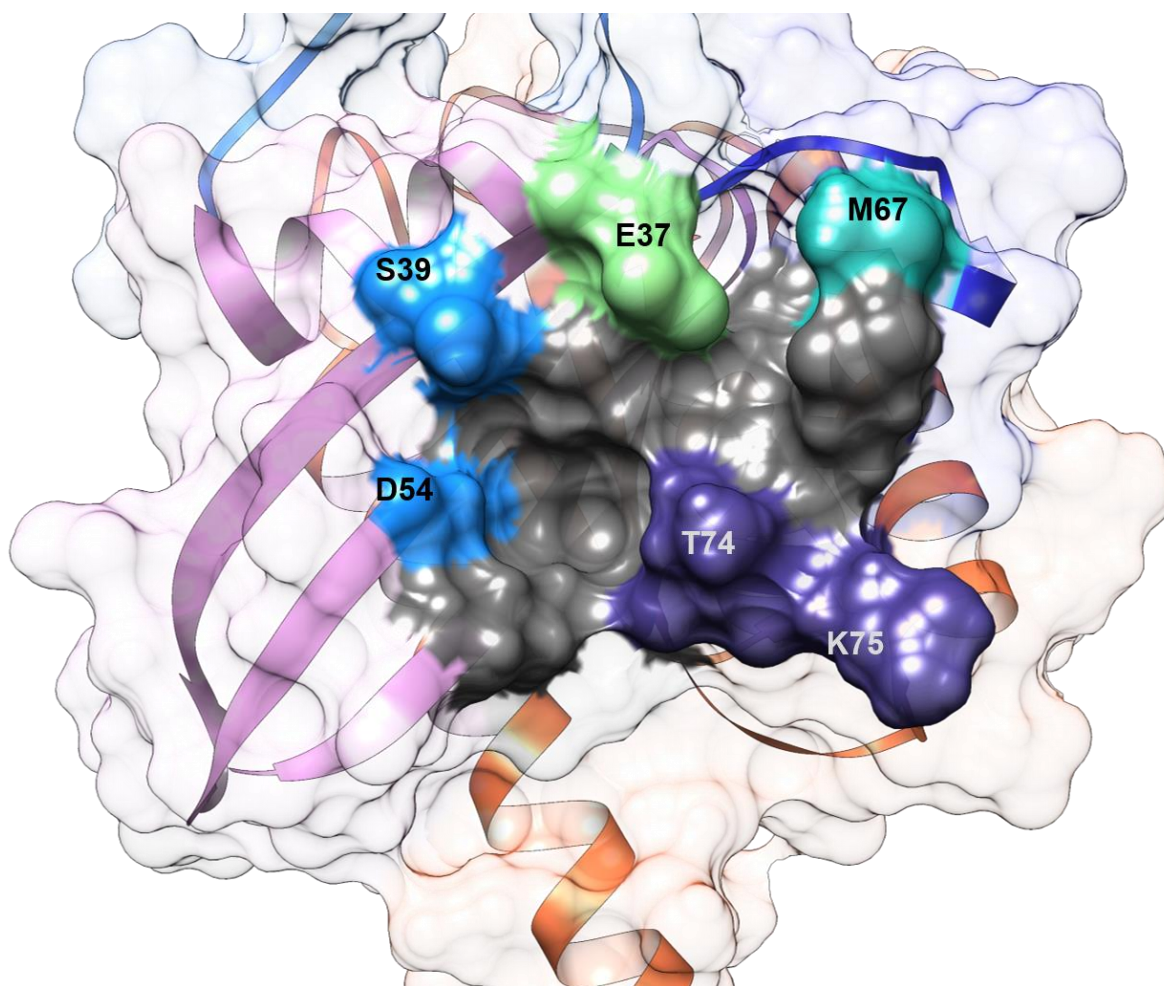
Figure 3.1: KRAS with pocket p1 grooves highlighted. Shown is the structure of KRAS in the conformation used for our HTVS. Molecules could have hydrophobic interactions with the four grooves of pocket p1, highlighted in blue, green, turquoise and purple.

3.3 Running and analyzing the high throughput virtual screen

DOVIS (version 2.0) is a program that was developed to perform multiple AutoDock4 (version 4.0.1) runs in parallel to maximize efficiency [122; 142; 143]. We have DOVIS complied on our cluster, which allows us to screen over 6 thousand molecules per node per day. However, before starting the screen careful benchmarking analysis was necessary to choose the docking parameters, i.e. the number of energy evaluations and the number of algorithm runs, such that HTVS returned results similar to posed molecules determined by X-ray crystallography, see **Table 3.1** for parameters tested. AutoDock4 uses the Lamarckian genetic algorithm to determine the lowest energy binding orientation and configuration of a molecule by generating a population of unique individuals and testing each one in the binding site. The individuals are copies of the molecule with unique orientations and changes of rotatable bonds, which act as "traits" of the individual. The highest scoring individuals become ancestors to the subsequent generations, passing on to the next generation of individuals the orientations or bond torsions or both that resulted in high affinity interactions. The repetition of this process is how the algorithm determines the best pose and score for a molecule. A high number of population members per generation consumes energy evaluations but helps determine the best "genetic traits" to pass on per generation, while the number of generations helps determine the highest affinity pose per molecule. The number of genetic algorithm runs helps ensure reproducibility of the final poses and scores. Slightly reducing the parameters of the genetic algorithm that estimates the binding energy does not significantly change the final score (the error for the AutoDock4 free energy based scoring function is ~2 kcal/mol) [144]. However, increasing the genetic algorithm parameters of AutoDock4 increases the time of docking per ligand. The parameters that

were chosen, described in the methods section, were consistent with both the recommendations of the developers of AutoDock4 and previously published studies [143].

Table 3.1: Testing AutoDock4 Parameters for HTVS

Benchmark	1	2	3	4	5
GA generation x1000	27		270		27
GA energy x1,000,000	1		100	10	10
0QY.pdb	-5.01	-5.01	-5.40	-5.39	-5.39
9LI.pdb	-4.22	-4.22	-4.26	-4.26	-4.26
KOB	-2.99	-2.99	-3.45	-3.48	-3.48
ZINC19991337	-8.35	-8.35	-8.92	-8.51	-8.51
ZINC39352733	-8.24	-6.63	-8.62	-7.12	-7.12
ZINC01328021	-8.12	-8.42		-8.53	-8.53
ZINC39362681	-8.10	-7.69		-8.89	-8.89
Time in Minutes	2 -5		420	45	35

From the first HTVS run we screened over 6 million compounds and selected the top 3,762 molecules that scored a ΔG = -6.8 kcal/mol or higher affinity. The docking score for these molecules ranged from -6.8 to just over -8 kcal/mol and the reported error in the score for AutoDock is ~2 kcal/mol, which means there is no significant difference in score for the top molecules. To narrow down the list of molecules we decided on a consensus scoring method which involved re-screening the top molecules with VINA. VINA is an independent docking program that uses a different search algorithm and scoring method to determine pose and calculate interactions between ligand and receptor [123; 145]. After the VINA screen, we looked at the top 500 in each list (VINA and AutoDock4) and selected the molecules that overlap in ΔG. Additionally, to validate that the best binders were selected we evaluated 8 ligand receptor interactions with BINding ANAlyzer v1.2.0 (binana) a script developed by Durant *et al.* [124]. Included in the binana analysis of the ligand interactions with p1 residues were hydrophobic contacts, hydrogen bonding, pi-stacking interactions and salt bridges (see methods for full description). This gave us 58 molecules, which when compared to the group as a whole were more likely to be better binders with KRAS. Overall, we found that this method helped identify molecules that were enriched for high affinity interactions. Additionally, this approach reduced the number of molecules that had high scores due to their size without making high affinity interactions with p1 residues. Other aspects, such as solvent accessible surface area (SASA) were considered. However, this method eliminated many molecules because the pocket was very shallow and often half or more of the molecule was exposed. Finally, the molecules were visually inspected and based on binana analysis and consensus scoring we concluded that the selected 58 had a good mix of similarity to known binders, high affinity interactions, and drug-likeness.

3.4 Cell signaling assays demonstrate promising effects of compound 11

Western blotting analysis was used to quickly assess the potential impact of our predicted hits on MAPK signaling, a major pathway activated by KRAS^{G12D}. Specifically, we monitored phosphorylated ERK levels (p-ERK) in BHK cells stably expressing KRAS^{G12D} treated with vehicle (DMSO), the MEK inhibitor U0125 (U) or compound at four concentrations (1-100 µM). The results show that the majority of the predicted hits have no effect while a few compounds (e.g. **4**) increase rather than decrease p-ERK levels (**Figure 3.2**). Compounds **9** and **11**, on the other hand, decrease p-ERK levels at concentrations ≥ 50 µM and ≤ 5 µM, respectively. To verify the latter observation, we repeated the experiments in an expanded concentration range starting from 0.1 µM. As in the first screen, compound **11** dose-dependently decreases p-ERK levels, leading to ~50% reduction at 5 µM (**Figure 3.2B**). However, compound **9** increased p-ERK levels at 25 and 38 µM in contrast to the decrease observed at higher concentrations (**Figure 3.2B**). Although a similar increase and then decrease of KRAS signaling with increased ligand concentration has been observed before (49, 52), we selected the more potent and monotonously dose-dependent compound **11** for further analysis.
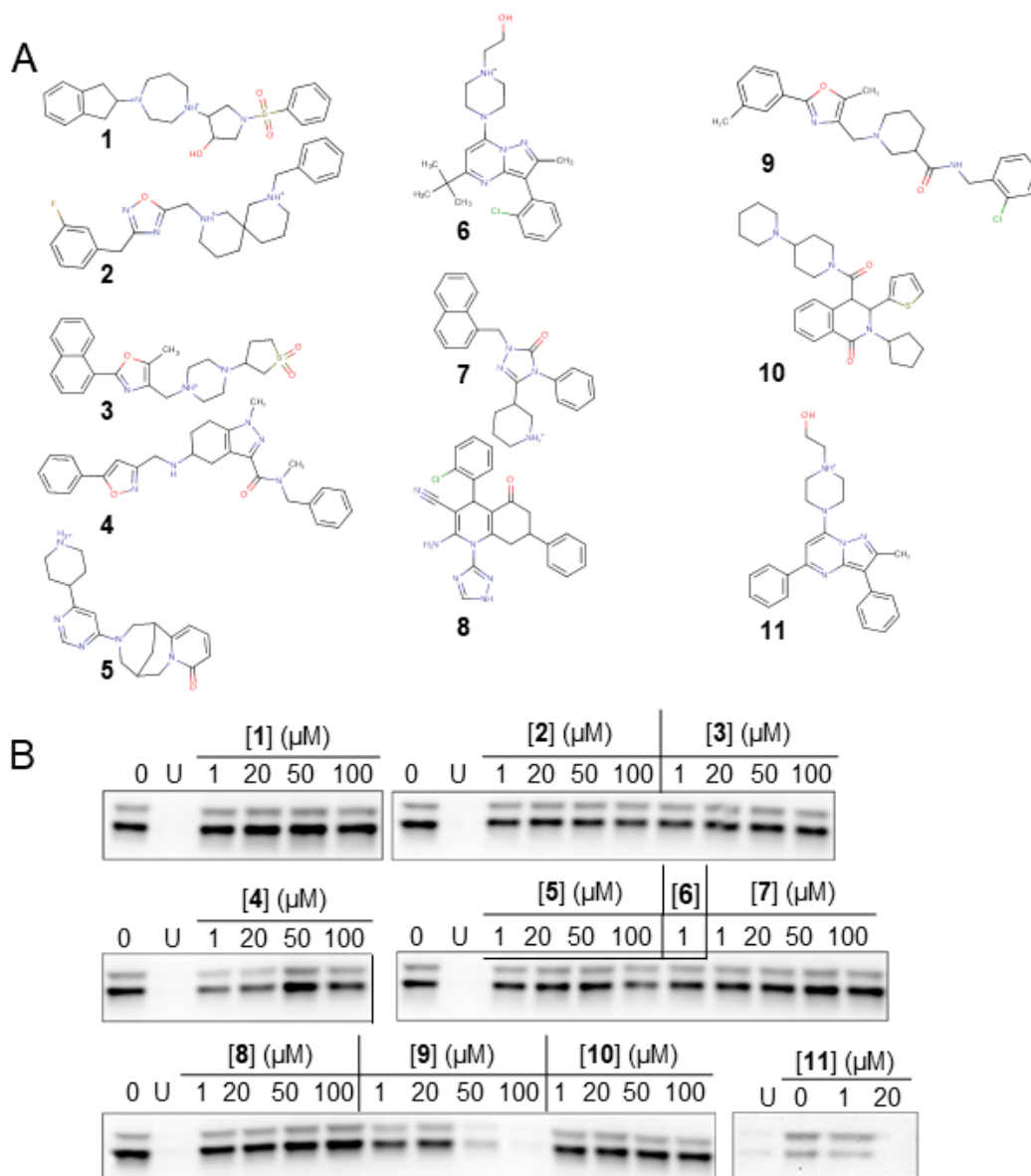
Figure 3.2: *In silico* **prediction and initial experimental characterization of potential KRAS inhibitors. (A)** Chemical structure of eleven computationally predicted hits (compounds **1** through **11**) selected for experimental testing in cell-based assays. **(B)** Western blots showing levels of phosphorylated ERK (p-ERK) in BHK cells ectopically expressing GFP-KRAS^{G12D} treated with vehicle (DMSO), a positive control U (the MEK inhibitor U0125) or compound at the indicated four concentrations.

3.5 Compound 11 binds to WT and oncogenic KRAS mutants with nano-molar affinity.

Figures 3.3B-C show the chemical structure and the predicted complex of compound **11** with KRAS, showing that the ligand forms multiple favorable interactions with residues in the p1 pocket. **Figure 3.3D** shows that the compound binds to ^{GTP}KRAS^{WT} with a K_D = ~0.3 µM, suggesting a very tight binding rarely seen in primary screens. The compound has a very similar affinity (K_D = ~0.4-0.7 µM) for oncogenic mutants KRAS^{G12D}, KRAS^{G12C} and KRAS^{Q61H} in the GTP-bound state (**Figure 3.3D**). However, no binding was detected to KRAS^{WT} and KRAS^{G12D} in the GDP state or to our control Rap1B, a RAS-related small GTPase with homologous structure. Few weak-affinity non-covalent binders that exhibit some selectively toward GDP- or GTP KRAS have been reported (25-27, 53). However, to the best of our knowledge, compound **11** is the first small molecule to selectively bind to ^{GTP}KRAS with nanomolar affinity. In the docked pose (**Figure 3.3C**), the 1-piperazineethanol moiety occupies an electronegative cleft near D54 and D38, and donates hydrogen bonds to the side chain and backbone atoms of E37. The methylated pyrazolopyrimidine core sits in a trench on top of V7 and L56 with the methyl pointing towards I55. The pyrimidine-bound benzene occupies the space between the central beta sheet (β1-β3) and helix 2, making π-stacking interactions with Y71. The pyrazol-attached benzene is buried deep in a tight pocket, stabilized primarily by van der Waals interactions with side chain carbon atoms of V7, L6 and K5; these interactions appear to be crucial for the binding and are common in the majority of our predicted hits in **Figure 3.3A**. We propose that, in addition to potential ligand-induced conformational changes, the compound's preference for ^{GTP}KRAS can be explained by the conformational differences of these residues in ^{GTP}RAS versus ^{GDP}RAS(5).
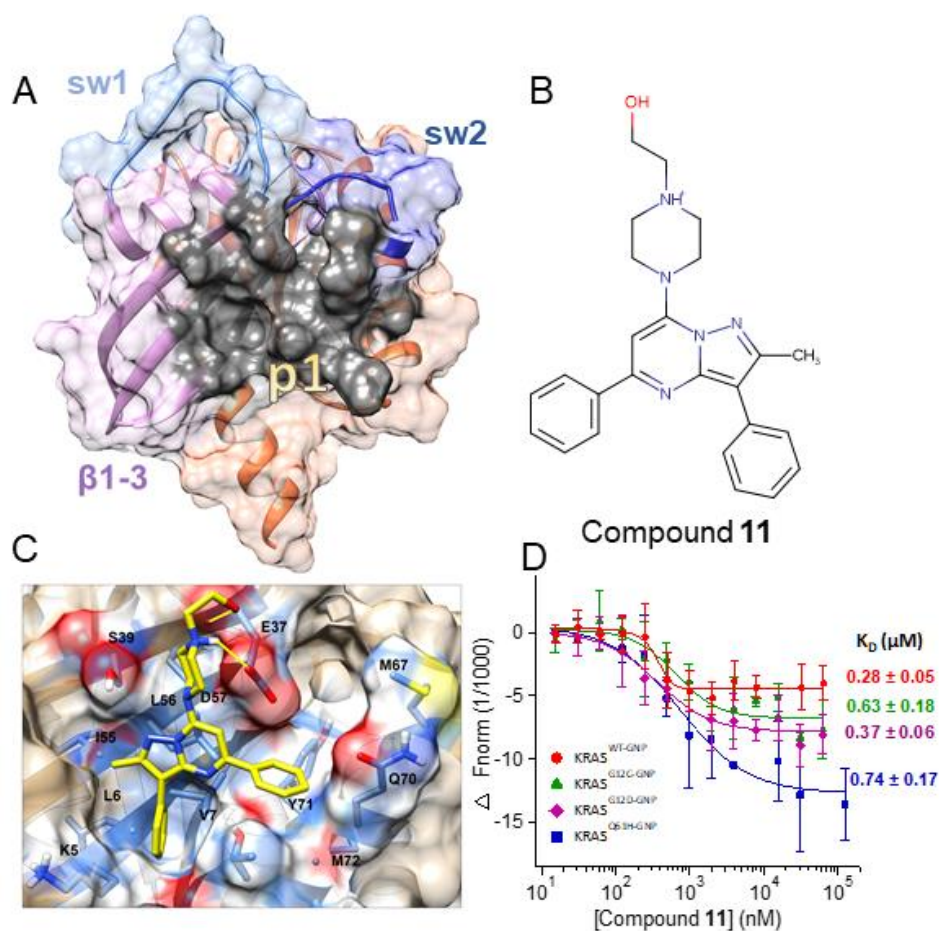
Figure 3.3: Predicted binding mode and measured affinity of compound 11 to KRAS. (A) Structure of the catalytic domain of KRAS used for the virtual screening. Lobe1 (residues 1-86) and lobe2 (residues 87-166) are highlighted in different colors, as well as switches 1 (residues 30-40) and 2 (residues 60-75). Our target allosteric pocket p1 is indicated. **(B)** Chemical structure of compound **11**. **(C)** Predicted binding pose of compound **11** with key polar or vdW interactions with the protein highlighted. **(D)** MST experiments (conducted and figure generated by Dr. Cynthia Pagba) indicating direct binding of compound **11** to KRAS, along with dissociation constants (K_D) derived from the curves. Changes in fluorescence upon titration of 50 µM KRAS with increasing concentration of compound are shown: KRAS[WT] (red), KRAS[G12C] (green), KRAS[G12D] (purple) and KRAS[Q61H] (blue), each bound to the non-hydrolyzable GTP analogue, guanylyl imidodiphosphate (GNP). No binding was detected for GDP-bound KRAS[G12D] and KRAS[WT] as well as Rap1B, which was used as control.

3.6 Compound 11 abolishes interaction of KRAS with RAF.

We used fluorescence polarization, pull-down assays, and FLIM-FRET to check if our compound inhibits RAS signaling by interfering with effector binding. Pull-down assays directly measure the interaction of KRAS with the RBD of RAF in purified or cell lysate systems, while FLIM-FRET measures the interaction of KRAS with full-length RAF in the cellular milieu. Dr. Cynthia Pagba, a researcher in our lab, used fluorescence polarization of BGTP-γ-S to monitor binding of the KRAS catalytic domain to GST-Raf^{RBD} with and without pre-incubation with 1 μM compound **11**. **Figure 3.4A** shows a dramatic decrease in polarization in the entire concentration range of GST-Raf^{RBD}. For example, at 2 μM GST-Raf^{RBD}, compound treatment reduced the polarization and therefore RAS-RAF interaction by >80%. The dissociation constant derived from the polarization curves indicate that **11** reduced the affinity of KRAS to Raf^{RBD} by ~13-fold. Consistent with this observation, pull-down of GFP-KRAS^{G12D} by GST-Raf^{RBD} beads show a significant (e.g. >50% at 1μM of **11**) decrease in GFP-KRAS^{G12D} levels (**Figure 3.4B**). We observed a similar effect in FLIM-FRET experiments in cells, in which quenching of GFP fluorescence lifetime indicates an interaction between GFP-KRAS^{G12D} and RFP-CRAF. Quenching of GFP fluorescence lifetime and hence KRAS^{G12D}-CRAF interaction is significantly reduced upon compound treatment (**Figure 3.4B**). These observations are supported by a comparative analysis of available RAS-RAF structures and our predicted ligand-bound structure. Taken together, these results strongly suggest that compound **11** will inhibit MAPK signaling by directly disrupting RAS-effector interaction.
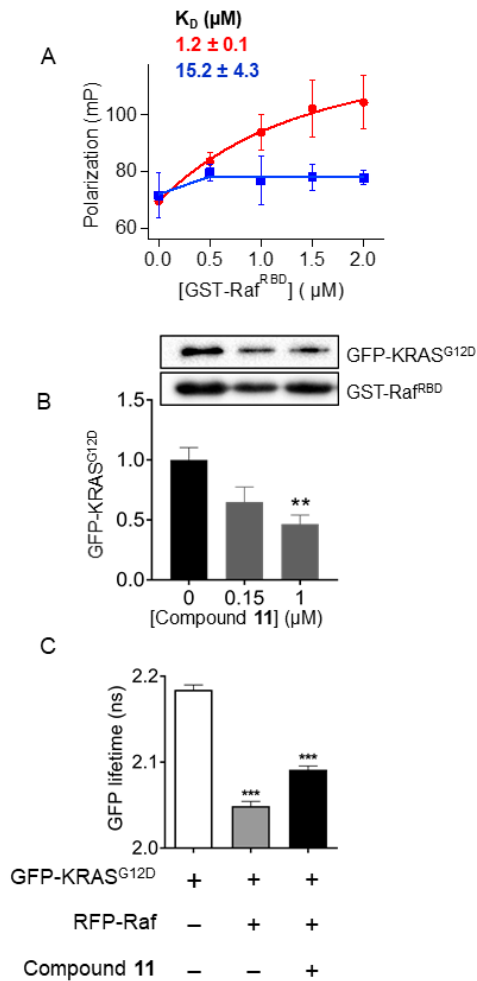
Figure 3.4: Compound 11 disrupts KRAS-RAF interaction. (**A**) Fluorescence polarization (conducted and figure generated by Dr. Cynthia Pagba) of $^{BGTP-\gamma-S}$KRAS (0.5 µM) as a function of a varying concentration of GST-Raf^{RBD} in the absence (red) and presence (blue) of 1 µM compound **11**. Shown above the curves is the K$_D$ for KRAS-Raf^{RBD} binding obtained by fitting the data to $P = P1 + (P2 - P1)\frac{Kd+c+x-\sqrt{(Kd+c+x)^2-4*c*x}}{2}$, where *P1* is polarization of free KRAS, *P2* is polarization of RAF-bound KRAS, *c* is the total concentration of KRAS, and *x* the total concentration of Raf^{RBD}. (**C**) Amount of GFP-KRAS^{G12D} pulled down by GST-Raf^{RBD} after treatment of cell lysates with compound at the concentrations indicated (representative westerns are shown at the top). (**D**) GFP fluorescence lifetime from FLIM-FRET using cells expressing GFP-KRAS^{G12D} alone or with RFP-RAF, with or without treatment by 1 µM compound **11**. Data are shown as mean ± S.E; significance estimated by one-way analysis of variance.

3.7 Compound 11 inhibits KRAS signaling.

Figure 3.5 shows that compound **11** dose-dependently decreases both p-ERK and p-CRAF levels in BHK cells expressing $KRAS^{G12D}$ and $KRAS^{G12V}$, suggesting inhibition of RAS signaling via the MAPK pathway. The data also indicate that the ligand has a slightly lower IC_{50} for its direct effector Raf (e.g., 0.7 in the case of $KRAS^{G12D}$) than the two-steps removed ERK (1.3 µM). Note also that the IC50 for CRAF is very close to the K_D of the ligand for $^{GTP}KRAS$. Changes in phosphorylated (p-AKT) levels show that the compound also inhibits signaling through the AKT pathway but to a lesser extent than the MAPK pathway. Together, these data suggest that the ligand disrupts MAPK signaling by acting on RAS or its upstream modulators. Since our MST data showed that compound **11** binds to $^{GTP}KRAS$ but not $^{GDP}KRAS$, we hypothesized that **11** may be less effective in inhibiting endogenous RAS signaling where RAS is predominantly GDP-loaded. We tested this hypothesis using wild type (un-transfected) BHK cells and found no significant difference in p-ERK levels between treated and untreated cells (data not shown). To test if compound **11** is selective for the KRAS isoform, we measured p-ERK and p-CRAF levels in BHK cells expressing the constitutively active $HRAS^{G12V}$ (**Figure 3.5, right**). The data indicates no significant effect on the phosphorylation of these effectors and hence signaling via the MAPK pathway. Similarly, no major effect on p-AKT levels was observed even though HRAS is a major driver of the AKT pathway. As a control, treatment of the $HRAS^{G12V}$-expressing BHK cells with 10 µM of the MEK inhibitor U0126 (U) almost completely abolished MAPK signaling (**Figure 3.5**). In sum, our comparative cell signaling analyses indicates that compound **11** selectively inhibits signaling through activated KRAS, which is consistent with its dramatic effect on KRAS-RAF interaction (**Figure 3.4**).
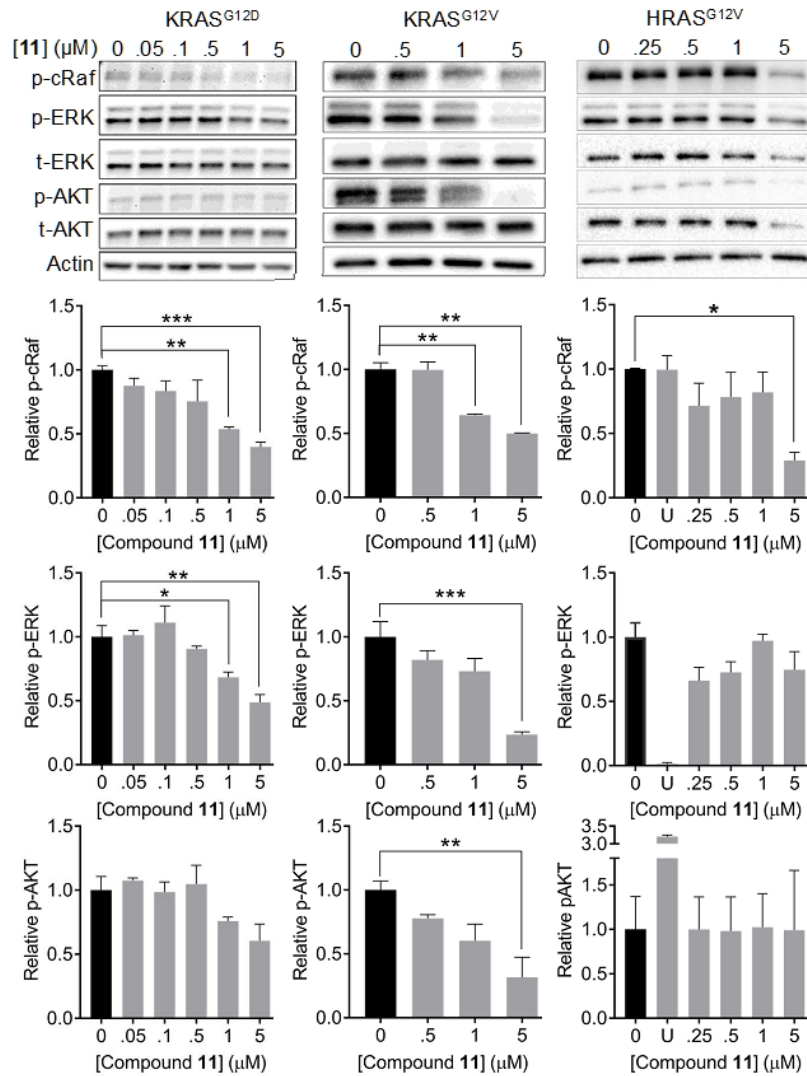
Figure 3.5: Compound 11 inhibits mutant KRAS signaling. Representative western blots (**top**) and their quantification showing levels of phosphorylated CRAF (p-CRAF), ERK (p-ERK) and AKT (p-AKT) in cells expressing KRAS[G12D] (**left**), KRAS[G12V] (**middle**) and HRAS[G12V] (**right**) treated with the indicated concentrations of compound **11,** DMSO or, where indicated 10 μM MEK inhibitor U0125 (U). Compound **11** dose-dependently reduced p-CRAF and p-ERK levels, and to a lesser extent p-AKT levels, in cells expressing KRAS[G12D] (estimated IC_{50} 0.7 μM for p-CRAF and 1.3 μM for p-ERK) and KRAS[G12V], but not HRAS[G12V]. Data are shown as mean ± S.E; significance was estimated by one-way analysis of variance: * = $p < 0.02$; ** = $p < 0.005$; *** = $p < 0.0001$.

3.8 Compound 11 inhibits cancer cell growth.

A CyQuant cell proliferation assay and/or cell counting was used to test if our compound affects growth/proliferation of cancer cells. As test cases, we chose H1975 and H522 (KRAS^{WT}) and SKLU-1 (KRAS^{G12D}) lung cancer cells, and Bxpc-3 (KRAS^{WT}) and Miapaca-2 (KRAS^{G12C}) pancreatic cancer cells. **Figures 3.6 A-B** show that each of these cell lines is sensitive to the compound, with Bxpc-3 and SKLU-1 being especially responsive. Consistent with the binding data (**Figure 3.3 D**), there is no significant difference in the effect of **11** on KRAS^{WT} and KRAS^{G12D} lung cancer cells. However, there is a typical hormesis in our Bxpc-3 data, a trend noticed in toxicology that can indicate a beneficial effect of a molecule at some concentrations. The CyQuant assay measured DNA content as an indicator of proliferation. We used cell counting to test if the observed increase in DNA content translated to cell proliferation. The result shown in **Figure 3.6 B** indicates that the enhancement in DNA synthesis did not lead to enhanced cell proliferation. Moreover, the compound is significantly more effective in the KRAS^{WT} Bxpc-3 cells than the KRAS^{G12C} MiaPaCa-2 cells, which is consistent with the difference in affinity for KRAS^{G12C} compared to KRAS^{WT}, observed in MST (**Figure 3.6 B**). However, given the lack of effect on RAS^{WT} signaling (**Figure 3.6 D**) we hypothesized that compound **11** could enhance interaction of KRAS with pro-death effector RASSF6. In pulldown experiments in **Figure 3.6 C** we show RASSF6 is pulled down with KRAS^{G12D} at high concentrations of compound **11**. Overall, however, it is clear that compound **11** inhibits proliferation or survival of cancer cells.
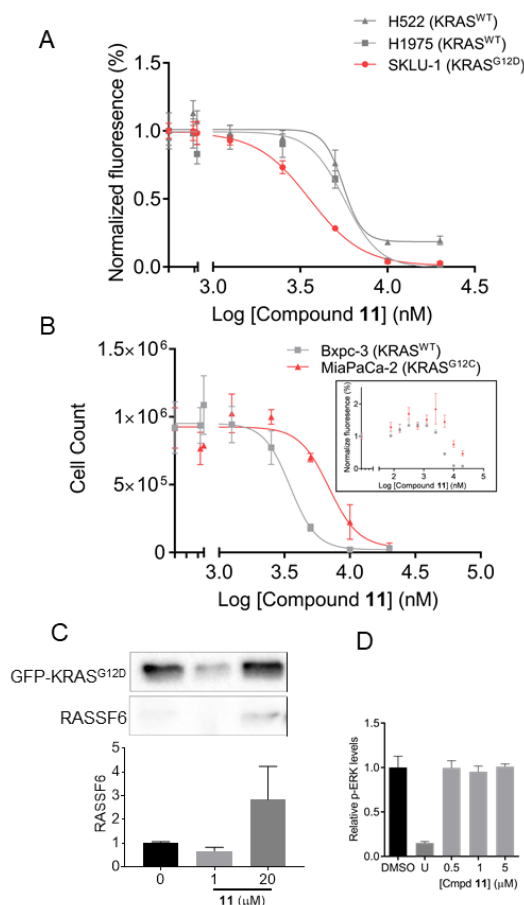
Figure 3.6: Proliferation assays suggest that cancer cells are sensitive to compound 11.

(**A**) Proliferation profile of lung and pancreatic cancer cells upon treatment by increasing concentration of compound **11** monitored by CyQuant assay. The lung cancer cell line with mutant KRAS^{G12D} (SKLU-1) is slightly more sensitive than its KRAS^{WT} counterparts H522 and H1975. However, the mutant KRAS (MiaPaCa-2) pancreatic cancer cell line is less sensitive then Bxpc-3 KRAS^{WT} pancreatic cancer cell line. (**B**) Proliferation profile of pancreatic cancer cells upon treatment by increasing concentration of compound **11** monitored by cell counting. The inset is the results from the CyQuant assay showing a hormesis in response to compound **11** at lower concentrations. Data are averages over three independent experiments and error bars represent standard error. (**C**) A representative western of pulldown assay with GST-RBD, the blot indicates RASSF6 is pulldown with GFP-KRAS^{G12D} at 20 μM of compound **11.** On the right is the quantification of the western blots. This was preformed twice. (**D**) Quantification of western of p-ERK levels in BHK^{WT} cells treated with compound **11**, preformed in triplicate.

3.9 Effect of compound 11 on intrinsic and GEF-dependent nucleotide release and exchange reactions.

In addition to its effect on effector binding, compound **11** also slightly reduced the rates of both intrinsic and SOS-mediated GDP/GTP exchange reactions of KRAS, as well as SOS-mediated GDP release. **Figure 3.7** shows time-dependent decreases and increases of fluorescence intensity as a labeled-nucleotide dissociates from and binds to KRAS^{WT}, respectively. Compound **11** reduced the rates of both intrinsic and SOS-mediated nucleotide exchange reactions, as well as the SOS-dependent (but not intrinsic) release of labeled-GDP. In particular, **11** decreased the intrinsic rate of nucleotide exchange by ~10-fold (**Figure 3.7, top-left**) but has no effect on intrinsic nucleotide release (**Figure 3.7, bottom-left**). The latter is consistent with our observation from MST that **11** does not bind to ^{GDP}KRAS^{WT}. Since GTP hydrolysis is unlikely to occur within the timescale of our experiments [82; 146], a plausible interpretation of the former would be compromised GTP loading. This is possible if, for example, the ligand binds to the nucleotide free 'transition state' conformation of KRAS and induces reorganization of active site residues. This is supported by the fact that **11**'s effect on the rate of nucleotide exchange is significantly smaller (only a 1.1-fold decrease, **Figure 3.7, top-right**). SOS stabilizes nucleotide free RAS in an open active site conformation [31], which allows for faster expulsion and rebinding of GTP or GDP. Stabilization of the KRAS:SOS complex could also help counteract the observed effect of the ligand in intrinsic nucleotide exchange, and may explain the 1.5-fold reduction in the rate of SOS-mediated GDP release (**Figure 3.7, bottom-right**).
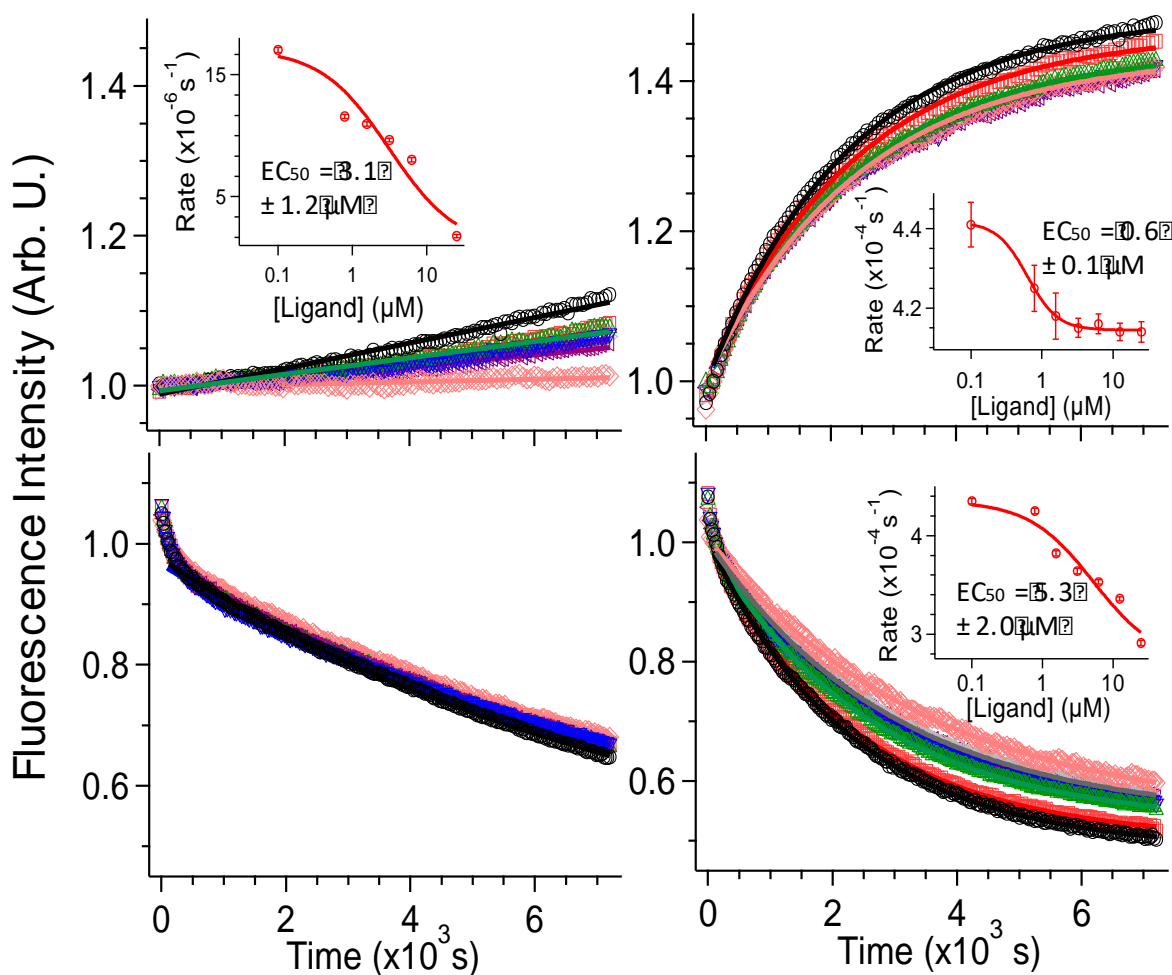
Figure 3.7: Effects of compound 11 on intrinsic and SOS-mediated nucleotide exchange and release. (Top) Intrinsic (left) and SOS-mediated (right) rates for the nucleotide exchange reaction $KRAS^{GDP} + BGTP \rightarrow KRAS^{BGTP} + GDP$ in a mixture of 0.5 μM each of KRAS, BGTP, and SOS. (**Bottom**) Intrinsic (left) and SOS-mediated (right) rates of the nucleotide release reaction $KRAS^{BGDP} + GTP \rightarrow KRAS^{GTP} + BGDP$. Concentrations of KRAS and SOS were 0.5 μM and that of GTP was 100 μM. Ligand concentrations: 0 (circle), 0.78 (square), 1.56 (triangle), 3.12 (inverted triangle), 6.25 (left-sided triangle), 12.5 (right-sided triangle) and 25 μM (diamond). Intensities were normalized with respect to the value at 120 s. Linear or single exponential fits, starting from 120 s, were superimposed as solid lines. Inset: Calculated rates as a function of ligand concentration. (work and figures generated by Dr. Cynthia Pagba)

Plotting the measured rates as a function of the total ligand concentration yielded additional insights into the effect of **11** in the intrinsic and GEF-catalyzed enzymatic activity of KRAS. We obtained an estimated EC_{50} of 3.1 ± 1.2 µM from the intrinsic nucleotide exchange assay, and a similar value of 5.3 ± 2.0 µM from the SOS-mediated GDP release assay. These values are about 10-times larger than the K_D of **11** for $^{GTP}KRAS^{WT}$, suggesting a potentially weaker binding to the nucleotide free state assuming that the observed effects on enzymatic activity are at least in part a result of binding to nucleotide free KRAS. Intriguingly, we obtained EC_{50} = 0.6 ± 0.1 µM from the SOS-dependent nucleotide exchange measurements, a value very close to the K_D of **11** for $^{GTP}KRAS^{WT}$. This may reflect binding to the GTP-bound KRAS at the allosteric site of SOS but the resulting change in the rate is very small. In fact, all of the effects we observed on reaction rates are much smaller than those in KRAS-Raf interaction. Nonetheless, they are statistically significant and dose-dependent, suggesting that compound **11** modulates KRAS activation through multiple mechanisms.

3.10 Derivative compounds 12 and 13 give insight into structure activity relationships.

To identify the chemical fingerprints of compound **11** responsible for its high-affinity binding and dual-effect on KRAS function, we studied compounds **12** and **13**. Obtained from similarity searches based on **11**, these analogues provided invaluable insights into the mechanisms of action of our pyrazolopyrimidine-based ligands. The 1-piperazineethanol functional group in **11** is replaced by 1-methylpiperazine (**Figure 3.8 A & B**) in compound **12**. As a result, it is more hydrophobic and therefore less soluble in DMSO. Nonetheless, at a somewhat higher concentration of 2 µM, **12** significantly reduced the p-ERK levels, but had no effect on the p-cRaf levels (**Figure 3.8 C**). This suggests a different mechanism of inhibition compared with compound **11**. We confirmed this by FLIM-FRET, which shows that, unlike **11**, compound **12** does not affect KRAS-Raf interaction (**Figure 3.8 D**). Consistent with its lack of effect on effector binding, compound **12** is less effective in inhibiting cell proliferation (**Figure 3.8 E**). For example, the IC_{50} of growth inhibition for the five cancer cell lines is ~3 to >30 µM for compound **12** compared with 2-5 µM for compound **11**. Clearly **12** exhibits a better selectively profile, even if the estimated IC_{50} in each case might be an upper bound due to the low solubility of the compound.

Despite the many attractive features of compound **12** as described above, a compound with a better solubility profile would be desirable. Also, we reasoned that a derivative that preserves **11**'s effectiveness in inhibiting effector binding would make for a better lead compound. Compound **13** (**Figure 3.8 A & B**) satisfies both of these conditions: it has a methyl group attached to the pyrimidine in place of the benzene ring found on **11**, which makes less hydrophobic and readily soluble in DMSO and other

common solvents, and inhibits KRAS-Raf interaction (see below). Since soluble

compound **13** is much more amenable for a detailed biophysical characterization than

12, Dr. Pagba measured the K_D of its interaction with G12D and other KRAS mutants

using MST. The results summarized in **Figure 3.8 C** show that this compound has a 6.5-

7.1-fold weaker affinity for KRAS than compound **11**. Similar to compound **11**, however,

13 does not bind to $^{GDP}KRAS^{WT}$ or $^{GDP}KRAS^{G12D}$.
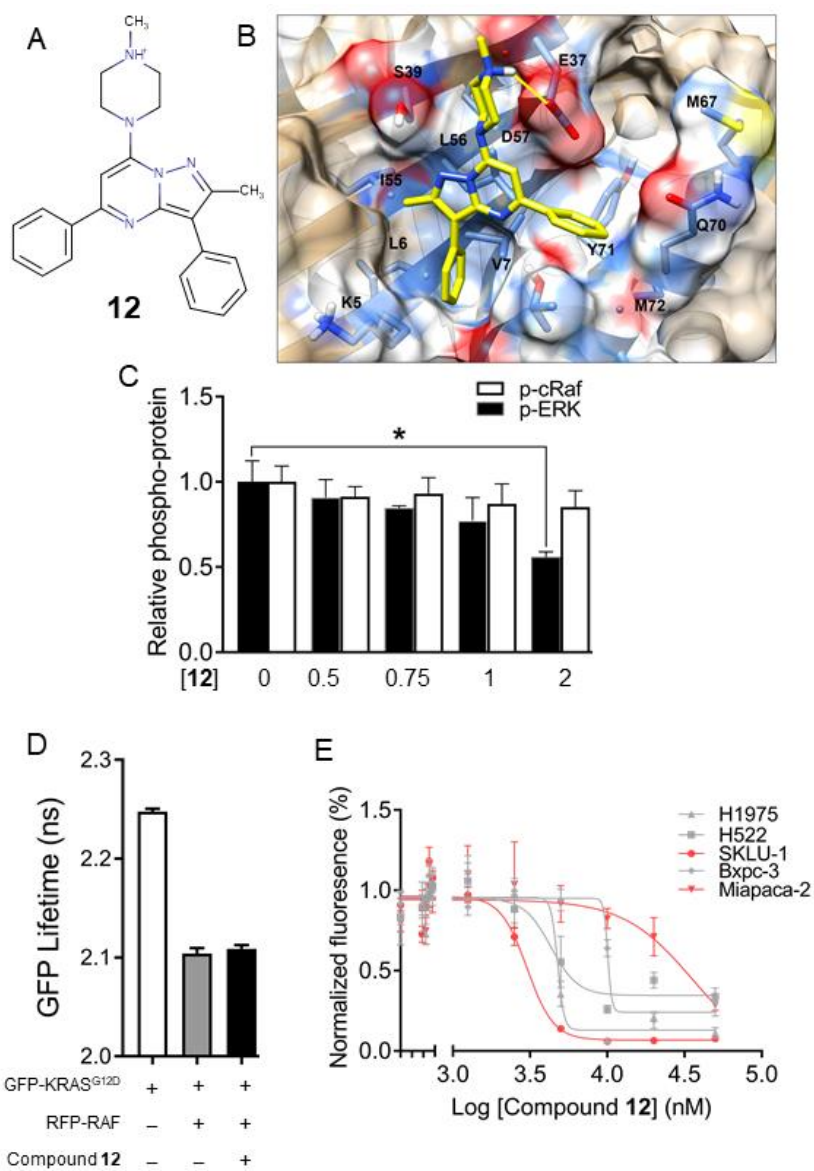
Figure 3.8: The piperazineethanol moiety of compound 11 is critical for abrogating effector binding. (**A**) Chemical structure of compounds **12,** an analogue of **11** lacking the terminal methyl alcohol functional group. (**B**) Predicted binding pose of compound **12**. (**C**) p-ERK and p-cRaf levels in BHK cells expressing KRAS[G12D] treated with indicated concentrations of compound **12** or vehicle. (**D**) GFP fluorescence lifetime from FLIM-FRET using cells expressing GFP-KRAS[G12D] alone or together with RFP-cRaf, with or without treatment with 2 μM compound **12**. (**E**) Proliferation profile of lung cancer cells upon treatment with increasing concentration of compound **12**, monitored by a CyQuant assay. Data are averages over three independent experiments and error bars represent standard error.

We used fluorescence polarization and pull-down assays to test the functional implication of the modification in compound **13** relative to the parent compound **11**. **Figure 3.9 D** shows that 20 µM of **13** disrupts the interaction of KRAS with GST-Raf^{RBD} as effectively as the parent compound. The pull-down assay led to the same conclusion: compound **13** disrupts KRAS^{G12D}-Raf^{RBD} interaction (**Figure 3.9 E**). These results demonstrate that modifications can be made on the pyrazolpyrimidine core to optimize for potency and selectively without compromising effect on effector binding.

We then wondered if interactions with switch 2 residues may play a role in nucleotide release, because the conformation of many switch 2 residues, such as Y71 and Y64, differs between free and GEF-bound RAS (24-26, 54). To test this, Dr. Pagba measured the intrinsic and SOS-dependent rates of labeled-GDP release in the absence and presence of compound **13**. We found that, indeed, replacing the benzene ring on the pyrimidine core by methyl dramatically altered the effect on nucleotide release. Whereas compound **11** had no effect on intrinsic and only modestly decreased the rate of SOS-mediated nucleotide release, compound **13** dramatically increased both rates (**Figure 3.9 F**). This result demonstrates that interaction with switch 2 residues including Y71 determines how a p1-bound ligand affects GEF activity.
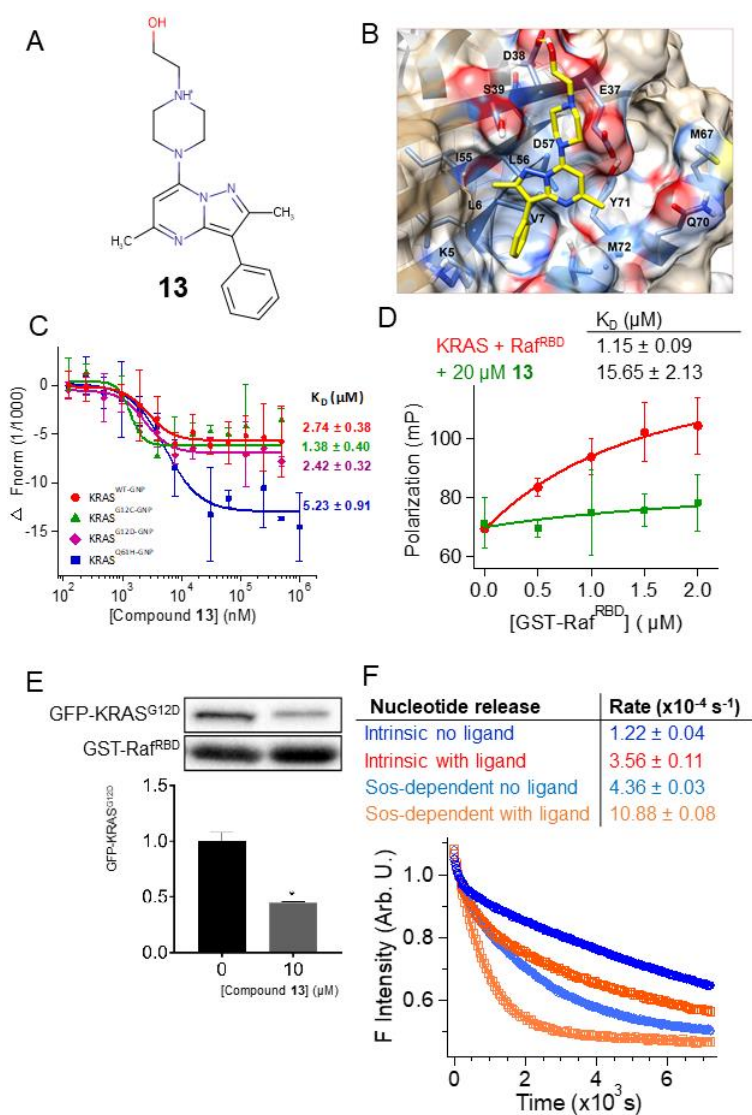
Figure 3.9: Interaction with switch 2 residues is important for modulating exchange factor activity. (**A**) Chemical structure of compounds **13,** an analogue of **11** without a benzene on the pyrimidine core. (**B**) Predicted binding pose of compound **13**. (**C, D**) Fluorescence intensity (**C**) and K_D obtained from MST experiments on KRAS mutants and control. See legend of Figure 2 for additional details. (**D**) Fluorescence polarization of $^{BGTP-\gamma-S}$KRAS (0.5 µM) with increasing concentration of GST-Raf^{RBD} in the absence (red) and presence (green) of 20 µM compound **13**. (**E**) Level of GFP-KRAS^{G12D} pulled down by GST-Raf^{RBD} after treatment of whole cell lysates with 10 µM of compound **13** (representative western blots are shown at the top). (**F**) Intrinsic and SOS-mediated nucleotide release from KRAS in a mixture of 0.5 µM KRAS (and SOS), 100 µM GTP and 0 or 50 µM of compound **13**. (Parts **C**, **D** and **F** work and figures by Cynthia Pagba)

3.11 Conclusion

In the work described in this chapter, we used structure based computational design followed by biophysical and cell biological experiments to discover a novel high-affinity KRAS inhibitor that has unique structural features. Compound **11** non-covalently binds to KRAS at allosteric site p1 with nano-molar affinity, abolishes interaction with Raf, and slightly decreases both intrinsic and SOS-mediated nucleotide exchange reactions. This compound inhibits KRAS signaling and proliferation of KRAS-dependent cancer cells. We also discovered two analogues of compound **11** that bind KRAS with somewhat weaker (low µM) affinity but exhibit a remarkable capacity for selectivity. The compounds inhibit KRAS signaling via dramatically different mechanisms, which we traced back to specific protein-ligand interactions. This diversity in structure-activity relationship provides an ideal platform for further optimization of our highly promising lead compounds.

Chapter 4: A Second Screen for KRAS Binders

4.1 Introduction

During the HTVS for inhibitors we conducted some *in vitro* cell-based and biophysical assays on a handful of high scoring compounds to develop our approach for validating the HTVS hits. During these validation experiments we found one molecule, which will be referred to as **M1**, that decreased p-ERK levels in KRAS mutant cells and bound to KRAS as indicated by NMR (to be discussed later). From these results we initiated a similarity search of the PubChem database based on **M1**, with a Tanimoto threshold of 90%. The search yielded a new small library of ~3,000 similar drug-like molecules. These molecules were then screened against the same conformation of GTP bound mutant KRAS^{G12D} that was derived from a MD simulation. For this screen we again focused on pocket p1, which is located between switches 1 and 2 of KRAS. The PubChem molecules were docked with Autdock4 and then redocked with VINA to get a consensus score of high affinity binders. The top hits were analyzed as described previously and 42 were selected as potential hits from which we were able to procure 13 for a cell-based screen. This process allowed us to to test this method to generate additional binders and to generate additional data for optimization methods.

4.2 Cell-based screen of M1 similarity hits.

We screened the top 13 hits with a monoclonal BHK cell line that ectopically expressed GFP-KRAS[G12D] to identify molecules that decrease p-ERK levels. To reduce background ERK phosphorylation due to endogenous KRAS[WT] we used serum free media. Additionally, to identify compounds that caused an acute decrease in p-ERK, which would indicate disruption of effector binding, we choose a 3 h incubation (see methods for full description of the screening procedure). The westerns in **Figure 4.1** show the results of the screen and the corresponding compound structures. For compound **M3** we observed a strong dose dependent decrease in KRAS signaling at 20 and 50 µM. However, during the second round of testing with more concentrations we observed the effect on signaling to be inconsistent. Our data indicates a 30% decrease averaged over multiple trials. Many of the other compounds either had no observable effect on KRAS signaling or enhanced p-ERK at the higher concentrations. This increase in signaling for some molecules correlated with changes in cell morphology that indicated toxicity. Therefore, we concluded that enhanced signaling was induced by toxicity, rather than the molecule's specific effect on KRAS. For other molecules we hypothesize the increase indicates hormesis, which can also indicate the compound binds to more than one target and the dominate effect changes with concentrations [147]. Consistent with this phenomena **M1** increased p-ERK during a short incubation experiments and decreased p-ERK during a long incubation experiments. As part of this hypothesis we are extrapolating that the time difference is equivalent to a concentration difference.
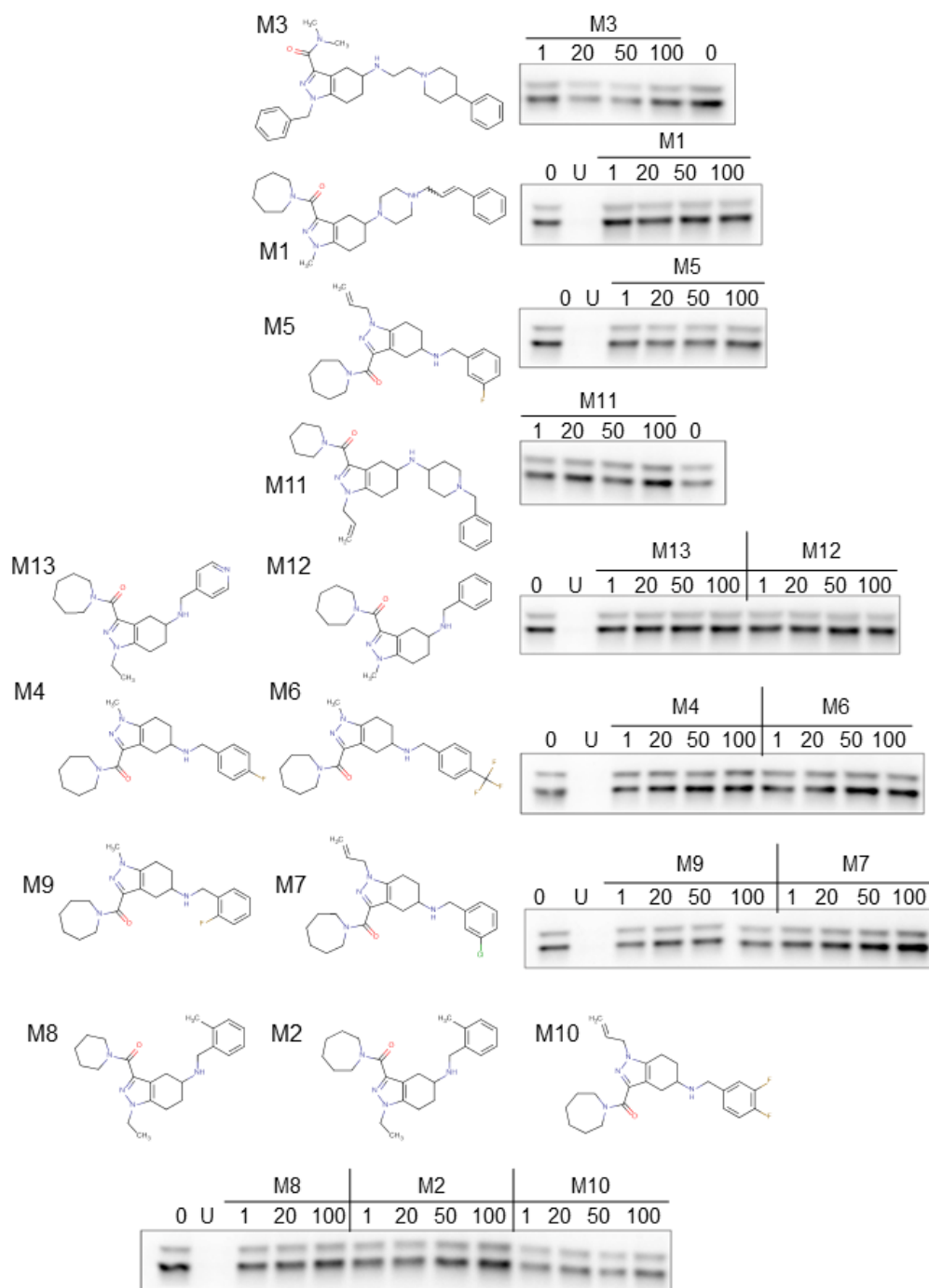
Figure 4.1: Cell-based screen of 13 structurally similar compounds. Chemical structures and accompanying western blots showing levels of phosphorylated ERK in BHK cells after treatment with compound for 3 h in serum free media. The BHK cells ectopically express GFP-KRAS^{G12D}. Indicated concentrations are in µM with negative control indicated as 0 (DMSO vehicle) and the positive control indicated as U (MEK inhibitor U0126 at 10 µM).

4.3 Biphasic effect on KRAS signaling.

A previous lab member, Dr. Hocker, and a Hancock lab member, Dr. Cho, showed that a class of small molecules called Andrographolides inhibit SOS-mediated nucleotide exchange of KRAS in a BHK cell-line expressing KRAS^{G12V} [82]. They demonstrated that as a result of this inhibition p-ERK levels were reduced. However, it is known that KRAS^{G12V} and KRAS^{G12D} are insensitive to GAP mediated GTP hydrolysis and that the rate of GTP hydrolysis is slowed significantly in mutant KRAS [117]. Therefore, to measure effects on KRAS signaling caused by SOS inhibition they required an incubation period of 48 h. We have tested **M1** in a similar 48 h incubation experiment with the BHK cells expressing KRAS^{G12D} used for this screen. The results of these assays, shown in **Figure 4.2**, indicate a dose dependent decrease in p-ERK levels (by ~80% relative to the vehicle control), with an estimated IC$_{50}$ of 40 μM (estimated by Prism GraphPad 4-parameter fit). Additionally, our western data indicates a decrease in p-AKT levels by ~80% relative to the vehicle control. (**Figure 4.2**). We hypothesize this compound may disrupt GEF interaction and binding of PI3K but not RAF interaction. Interestingly, **M1** produced an ~0.8-fold increase in p-ERK levels after a 3 h incubation during the primary screen at all concentrations tested. When we followed up the primary screen with additional short incubation experiments that included KRAS^{WT} cells as a control, our results indicated **M1** enhanced KRAS^{G12D} signaling at the lowest concentration tested, but no change is observed in KRAS^{WT} (**Figure 4.2**). The observed increase prompted us to hypothesize that this compound may enhance dimerization of KRAS^{G12D} or enhance effector interactions.
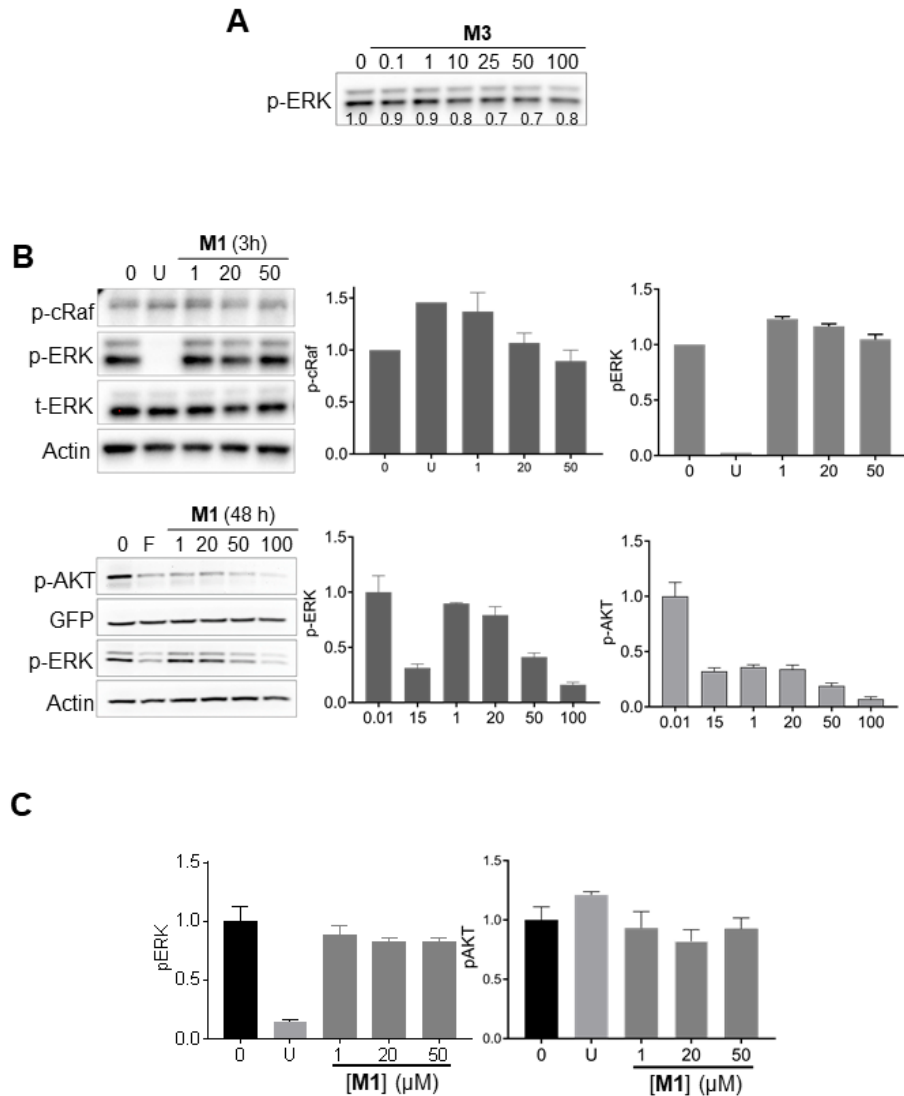
Figure 4.2 Compound M1 effect mutant KRAS signaling in short and long incubations. (**A**) Representative western blot showing levels of phosphorylated ERK (p-ERK) in BHK cell treated with compound **M3** at concentrations indicated. The average relative level of p-ERK is indicated at the bottom of the blot. (**B**) Representative western blot showing effect of compound on mutant KRAS signaling pathway output on p-cRaf and p-ERK after 3 h incubation (top). (Bottom) Representative western blot showing the effect of **M1** on the levels of p-AKT and p-ERK after 48 h incubation. Quantification of p-AKT and p-ERK (left), relative to the 0 concentration (vehicle) with positive control Fendiline (15 µM), the error bars representing the standard error of the mean for 2 replicate experiments. (**C**) The quantification of p-AKT and p-ERK levels from untransfected BHK cells after 3 h incubation with **M1** in full serum media. (**B & C**) The negative control is the 0 concentration (vehicle) and the positive control is U (MEK inhibitor U0126), the error bars represent standard error of the mean for 3 replicate trials.

To test for enhanced effector binding, we conducted two experiments, the first was FLIM-FRET with GFP tagged mutant KRAS^{G12D} and RFP-CRAF^{WT} and the second was GFP-KRAS^{G12D} pulldown with GST-RBD (as described in chapter 3). The results of the FLIM-FRET assay indicated there is no disruption of Ras-Raf interaction during 3 h incubation, but there is a slight disruption of the interaction upon 48 h incubation of cells with compound **M1** (**Figure 4.3**). The 48 h experiment data for FLIM-FRET is consistent with the signaling results seen by western blot.

For the pulldown assay we incubated cell lysate from BHK cells expressing GFP-KRAS^{G12D} with GST-RBD on glutathione agarose beads for 2 h with or without compound **M1**. The results of the pulldown assay to-date show a trend of increased KRAS pulldown; however, these experiments remain unfinished. In **Figure 4.3** there is a dose dependent increase in KRAS pulldown with increasing concentration of compound **M1**. The data could indicate that this compound somehow enhances the interaction between KRAS^{G12D} and the RBD. However, the magnitude of GFP-KRAS^{G12D} pulldown varied with each experiment generating a large error. Considering the variability in the pulldowns, we interpret these findings that increased signaling at low concentrations of **M1** may not be a result of directly enhancing the interaction between KRAS^{G12D} and its effectors.

4.4 RICS analysis indicates M1 enhances oligomerization.

To determine if **M1** causes an enhancement of dimerization KRAS^{G12D} we performed Raster image correlation spectroscopy (RICS) on compound-treated KRAS^{G12D} cells (**Figure 4.3C**). This work was done by Dr. Suparna Sarkar-Banerjee, a post-doctoral research in our lab. Specifically, we treated BHK cells expressing GFP-

KRAS^{G12D} with **M1** at 50 µM for 3 h in serum free media. Time of diffusion data from microscopy images was analyzed to determine the oligomerization state of GFP-KRAS^{G12D} with comparisons made between compound treated and vehicle treated control cells. The diffusion coefficient of the treated cells was lower than the control cells, suggesting their slower diffusion dynamics was due to higher order structures (**Figure 4.3C**). The results indicate that for control cells GFP-KRAS^{G12D} exists mostly as monomers and some dimers, whereas the treated cells had a mixture of dimers, trimers (most common) and higher order oligomers. Our results show that when cells were treated with 50 µM of compound **M1**, there was an increased number of oligomers and a decreased number of monomers of GFP-KRAS^{G12D}. This suggests that **M1** is enhancing dimerization and higher order oligomerization of GFP-KRAS^{G12D} and enhanced dimerization could cause the increased signaling as seen in western blots [148].
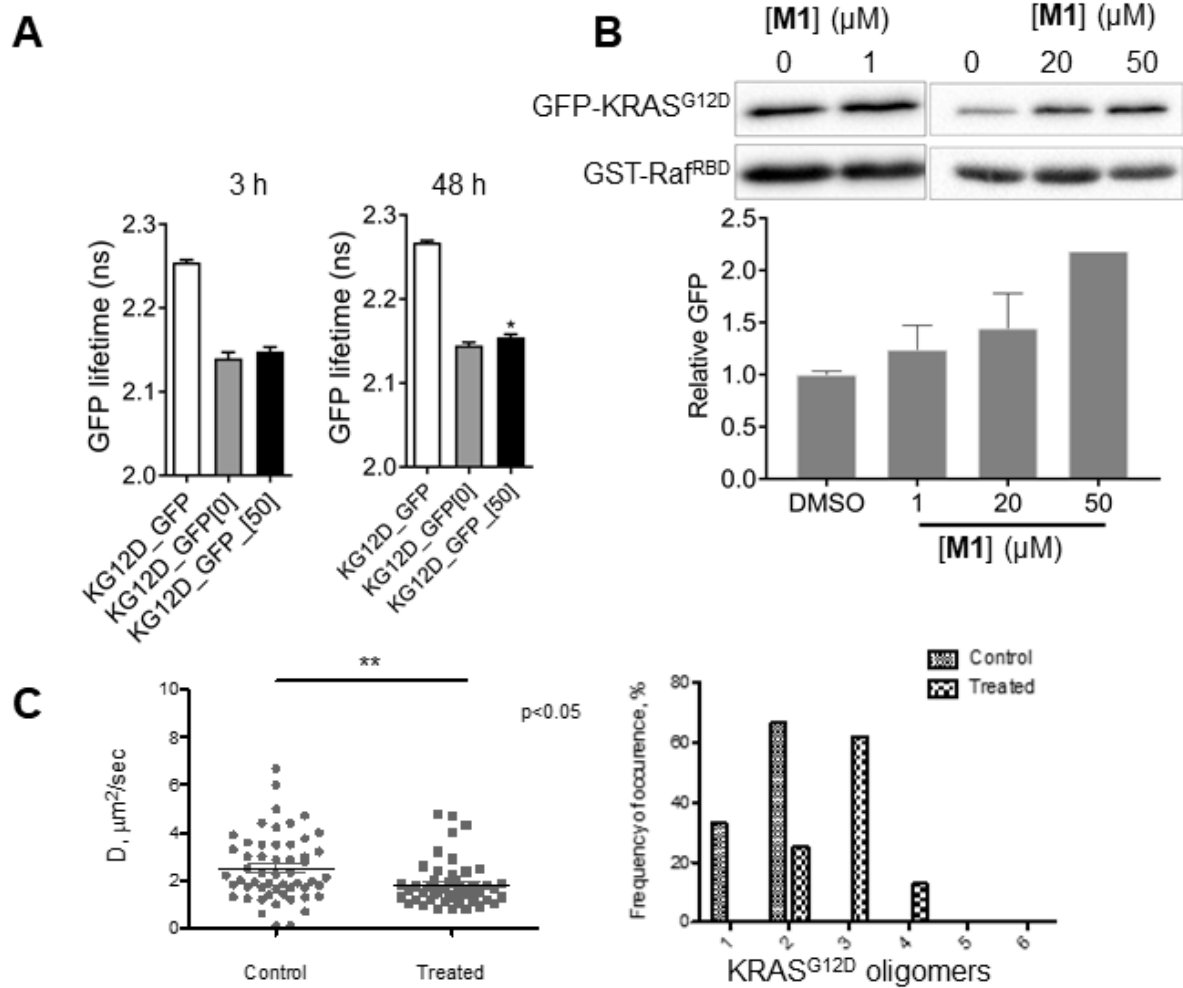
Figure 4.3: FLIM-FRET and RICS analysis of M1. (**A**) FLIM-FRET with BHK cells transfected with RFP-cRAF^WT and GFP-KRAS^G12D and incubated with **M1** for 3 h or 48 h. (**B**) Representative western blot of an active GFP-KRAS^G12D pulldown assay with GST-RBD. The concentrations are ranged from 1 to 50 µM as indicated by the blot and quantification below. (**C**) RICs analysis (work and figures by Suparna Sarkar-Banerjee) of BHK cells expressing GFP-KRAS^G12D after 3 h incubation with **M1** at 50 µM.

4.5 Nucleotide exchange data indicates biphasic response with increased concentrations.

Next, we tested the hypothesis that **M1** disrupts SOS interaction or nucleotide exchange with intrinsic and SOS mediated nucleotide exchange assays. The intrinsic nucleotide exchange assay used BGTP and monitored a change in fluorescences when bound to KRAS. We found that as the concentration of **M1** increased the rate of uptake of BGTP also increased relative to the vehicle control (**Figure 4.4**). This indicates that **M1** binds to KRAS and enhances GTP loading. Second, in a similar assay that included SOS, an enzyme that catalyzes GDP release, we observed an increase in uptake followed by a decrease in the rate of BGTP loading. This data could indicate that **M1** binds to SOS and enhances activity, which is consistent with other reports of a small molecule that bind SOS near the catalytic site and enhance nucleotide exchange of KRAS [128]. The increase in GTP loading at lower concentrations was consistent with our short incubation signaling data at similar concentrations (**Figures 4.2 & 4.4B**). Enhanced GTP loading, even in the case of mutant KRAS, can increase signaling. However, during long incubation with **M1** in BHK cells at 100 µM we see a decrease in KRAS signaling by western blot, a result that is consistent with the decrease in nucleotide exchange at high **M1** concentrations (50 µM in these experiments). The disruption of SOS mediated GDP turnover could result in less active KRAS in the cells. This would subsequently decrease KRAS signaling, a result that is consistent with our signaling data (**Figure 4.2B, bottom**).
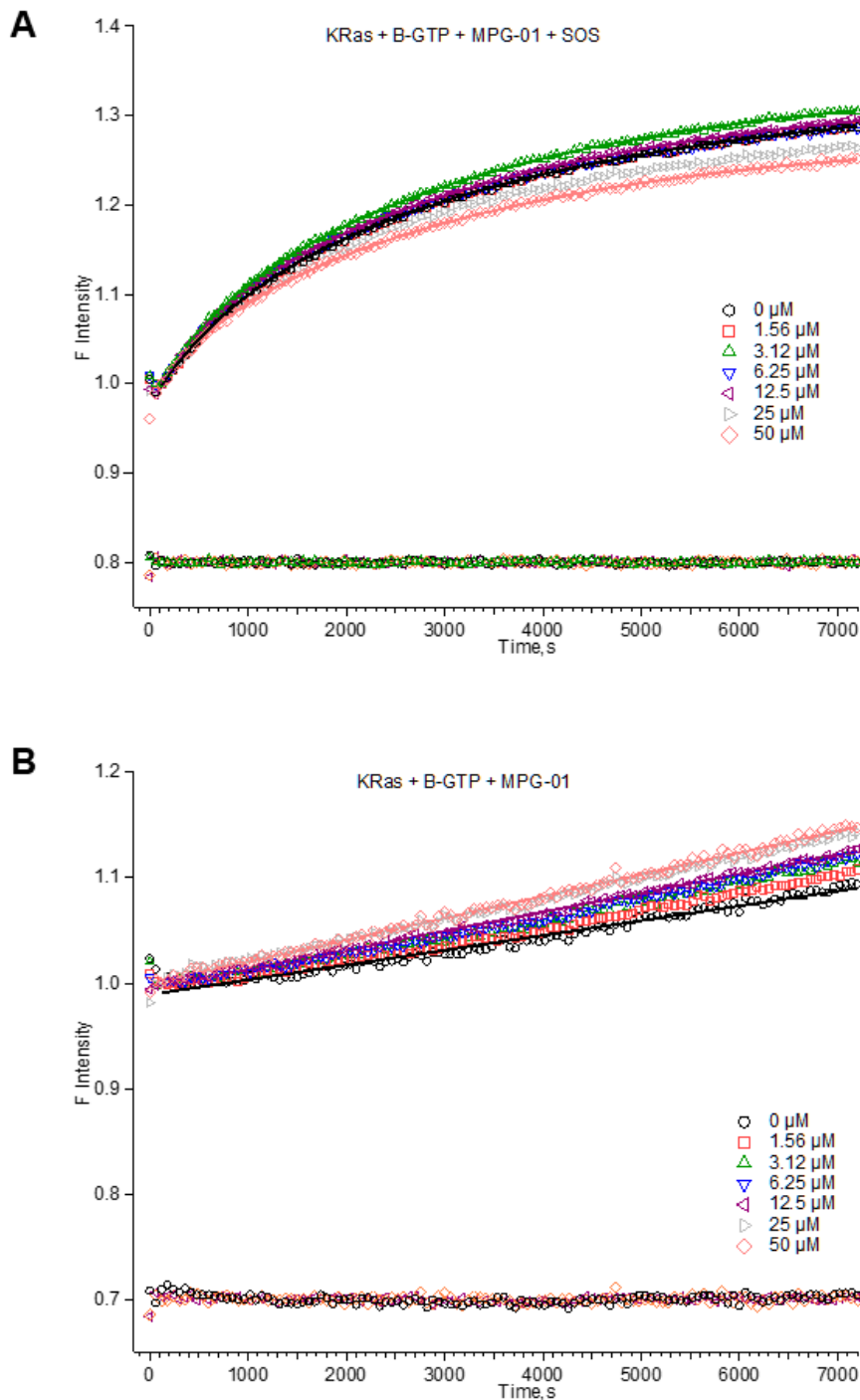
Figure 4.4: M1 changes nucleotide exchange (**A**) The rate of GTP binding during intrinsic nucleotide exchange is enhanced with **M1**. (**B**) The rate of SOS catalyzed nucleotide exchange is demonstrating that **M1** could enhance the level of GTP bound KRAS at low micromolar treatment. The rate of nucleotide exchange then reverses at high concentrations of **M1** indicating **M1** also inhibits SOS activity. (work and figures by Cynthia Pagba)

4.6 Pancreatic cancer cell proliferation is reduced by M1.

To test compound **M1** in human cancer cells we chose a panel of 3 lung cancer cells including H522 and H1975 (both expressing wild type KRAS) and SKLU-1 cells which express $KRAS^{G12D}$. Although these experiments remain unfinished, the data shown in **Figure 4.5** indicate some reduction in growth at the highest concentration suggesting that these cells are sensitive to this compound. Additionally, we tested compound **M1** with two pancreatic cancer cell lines, Miapaca-2, (driven by $KRAS^{G12C}$) and Bxpc-3, which are wild type for KRAS. The compound inhibited growth of Miapaca-2 cells with an IC_{50} of 6.8μM (**Figure 4.5A, left**). Therefore, this led us to hypothesis that $KRAS^{G12C}$ may be the best target for this compound. Indeed, this compound shares ~73% similarity with compound 21S (PDB 4M1Y), a molecule that covalently binds to $KRAS^{G12C}$ and was developed by Ostrem *et al.* (ref).
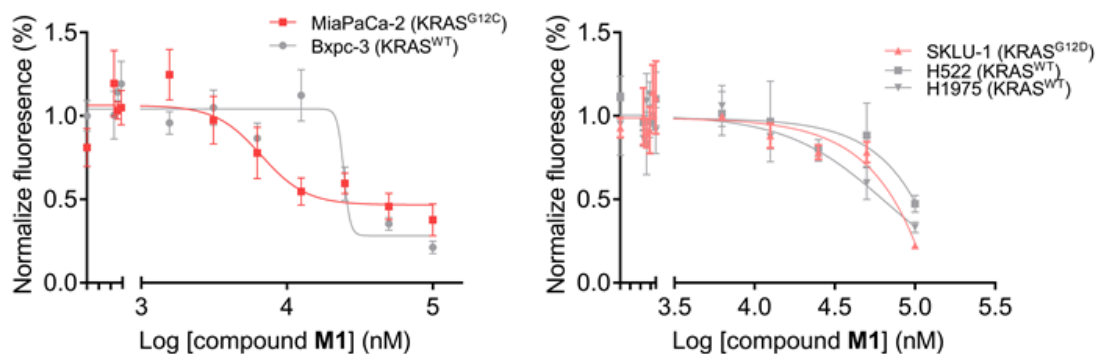
Figure 4.5: Cancer cell proliferation reduced by M1 (**A**) (left) Pancreatic cancer cells were treated with **M1** for 48 h and then cell proliferation was measured with CyQuant assay. With an estimated IC_{50} of 6.6 µM the KRAS mutant dependent MiaPaCa-2 cell line is more sensitive to **M1** then the $KRAS^{WT}$ Bxpc-3 cell line (estimated IC_{50} 24 µM). Relative proliferation is plotted with error bars representing the standard error of the mean for two trials with three replicate wells per trial. (**A**) (right) A panel of 3 lung cancer cell lines treated for 72 h with indicated concentrations of **M1**.

4.7 Biophysical assays indicate M1/KRAS binding.

Compound **M1** was subject to a small battery of biophysical assays starting with microscale thermophoresis (MST), which indicated high affinity binding with an initial K_D of ~2 μM. Compound **M1**, is seen in its predicted binding mode in **Figure 4.6 A**. The central indazol core that sits in the space between the effector loop and switch 2 is similar to some known binders that disrupt GEF-mediated nucleotide exchange [118]. However, attached to that core structure is a unique piperazine moiety that hydrogen bonds with E37 holding the molecule tightly in the pocket.

Second, in work done by Dr. Wang, a research scientist in Dr. Putkey's lab, we have used NMR to determine the binding site of this molecule. Starting with N_{15} labeled $^{GDP}KRAS^{WT}$ we were able to generate a Heteronuclear Single Quantum Coherence (HSQC) spectra of KRAS shown in **Figure 4.6 B.** The H_1 and N_{15} cross peaks generated by amide chemical shifts attribute to the protein backbone amides and spreading of cross peaks in the nitrogen dimension and hydrogen dimension indicates uniform average structure.

We then titrated in compound **M1** to a final molar ratio of 10 : 1 of compound to protein and observed amide chemical shifts perturbations in residues 37, 74 and 75. Interestingly, there were further perturbation in those residues as the concentration of compound increased. The amide chemical shift perturbations at the p1 pocket site could be the result of M1 binding thus validating the success of our focused design efforts with the HTVS. In **Figure 4.6 A** the pose of molecule **M1** in pocket p1 is shown. Major residues of the pocket were labeled and those highlighted in red showed the greatest amide chemical shift perturbation. The image in **Figure 4.6 B** is of HSQC spectra of amide chemical shift cross peaks generated by $^{GDP}KRAS^{WT}$ with **M1** at three

concentrations. The starting spectra, shown in blue, was taken before the addition of compound and then the purple at 5 : 1 and the red at 10 : 1, compound to protein molar ratio.
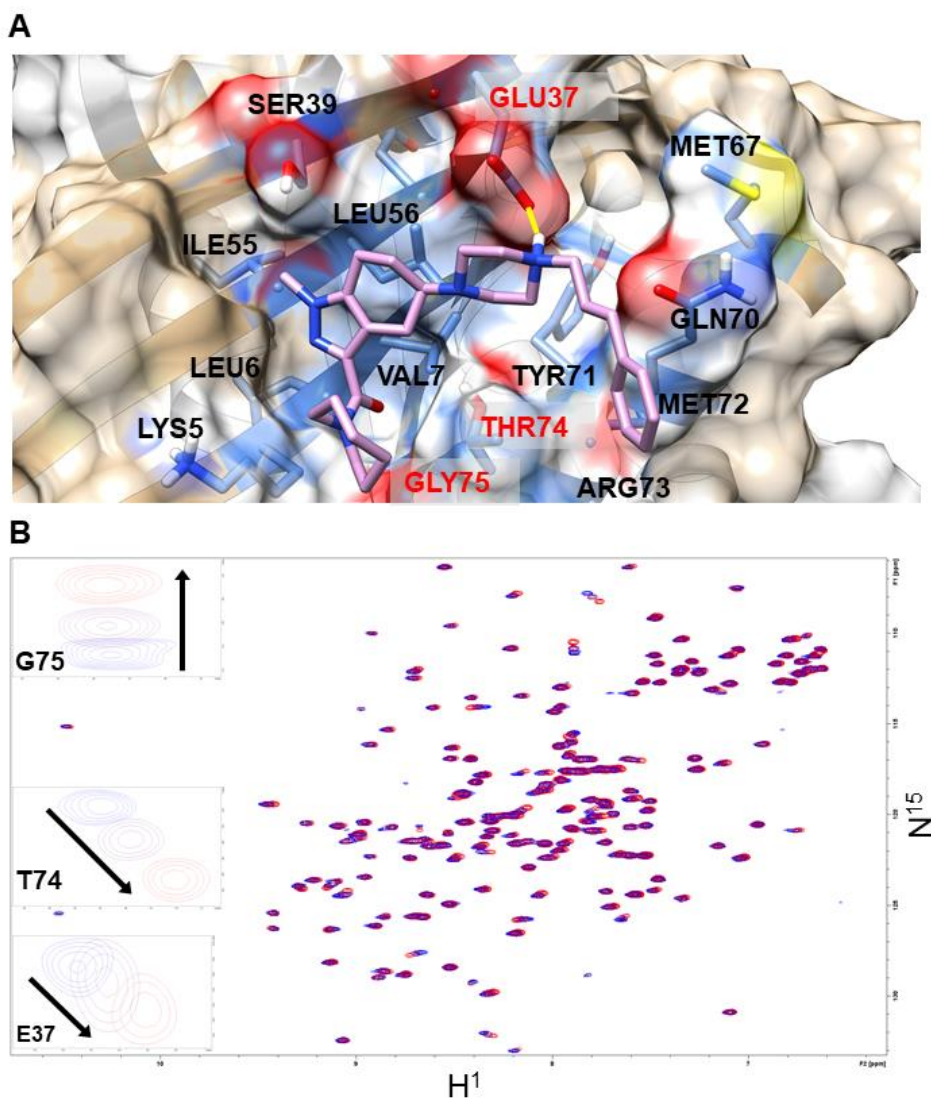
Figure 4.6: NMR confirms predicted binding mode of M1. (**A**) Predicted binding mode of compound **M1** in a conformation of pocket p1 of KRAS^{G12D} that was used for docking and generated by MD simulations. A hydrogen bond with E37 is highlighted in yellow and the residues of the pocket are labeled in black. Key residues that coincide with those that exhibited amide chemical shifts in NMR are highlighted in red. (**B**) An overlay of three NMR, HSQC spectra of H$_1$ and N$_{15}$ labeled KRAS^{WT} alone and then with the addition of increasing molar ratios of compound **M1**. The blue spectra is from KRAS^{WT} alone and the purple is with the addition of **M1** at 5 x KRAS^{WT} and the red is **M1** at 10 x KRAS^{WT}. The insets show amide chemical shifts pertubations detected in p1 residues glycine 75 (top), tyrosine 74 (middle) and glutamate 37 (bottom).

4.8 Conclusion

A pilot screen of a few molecules during the HTVS generated a potential new hit, compound **M1**, which was used as the basis for a smaller similarity-screen for novel KRAS inhibitors. Over 3,000 similar molecules from PubChem were screened through pocket p1 of KRAS^{G12D}. After redocking and analysis we ordered the top 13 available molecules to test in cell-based and biophysical assays. From testing we were able to identify 1 new potential inhibitor and determine that the parent compound **M1,** demonstrates a biphasic effect on KRAS^{G12D} signaling. Although the new inhibitor proved inconsistent, the data generated to-date with **M1** indicates that it binds to KRAS and alters signaling. However, with SOS mediated nucleotide exchange assays we observe an increase in BGTP binding suggesting **M1** may also be bind to SOS. Additionally, at low micro-molar concentrations and during short incubations we observed elevated KRAS signaling in western blotting as shown by increased p-CRAF and p-ERK levels. These results are consistent with enhanced SOS mediated KRAS activation and enhanced dimerization observed by RICS analysis. We interpret this result as a hormesis response, in which many small molecules can have different effects on cells depending on concentration. The hormesis response is hypothesized to be attributed to a molecule binding two targets. Our NMR results confirm **M1** binds to KRAS, while results from the nucleotide exchange assay may indicate **M1** binds to SOS. Therefore, at low concentrations **M1** may target SOS first, then at high concentrations it targets KRAS.

Chapter 5: Discussion and Future Directions

5.1 Discussion

Breaking through the "undruggable" wall to reach KRAS has been a major challenge in the search for cancer therapies. Previous attempts at therapeutically attacking KRAS focused on inhibiting farnesyl transferase (FTI's), which prevented the farnesylation and membrane anchoring of KRAS. Although initially effective in studies, FTI's ultimately failed in clinical trials [40]. It was later discovered that KRAS can be alternatively lipid modified by the geranylgeranylation, which bypasses the need for a farnesyl group as a lipid anchor [51]. More recent efforts focused on the dynamics of KRAS and revealed allosteric pockets suitable for binding of small molecules [20; 73]. Ground breaking fragments, such as DCAI and the fragment-like molecule developed by Sun et al., were shown to bind to p1 and disrupt KRAS interaction with SOS [118]. Further, small-molecules such as p4 binding andrographolides will decrease SOS mediated nucleotide exchange, ultimately resulting in decreased signaling through a buildup of GDP bound KRAS [77; 82]. The Kobe molecules were shown by X-ray crystallography to bind to p1 and decrease KRAS signaling though disruption of effector binding [75]. However, thus far none of these ligands have led to a viable lead compound.

Our approach to structure-based drug design for new KRAS inhibitors combined MD simulations with HTVS of "drug-like" molecules. By starting with MD simulations of KRAS^{G12D} we were able to identify conformations of the protein with open pockets that were not available in starting crystal structures at the time. Our efforts led to the identification of a small molecule, compound **11**, which directly binds KRAS^{G12D} and WT KRAS with nanomolar affinity. Compared with published KRAS binders that target pocket

p1 (25, 26), compound **11** (2-[4-(8-methyl-3,9-diphenyl-2,6,7-triazabicyclo[4.3.0]nona-2,4,7,9-tetraen-5-yl)piperazin-1-yl]ethanol) exhibits a number of unique structural and biochemical properties. First, compound **11** is more drug-like (drug-likeness = 4.1) and more polar with 6 hydrogen bond donors and 2 acceptors (cLogP = 0.87). Second, it has a pyrazolopyrimidine core rather than indole or imidazole rings common in the published ligands. Thirdly, compound **11** is relatively large (415 Da) with its pyrazol ring methylated and benzoylated and its pyrimidine ring beta-modified by benzene and 1-piperazineethanol. This allows **11** to make more extensive contacts with KRAS residues than is common in most of the previously published ligands (**Figure 3.3C**). Biochemically, compound **11** inhibits MAPK signaling by almost completely abrogating interaction with effector proteins (**Figure 3.4**), in contrast to many published KRAS ligands that primarily affect GEF activity (24-26). In **Figure 5.1** we aligned the KRAS^{G12D} conformation that was used for docking with docked pose of compound **11**, to an HRAS:CRAF^{RBD} complexed crystal structure (PDB 4G0N) [149]. This alignment shows that pocket p1 of HRAS is open and the side chains of each residue are in very similar arrangement with the KRAS^{G12D} conformation. This suggests that we have captured a potentially necessary conformation of KRAS for effector interaction in our simulation. Compared to other known binders the piperazineethanol group is a new feature, essentially it is a bulky ring structure that fills the space between E37 and S39 potentially limiting their movement. Together, the piperazine and the ethanol form two hydrogen bonds with E37, or alternately one with S39 and one with E37. In this alignment, 11 would prevent the interaction between KRAS and CRAF because it clashes with R67 of CRAF. Further, our testing confirms the other hallmarks of binding to pocket p1 on KRAS are intact, specifically nucleotide exchange by SOS is decreased. We also see this compound alters

the nucleotide free state of KRAS and decreases its affinity for GTP, but does not disrupt GDP release [150; 151].

Additionally, compound **11** is toxic to human cancer cells with great potency and for some cancer types it discriminates between KRAS^{mut} cells and wild-type dependent KRAS cells, albeit weakly. Finally, the toxicity observed in cells may not be solely caused by off target effects. We predict this compound switches KRAS signaling from pro-survival to pro-apoptosis by enhancing interaction with RASSF6, an effector of KRAS that initiates apoptosis through the MOAP/Bax pathway [152; 153]. A prediction that is supported by our data showing enhanced pulldown of RASSF6 (**Figure 3.6**).
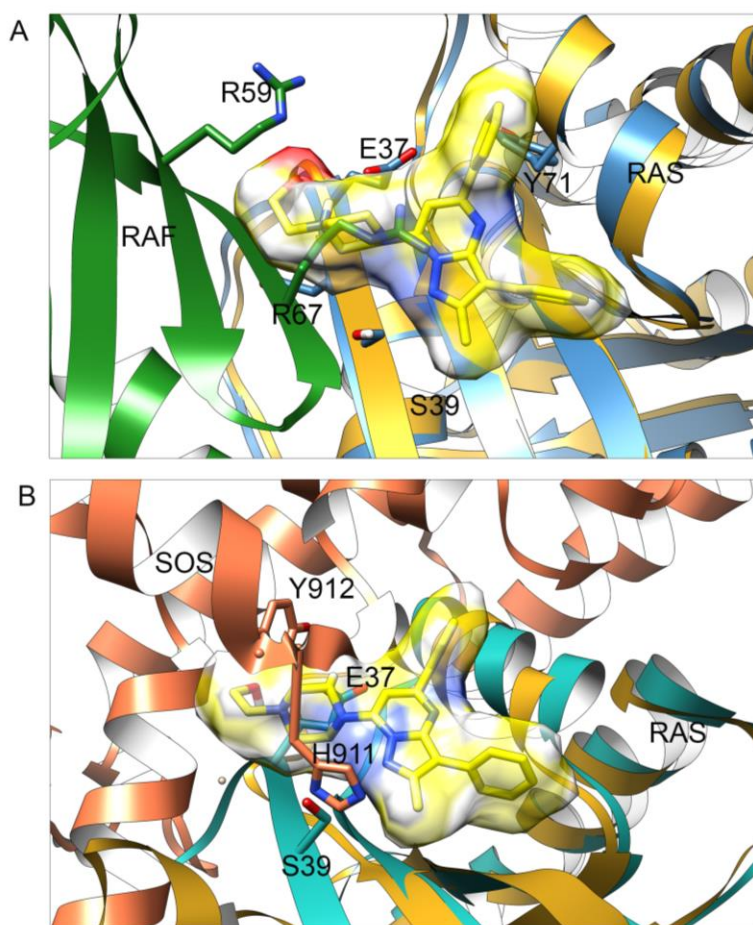
Figure 5.1: KRAS^{G12D} with compound 11 docked aligned to crystal structures of RAS and effector complexes. (**A**) Superimposition of the X-ray structure of the HRAS:Raf complex (PDB 4G0N, green and yellow) with our predicted KRAS-compound **11** complex (KRAS in cyan and ligand in yellow). The ligand clashes with residues R59 and R67 of Raf and competes for H-bonding to E37, and potentially blocks the interaction between R89 of Raf and D38 of RAS.KRAS^{G12D} aligned with HRAS:Raf cocrystal. (**B**) Superimposition of the structure of HRAS:SOS complex (PDB 1BKD, coral and gold, respectively) and predicted KRAS-compound **11** complex (cyan and yellow, respectively). Notice the significant overlap between the core of compound **11** (especially the pyrimidine-bound phenyl ring) and SOS, consistent with the observed reduction in the rate of SOS-mediated nucleotide exchange and release reactions shown in **Figure 3.7**. Also, note the potential of the ligand to form hydrogen bonds with H911 and Y912 of SOS, which may explain the enhanced rate of SOS-mediated nucleotide release observed in compound **13** that lacks the ring clashing with SOS.

A second compound to come out of the primary screen was **M1,** which demonstrated binding to KRAS in NMR experiments. This compound contains an indazole core that is a little more similar to other published binders than the compound **11** core. The molecule **M1** (azepan-1-yl-[1-methyl-5-[4-[(E)-3-phenylprop-2-enyl]piperazin-1-yl]-4,5,6,7-tetrahydroindazol-3-yl]methanone) has a drug-likeness score of 2.9, with 6 hydrogen bond donors and 1 acceptor, the molecule weight is 462 Da. Compared to compound **11** this compound has demonstrated a biphasic effect of p-ERK levels and was less potent at decreasing p-ERK levels and inhibiting cancer cell growth. However, during long incubation, at all concentrations, it caused a consistent decrease in p-AKT levels.

To gain insight into the structural basis for our biochemical data we superimposed KRAS^{G12D} with **M1** docked onto crystal structure of RAS in complex with effectors. The docked pose of compound **M1** was align with the crystal structure of HRAS:RBD of cRaf (PDB 4G0N) (**Figure 5.2**) [149]. For compound **M3** the piperazineethanol found in compound **11** is replace with a carboxamide group. Without a bulky group to fill the space between S39 and E37 and the loss of hydrogen bonds to those residues, **M1** may not be able to interfere with R67 nor R59 of Raf. Therefore, it probably cannot disrupt KRAS interactions with CRaf, like compound **11**. This conclusion is supported by our signaling and FLIM-FRET data (see **Figure 4.2 & 4.3 A)**. Similarly **M1** docked on KRAS^{G12D} was superimposed on to the HRAS:PI3K crystal structure (PDB 1HE8 **Figure 5.2 A**). **M1** interacts with switch II and effector loop residues which could limit their rearrangement and it could clash with K223 of PI3K preventing a hydrogen bond with E37 [154]. However, in this complex HRAS is bound to the p110γ subunit of PI3K and residue 223 was mutated from valine to lysine. The authors describe this change as analogous to

endogenous K206 of the p110α subunit that typically binds KRAS [154]. Therefore, I docked **M1** on to HRAS in this complex and then superimposed a crystal structure of the p110α (PDB 4TUU) subunit [155]. Shown in **Figure 5.2 A**, although the full side chain of K206 is not present, **M1** (shown in blue docked on HRAS) forms a hydrogen bond with S39 that would prevent K206 from interacting with E37. The score for this pose is not significantly lower than the pose on KRAS (**Figure 5.2** (**A**) **M1** is in green). The position of the molecule and the clashes it would form with PI3K may prevent KRAS from interacting with PI3K, a conclusion supported by reduced cellular p-AKT levels in our long incubation experiments. However, binding directly to KRAS at low concentrations is inconsistent with our p-ERK signaling data and SOS mediated nucleotide exchange data. Other possibilities should be considered such as binding directly to the p110α subunit of PI3K and disrupting binding to KRAS.

M1 was evaluated in a third alignment to the HRAS:SOS crystal structure (1NVV) [156]. The alignment allows for a comparison of HRAS to KRAS and it is obvious that a significant change in the position of the switch I residues (R42 to Y32) of HRAS has occurred (**Figure 5.2B**). However, compound **M1** forms a hydrogen bond with the side chain of E37 which could lock the molecule and E37 together in the pocket, in this case it might prevent SOS activity or even binding. Additionally, a possible pi-cation stacking interaction with Q70 and the terminal benzene of **M1** could prevent the rearrangement of R73 possibly eliminating a necessary stacking interaction with Y884 [128]. This along with a potential clash between **M1** and H911 could explain a decrease nucleotide exchange and decreased signaling by buildup of ^{GDP}KRAS. Conversely, at low micro-molar concentrations we observe an increase in SOS mediated nucleotide exchange. Recently other groups have reported small molecule that bind to SOS and enhance

nucleotide exchange. The binding spot on SOS is a small pocket near the interface between KRAS and SOS [128]. I docked **M1** on the crystal structure generated in that study (PDB 4NYJ) and found that the **M1** fits in the pocket in a similar orientation to 2PZ [128]. **M1** also forms a hydrogen bond with Y884 possibly stabilizing it in a pi-stacking interaction with R73 of RAS (**Figure 5.3**). Considering our results, it could be possible that **M1** binds to the same pocket and enhances SOS activity.
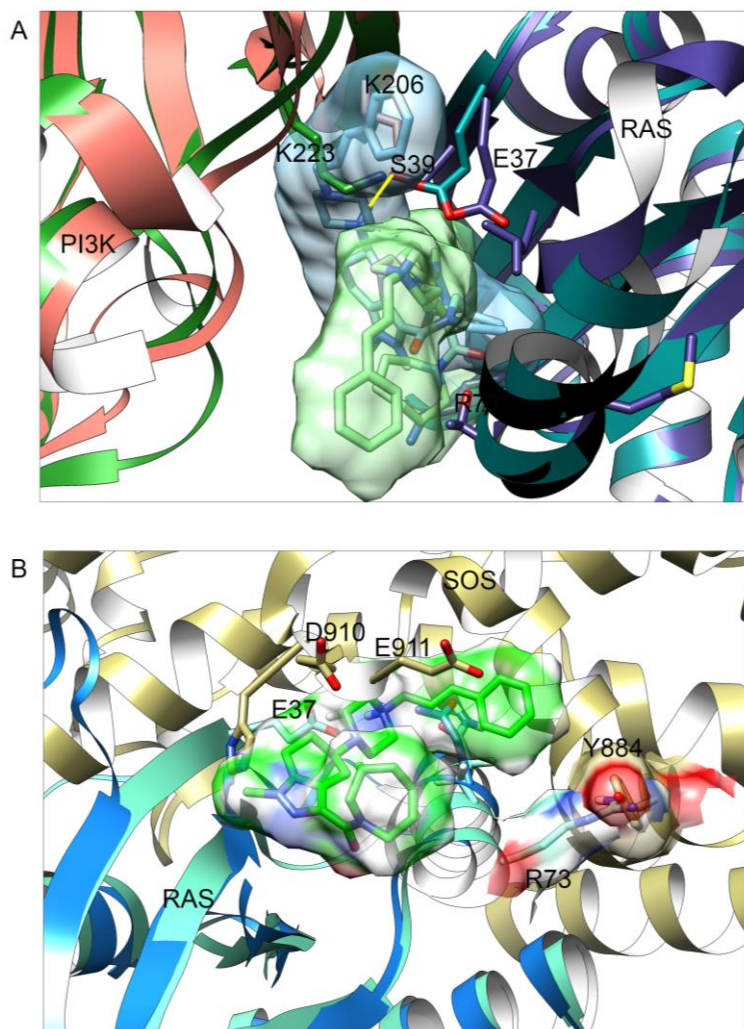
Figure 5.2: Compound M1 docked to KRAS and superimposed on to HRAS crystalized in complex with PI3K or SOS. (**A**) KRAS^G12D (blue) with **M1** (green) docked is superimposed on to HRAS^G12V (purple) with **M1** docked (light blue) that was cocrystalized with PI3K p110γ (green) (PDB 1HE8) and the crystal structure of PI3K p110α (coral color, PDB 4TV3) was superimposed onto the p110γ subunit. A hydrogen bond is highlighted in yellow between **M1** and the sidechain of S39 of HRAS^WT. In the illustration only, part of K206 survived crystallization but I predict the end of the side chain would clash with **M1** which could limit binding. (**B**) HRAS^WT (blue) crystalized with SOS (khaki) with KRAS^G12D (teal) and **M1** (green) superimposed. The ligand in this position could limit the movement of R73, forcing it to stay extended and potentially clashing with Y884. This clash along with clashes with residues 912 and 911 could disrupt binding and therefore nucleotide exchange.

Derivatives of compound **11** and **M1** give insight into the mechanism of activity**.** First, we tested compound **13,** a derivative of **11** in which a benzene ring is replaced with a methyl group. Compared to **11**, we observe changes in affinity, potency and enhances in both intrinsic and SOS mediate nucleotide release rates. Comparison of the docked poses of **11** (**Figure 3.3C**) and **13** (**Figure 3.9B**) provided a rationale for the observed differences in binding affinity. The benzene ring of compound **11** is involved in a T-shaped π-stacking interaction with the side chain of Y71, which is replaced by methyl in compound **13** so that interaction is lost. The methyl is also too small to fill-up the space above Y71, which means **13** may not fit as tightly as compound **11** in the pocket and we then lose some hydrophobic contacts with the pocket. Additionally without this ring compound **13** may not clash with SOS residues H911 and Y912 thus it could actually then stabilize the SOS:KRAS complex. However, we retain disruption of RAF-RBD binding and this is supported by our structural analysis (**Figures 3.3C and 3.9B**), which shows that compounds **11** and **13** make identical contacts with residues at the effector-binding region via their piperazine ring and especially the piperazineethanol group.

The predicted binding mode of another derivative, compound **12,** is very similar to that of **11** and **13**, with the key difference being that compound **12** lacks hydrogen bonding interactions with residues at the effector binding loop (**Figure 3.5B**). Specifically compound **12** lacks the alcohol group and therefore only forms hydrogen bonds with the sidechain of E37, and although we lose the effect on p-cRaf levels that **11** causes, we do observe a significant decrease in p-ERK levels at 2μM.

Next for consideration is molecule **M3** (1-benzyl-N,N-dimethyl-5-[2-(4-phenylpiperidin-1-yl)ethylamino]-4,5,6,7-tetrahydroindazole-3-carboxamide) a derivative of **M1** The docked pose is shown in **Figure 5.3.** The functional features of this molecule

are central indazole with a piperdine, attached through an ethylamino linker, the piperdine makes a hydrogen bond with E37 (highlighted in yellow **Figure 5.3B**). Additionally, attached to the indazole is a carboxamide group that rests partially between S39 and E37 like the piperazine of compounds **11**, **12** and **13**. However, in contrast to those molecules the carboxamide cannot form hydrogen bonds with either residue nor does it fill up the space between residues. Therefore, the carboxamide group may be too small to effect S39 and E37 as significantly as the piperazineethanol of compound **11** and **13**. Similar to compound **12** we observe a small decrease in p-ERK levels but at more than 10-fold higher concentration, indicating the importance of the entire piperazineethanol moiety and the hydrogen bonds it makes. Together, these results indicate that the ethanol moiety on the piperazine ring, which forms a hydrogen bond with E37 or S39 of the effector-binding loop (**Figure 3.3C**), is crucial for disrupting interaction of RAS with CRAF.

Further insights into the benzene to methyl change in **11** and **13** can be gained by considering the differences between **M1** and **M3** and the other three compounds. For the **M** molecules the benzene is extended away from the central core with a linker attached a piperdine for **M1,** however for **M3** the linker is between the piperdine and the core of the molecule, therefore the benzene becomes part of a bulkier group. In either case the stacking interaction with Y71 is most likely lost. For **M3** the large piperdine-benzene group maybe be too large to occupy the space between E37 and M67 and too long to fit in the pocket (**Figure 5.4**). Without a trench or pocket shielding the hydrophobic benzene from the aqueous environment, the molecule may be too unstable to stay bound to KRAS except at high concentrations. Although these compounds are capable of similar interactions with p1 residues as compound **11** or **13**, the penalty for the solvent

exposed benzene and lack of additional h-bonds with S39 or E37 may be the source of inconsistency and low effect observed during cell-based testing. Together, these findings demonstrate the critical role of the benzene ring on the pyrazolopyrimidine core of **11** and **13** plays by interacting with Y71 to enhance potency and selectivity, providing a useful handle for future optimization efforts.

In summary, our comparative analyses of compounds **M1**, **M3**, **11**, **12** and **13** allowed us to unambiguously determine the mechanisms by which **11** simultaneously abolishes effector binding and modulates intrinsic and GEF-mediated nucleotide exchange reactions. Indeed, superposition of our predicted ligand-bound KRAS structure onto the HRAS:SOS complex (PDB 1NVV) suggests stabilization of the ternary complex (**Figure 3.4**). For example, side chains of H911 and Y912 of SOS are within a H-bonding distance from nitrogen atoms on the pyrazolopyrimidine ring of **11**. Additionally, as discussed the 1-piperazineethanol prevents CRaf binding by blocking the RBD from interacting with effectors residues of switch 1. Compound **11** and derivatives **12** and **13** are the next step in targeting KRAS with small molecules. Compound **11** binds with nanomolar affinity and is effective at disrupting KRAS-effector interaction at low micro-molar concentrations in *in-vivo* and biophysical experiments, a remarkable success for an initial screening effort. A second compound, **M1** may be a good starting point for further optimization since it has a strong effect on p-AKT levels during long incubation at very low micromolar concentrations. Additionally, our RICS data indicates this compound enhances KRAS dimerization, and we see enhanced nucleotide exchange in biophysical assays. Together, these observations bring about the possibility of a new experimental tool. Finally, these results also provided a strong support for the reliability of the predicted

ligand-KRAS complex structures, and offered a viable route for additional modifications

in future optimization efforts.
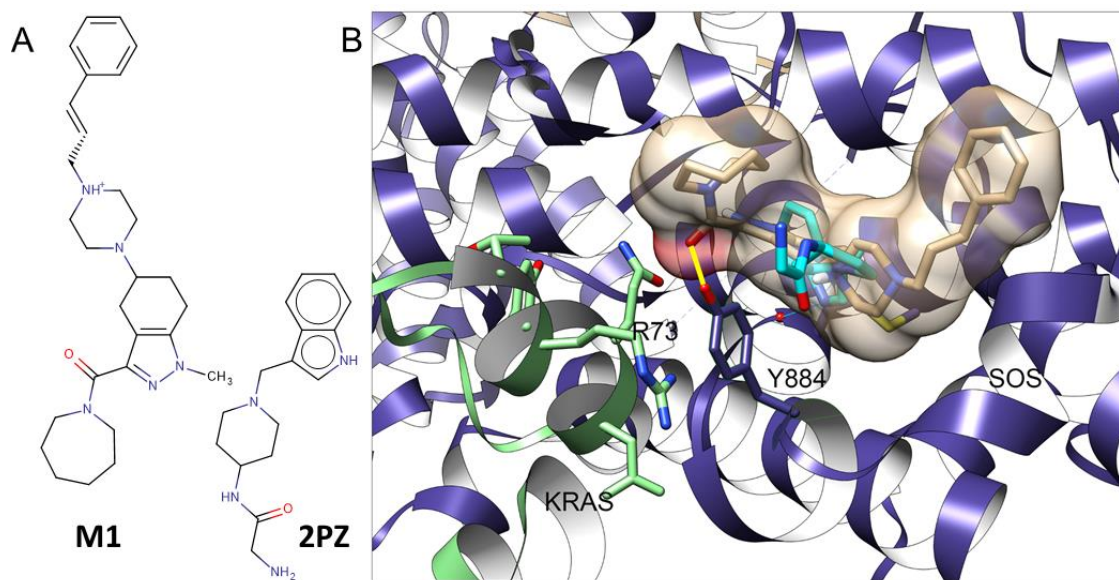
Figure 5.3: M1 docked on to SOS with 2PZ in a pocket near KRAS binding domain. (**A**) The structure of **M1** and 2PZ, they share a similar core indole group. (**B**) Compound **M1** (tan) and 2PZ (blue) bound to SOS in a pocket near the KRAS catalytic interaction site. Compound **M1** forms a hydrogen bond (highlighted in yellow) with Y884 (purple) of SOS, possibly stabilizing it in a π-stacking interaction with R73 (green) of KRAS.
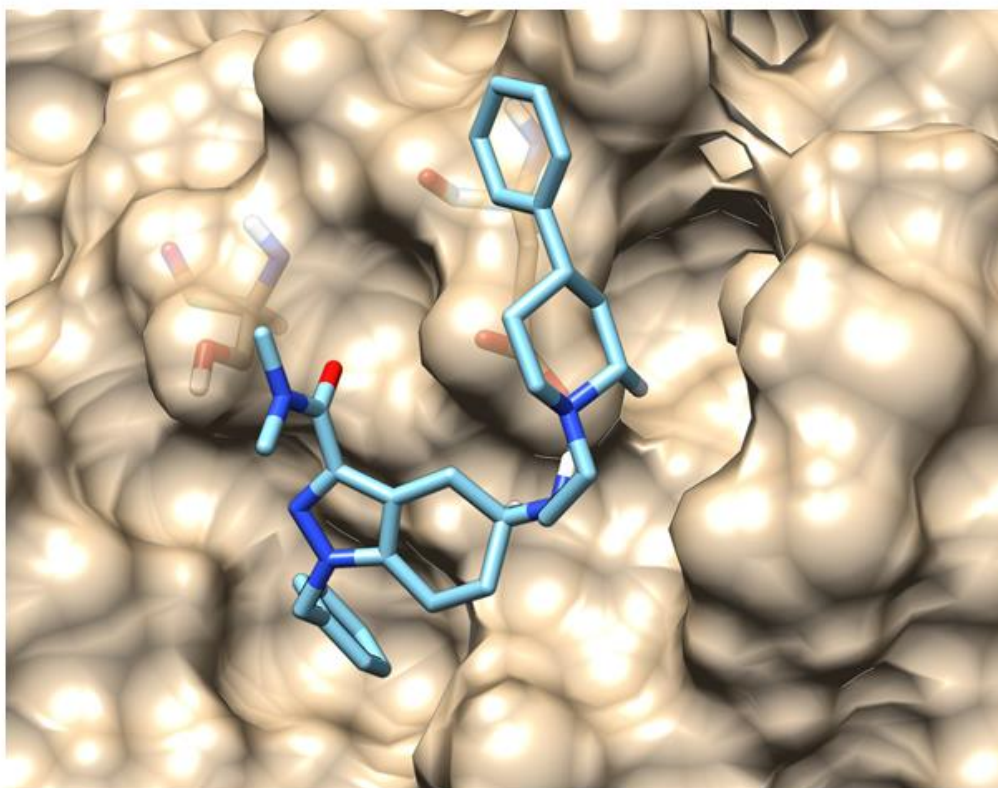
Figure 5.4: Compound M3 docked to KRAS^G12D Surface representation of KRAS^G12D (tan) and compound **M3** (blue). The caboxamide group attached to the central indazole rests between S39 and E37 although it does not fill up the space nor does it form any high affinity interactions with either residue. The ethylamino forms a hydrogen bond with E37 but the piperdine-benzene group wraps around E37 rather than occupy the gap between E37 and M67. The solvent exposed benzene is an unfavorable interaction that would reduce binding affinity.

5.2 Future directions

Compound **13** should be thoroughly evaluated in cell-based assays. Preliminary testing indicated a decrease of p-ERK levels occurred at 1 µM treatment of BHK cells expressing GFP-KRAS^{G12D} after 3 hr in serum free media. Although more soluble then compound **11** we used 10 µM of **13** to disrupt GFP-KRAS^{G12D} binding in pulldown assays. Therefore, in signaling experiments the concentration range should be from 1 to 20 µM to determine if the compound can cause more than the ~50% reduction typically observed. Along with 2D cell proliferation assays with **13**, compound **11** and **13** should be testing in 3D cell proliferation assays. I would start with SKLU-1 and H1975 cells as a first test, since we saw the greatest difference in IC$_{50}$ in compound **11** experiments. Finally, compound **11** and **13** should be used for similarity searches and new molecules based on these could be screened and tested.

It was demonstrated with NMR that compound **M1** does bind to KRAS^{WT} probably at the p1 site and western blots indicate it decreased p-AKT after long incubation. This indicates **M1** should be explored further, although it needs to be resynthesized. The next steps would be gathering additional signaling data from long incubation experiments. To assess whether **M1** disrupts PI3K binding to KRAS, pulldown experiments with p110α, the subunit of PI3K, should be performed. Finally, the molecule could be optimized by removing the terminal benzene and rationally designing a functional group to interact with the residues that form the trench between E37 and M67.

Molecule **M3** was initially promising and has some features that make it attractive. Removing the terminal benzene would probably improve its binding. Further the

carboxamide group could be lengthened with a short carbon-chain and this might allow it to hydrogen bond with S39 or G37 and improve its activity. Additionally, the methyl groups on the amine could be removed to improve solubility and add hydrogen bond potential. Finally, it could be used as the basis for a similarity search to generate a new group of potential binders to be screened in a small high throughput virtual screen and then a small cell-based screen.

References

1   (2018). Cancer facts and figures 2018. American Cacner Society.

2   Hanahan, D., and Weinberg, R.A. (2011). Hallmarks of cancer: the next generation. Cell *144*, 646-674.

3   Bister, K. (2015). Discovery of oncogenes: The advent of molecular cancer research. Proceedings of the National Academy of Sciences of the United States of America *112*, 15259-15260.

4   Der, C.J., Krontiris, T.G., and Cooper, G.M. (1982). TRANSFORMING GENES OF HUMAN BLADDER AND LUNG-CARCINOMA CELL-LINES ARE HOMOLOGOUS TO THE RAS GENES OF HARVEY AND KIRSTEN SARCOMA-VIRUSES. Proceedings of the National Academy of Sciences of the United States of America-Biological Sciences *79*, 3637-3640.

5   Der, C.J. (1987). Cellular oncogenes and human carcinogenesis. Clinical chemistry *33*, 641-646.

6   Prior, I.A., Lewis, P.D., and Mattos, C. (2012). A comprehensive survey of Ras mutations in cancer. Cancer Res *72*, 2457-2467.

7   Barbacid, M. (1987). Ras Genes. Annu Rev Biochem *56*, 779-827.

8   Karnoub, A.E., and Weinberg, R.A. (2008). Ras oncogenes: split personalities. Nat Rev Mol Cell Biol *9*, 517-531.

9   Willingham, M.C., Pastan, I., Shih, T.Y., and Scolnick, E.M. (1980). Localization of the src gene product of the Harvey strain of MSV to plasma membrane of transformed cells by electron microscopic immunocytochemistry. Cell *19*, 1005-1014.

10   Hancock, J.F., Magee, A.I., Childs, J.E., and Marshall, C.J. (1989). All ras proteins are polyisoprenylated but only some are palmitoylated. Cell *57*, 1167-1177.

11   Cadwallader, K.A., Paterson, H., Macdonald, S.G., and Hancock, J.F. (1994). N-terminally myristoylated Ras proteins require palmitoylation or a polybasic domain for plasma membrane localization. Molecular and cellular biology *14*, 4722-4730.

12   Gibbs, J.B., Sigal, I.S., Poe, M., and Scolnick, E.M. (1984). Intrinsic GTPase activity distinguishes normal and oncogenic ras p21 molecules. Proceedings of the National Academy of Sciences of the United States of America *81*, 5704-5708.

13   Hoshino, M., Kawakita, M., and Hattori, S. (1988). Characterization of a factor that stimulates hydrolysis of GTP bound to ras gene product p21 (GTPase-activating protein) and correlation of its activity to cell density. Molecular and cellular biology *8*, 4169-4173.

14   Quilliam, L.A., Hisaka, M.M., Zhong, S., Lowry, A., Mosteller, R.D., Han, J., Drugan, J.K., Broek, D., Campbell, S.L., and Der, C.J. (1996). Involvement of the switch 2 domain of Ras in its interaction with guanine nucleotide exchange factors. The Journal of biological chemistry *271*, 11076-11082.

15   Schubbert, S., Shannon, K., and Bollag, G. (2007). Hyperactive Ras in developmental disorders and cancer. Nature reviews Cancer *7*, 295-308.

16   Taveras, A.G., Remiszewski, S.W., Doll, R.J., Cesarz, D., Huang, E.C., Kirschmeier, P., Pramanik, B.N., Snow, M.E., Wang, Y.S., del Rosario, J.D*., et al.* (1997). Ras oncoprotein inhibitors: The discovery of potent, ras nucleotide exchange inhibitors and the structural determination of a drug-protein complex. Bioorganic & Medicinal Chemistry *5*, 125-133.

17   McCormick, F., and Wittinghofer, A. (1996). Interactions between Ras proteins and their effectors. Current opinion in biotechnology *7*, 449-456.

18   Marshall, M.S. (1995). Ras target proteins in eukaryotic cells. FASEB journal : official publication of the Federation of American Societies for Experimental Biology *9*, 1311-1318.

19   Cox, A.D., and Der, C.J. (2010). Ras history: The saga continues. Small GTPases *1*, 2-27.

20   Gorfe, A.A. (2010). Mechanisms of allostery and membrane attachment in Ras GTPases: implications for anti-cancer drug discovery. Curr Med Chem *17*, 1-9.

21   Almoguera, C., Shibata, D., Forrester, K., Martin, J., Arnheim, N., and Perucho, M. (1988). Most human carcinomas of the exocrine pancreas contain mutant c-K-ras genes. Cell *53*, 549-554.

22   Jones, S., Zhang, X., Parsons, D.W., Lin, J.C., Leary, R.J., Angenendt, P., Mankoo, P., Carter, H., Kamiyama, H., Jimeno, A.*, et al.* (2008). Core signaling pathways in human pancreatic cancers revealed by global genomic analyses. Science *321*, 1801-1806.

23   Forrester, K., Almoguera, C., Han, K., Grizzle, W.E., and Perucho, M. (1987). Detection of high incidence of K-ras oncogenes during human colon tumorigenesis. Nature *327*, 298-303.

24   Riely, G.J., Marks, J., and Pao, W. (2009). KRAS mutations in non-small cell lung cancer. Proceedings of the American Thoracic Society *6*, 201-205.

25   Ball, N.J., Yohn, J.J., Morelli, J.G., Norris, D.A., Golitz, L.E., and Hoeffler, J.P. (1994). Ras mutations in human melanoma: a marker of malignant progression. The Journal of investigative dermatology *102*, 285-290.

26   Luo, D., Liu, Q.F., Gove, C., Naomov, N., Su, J.J., and Williams, R. (1998). Analysis of N-ras gene mutation and p53 gene expression in human hepatocellular carcinomas. World journal of gastroenterology : WJG *4*, 97-99.

27   van 't Veer, L.J., Burgering, B.M., Versteeg, R., Boot, A.J., Ruiter, D.J., Osanto, S., Schrier, P.I., and Bos, J.L. (1989). N-ras mutations in human cutaneous melanoma from sun-exposed body sites. Molecular and cellular biology *9*, 3114-3116.

28   Burchill, S.A., Neal, D.E., and Lunec, J. (1994). Frequency of H-ras mutations in human bladder cancer detected by direct sequencing. British journal of urology *73*, 516-521.

29   Castro, P., Soares, P., Gusmao, L., Seruca, R., and Sobrinho-Simoes, M. (2006). H-RAS 81 polymorphism is significantly associated with aneuploidy in follicular tumors of the thyroid. Oncogene *25*, 4620-4627.

30   Adari, H., Lowy, D.R., Willumsen, B.M., Der, C.J., and McCormick, F. (1988). Guanosine triphosphatase activating protein (GAP) interacts with the p21 ras effector binding domain. Science *240*, 518-521.

31   Vetter, I.R., and Wittinghofer, A. (2001). Signal transduction - The guanine nucleotide-binding switch in three dimensions. Science *294*, 1299-1304.

32   Scheffzek, K., Ahmadian, M.R., Kabsch, W., Wiesmuller, L., Lautwein, A., Schmitz, F., and Wittinghofer, A. (1997). The Ras-RasGAP complex: structural basis for GTPase activation and its loss in oncogenic Ras mutants. Science *277*, 333-338.

33   Cox, A.D., Fesik, S.W., Kimmelman, A.C., Luo, J., and Der, C.J. (2014). Drugging the undruggable RAS: Mission Possible? Nature reviews Drug discovery *13*, 828-851.

34   Engelman, J.A. (2009). Targeting PI3K signalling in cancer: opportunities, challenges and limitations. Nature reviews Cancer *9*, 550-562.

35   Welsch, M.E., Kaplan, A., Chambers, J.M., Stokes, M.E., Bos, P.H., Zask, A., Zhang, Y., Sanchez-Martin, M., Badgley, M.A., Huang, C.S*., et al.* (2017). Multivalent Small-Molecule Pan-RAS Inhibitors. Cell *168*, 878-889 e829.

36   Spencer-Smith, R., Koide, A., Zhou, Y., Eguchi, R.R., Sha, F., Gajwani, P., Santana, D., Gupta, A., Jacobs, M., Herrero-Garcia, E*., et al.* (2017). Inhibition of RAS function through targeting an allosteric regulatory site. Nat Chem Biol *13*, 62-68.

37   Gentry, L., Samatar, A.A., and Der, C.J. (2013). Inhibitors of the ERK mitogen-activated protein kinase cascade for targeting RAS mutant cancers. The Enzymes *34 Pt. B*, 67-106.

38   Adjei, A.A., Erlichman, C., Davis, J.N., Cutler, D.L., Sloan, J.A., Marks, R.S., Hanson, L.J., Svingen, P.A., Atherton, P., Bishop, W.R*., et al.* (2000). A Phase I trial of the farnesyl transferase inhibitor SCH66336: evidence for biological and clinical activity. Cancer Res *60*, 1871-1877.

39   Kohl, N.E., Omer, C.A., Conner, M.W., Anthony, N.J., Davide, J.P., deSolms, S.J., Giuliani, E.A., Gomez, R.P., Graham, S.L., Hamilton, K*., et al.* (1995). Inhibition of farnesyltransferase induces regression of mammary and salivary carcinomas in ras transgenic mice. Nature medicine *1*, 792-797.

40   Lobell, R.B., Omer, C.A., Abrams, M.T., Bhimnathwala, H.G., Brucker, M.J., Buser, C.A., Davide, J.P., deSolms, S.J., Dinsmore, C.J., Ellis-Hutchings, M.S*., et al.* (2001). Evaluation of farnesyl:protein transferase and geranylgeranyl:protein transferase inhibitor combinations in preclinical models. Cancer Res *61*, 8758-8768.

41   Zujewski, J., Horak, I.D., Bol, C.J., Woestenborghs, R., Bowden, C., End, D.W., Piotrovsky, V.K., Chiao, J., Belly, R.T., Todd, A.*, et al.* (2000). Phase I and pharmacokinetic study of farnesyl protein transferase inhibitor R115777 in advanced cancer. Journal of clinical oncology : official journal of the American Society of Clinical Oncology *18*, 927-941.

42   Mackenzie, G.G., Bartels, L.E., Xie, G., Papayannis, I., Alston, N., Vrankova, K., Ouyang, N., and Rigas, B. (2013). A novel Ras inhibitor (MDC-1016) reduces human pancreatic tumor growth in mice. Neoplasia (New York, NY) *15*, 1184-1195.

43   Rotblat, B., Ehrlich, M., Haklai, R., and Kloog, Y. (2008). The Ras inhibitor farnesylthiosalicylic acid (Salirasib) disrupts the spatiotemporal localization of active Ras: a potential treatment for cancer. Methods in enzymology *439*, 467-489.

44   Barkan, B., Starinsky, S., Friedman, E., Stein, R., and Kloog, Y. (2006). The Ras inhibitor farnesylthiosalicylic acid as a potential therapy for neurofibromatosis type 1. Clinical cancer research : an official journal of the American Association for Cancer Research *12*, 5533-5542.

45   Cho, K.J., Park, J.H., Piggott, A.M., Salim, A.A., Gorfe, A.A., Parton, R.G., Capon, R.J., Lacey, E., and Hancock, J.F. (2012). Staurosporines disrupt phosphatidylserine trafficking and mislocalize Ras proteins. J Biol Chem *287*, 43573-43584.

46   van der Hoeven, D., Cho, K.J., Ma, X., Chigurupati, S., Parton, R.G., and Hancock, J.F. (2013). Fendiline inhibits K-Ras plasma membrane localization and blocks K-Ras signal transmission. Molecular and cellular biology *33*, 237-251.

47   Cho, K.J., van der Hoeven, D., and Hancock, J.F. (2013). Inhibitors of K-Ras plasma membrane localization. The Enzymes *33 Pt A*, 249-265.

48   Zimmermann, G., Papke, B., Ismail, S., Vartak, N., Chandra, A., Hoffmann, M., Hahn, S.A., Triola, G., Wittinghofer, A., Bastiaens, P.I.*, et al.* (2013). Small molecule inhibition of the KRAS-PDEdelta interaction impairs oncogenic KRAS signalling. Nature *497*, 638-642.

49   Zimmermann, G., Schultz-Fademrecht, C., Kuchler, P., Murarka, S., Ismail, S., Triola, G., Nussbaumer, P., Wittinghofer, A., and Waldmann, H. (2014). Structure guided design and kinetic

analysis of highly potent benzimidazole inhibitors targeting the PDEdelta prenyl binding site. J Med Chem *57*, 5435-5448.

50   Baines, A.T., Xu, D., and Der, C.J. (2011). Inhibition of Ras for cancer treatment: the search continues. Future Med Chem *3*, 1787-1808.

51   Whyte, D.B., Kirschmeier, P., Hockenberry, T.N., Nunez-Oliva, I., James, L., Catino, J.J., Bishop, W.R., and Pai, J.K. (1997). K- and N-Ras are geranylgeranylated in cells treated with farnesyl protein transferase inhibitors. The Journal of biological chemistry *272*, 14459-14464.

52   Sosman, J.A., Kim, K.B., Schuchter, L., Gonzalez, R., Pavlick, A.C., Weber, J.S., McArthur, G.A., Hutson, T.E., Moschos, S.J., Flaherty, K.T.*, et al.* (2012). Survival in BRAF V600-Mutant Advanced Melanoma Treated with Vemurafenib. New Eng J Med *366*, 707-714.

53   Hauschild, A., Grob, J.-J., Demidov, L.V., Jouary, T., Gutzmer, R., Millward, M., Rutkowski, P., Blank, C.U., Miller, W.H., Kaempgen, E.*, et al.* (2012). Dabrafenib in BRAF-mutated metastatic melanoma: a multicentre, open-label, phase 3 randomised controlled trial. The Lancet *380*, 358-365.

54   Mandal, R., Becker, S., and Strebhardt, K. (2016). Stamping out RAF and MEK1/2 to inhibit the ERK1/2 pathway: an emerging threat to anticancer therapy. Oncogene *35*, 2547-2561.

55   Yeh, J.J., Routh, E.D., Rubinas, T., Peacock, J., Martin, T.D., Shen, X.J., Sandler, R.S., Kim, H.J., Keku, T.O., and Der, C.J. (2009). KRAS/BRAF mutation status and ERK1/2 activation as biomarkers for MEK1/2 inhibitor therapy in colorectal cancer. Mol Cancer Ther *8*, 834-843.

56   Mariati, Ho, S.C.L., Yap, M.G.S., and Yang, Y. (2010). Evaluating post-transcriptional regulatory elements for enhancing transient gene expression levels in CHO K1 and HEK293 cells. Protein Expression and Purification *69*, 9-15.

57   Lim, S.M., Westover, K.D., Ficarro, S.B., Harrison, R.A., Choi, H.G., Pacold, M.E., Carrasco, M., Hunter, J., Kim, N.D., Xie, T.*, et al.* (2014). Therapeutic Targeting of Oncogenic K-Ras by a Covalent Catalytic Site Inhibitor. Angewandte Chemie International Edition *53*, 199-204.

58	Rudolph, J., and Stokoe, D. (2014). Selective Inhibition of Mutant Ras Protein through Covalent Binding. Angewandte Chemie International Edition *53*, 3777-3779.

59	Stephen, A.G., Esposito, D., Bagni, R.K., and McCormick, F. (2014). Dragging ras back in the ring. Cancer cell *25*, 272-281.

60	Grant, B.J., Lukman, S., Hocker, H.J., Sayyah, J., Brown, J.H., McCammon, J.A., and Gorfe, A.A. (2011). Novel allosteric sites on Ras for lead generation. PLoS One *6*, e25711.

61	Harrison J Hocker; Kwang-Jin Cho; Chung-Ying K Chen; Nandini Rambahal; Hui Chyn Wong; Sreenivasa Raso Sagineedu, K.S.J.S.J.F.H.A.A. (2013). Andrographolide derivative inhibit guanine nucleotide exchange and abrogate oncogenic Ras function: Prediction of direct Ras binding. Proc Natl Acad Sci U S A.

62	Prakash, P., Gorfe AA (2014). Overview of simulation studies on the enzymatic activity and conformational dynamics of the GTPase Ras. Molecular Simulation *40*, 9.

63	Prakash, P., and Gorfe, A.A. (2013). Lessons from computer simulations of Ras proteins in solution and in membrane. Biochimica et biophysica acta *1830*, 5211-5218.

64	Maurer, T., Garrenton, L.S., Oh, A., Pitts, K., Anderson, D.J., Skelton, N.J., Fauber, B.P., Pan, B., Malek, S., Stokoe, D.*, et al.* (2012). Small-molecule ligands bind to a distinct pocket in Ras and inhibit SOS-mediated nucleotide exchange activity. Proceedings of the National Academy of Sciences of the United States of America *109*, 5299-5304.

65	Ostrem, J.M., Peters, U., Sos, M.L., Wells, J.A., and Shokat, K.M. (2013). K-Ras(G12C) inhibitors allosterically control GTP affinity and effector interactions. Nature *advance online publication*.

66	Rosnizeck, I.C., Graf, T., Spoerner, M., Tränkle, J., Filchtinski, D., Herrmann, C., Gremer, L., Vetter, I.R., Wittinghofer, A., König, B.*, et al.* (2010). Stabilizing a Weak Binding State for Effectors in the Human Ras Protein by Cyclen Complexes. Angewandte Chemie International Edition *49*, 3830-3833.

67	Rosnizeck, I.C., Spoerner, M., Harsch, T., Kreitner, S., Filchtinski, D., Herrmann, C., Engel, D., Konig, B., and Kalbitzer, H.R. (2012). Metal-bis(2-picolyl)amine complexes as state

1(T) inhibitors of activated Ras protein. Angewandte Chemie (International ed in English) *51*, 10647-10651.

68   Shima, F., Yoshikawa, Y., Ye, M., Araki, M., Matsumoto, S., Liao, J., Hu, L., Sugimoto, T., Ijiri, Y., Takeda, A.*, et al.* (2013). In silico discovery of small-molecule Ras inhibitors that display antitumor activity by blocking the Ras–effector interaction. Proceedings of the National Academy of Sciences.

69   Sun, Q., Burke, J.P., Phan, J., Burns, M.C., Olejniczak, E.T., Waterson, A.G., Lee, T., Rossanese, O.W., and Fesik, S.W. (2012). Discovery of small molecules that bind to K-Ras and inhibit Sos-mediated activation. Angew Chem Int Ed Engl *51*, 6140-6143.

70   Buhrman, G., O'Connor, C., Zerbe, B., Kearney, B.M., Napoleon, R., Kovrigina, E.A., Vajda, S., Kozakov, D., Kovrigin, E.L., and Mattos, C. (2011). Analysis of Binding Site Hot Spots on the Surface of Ras GTPase. Journal of Molecular Biology *413*, 773-789.

71   Spiegel, J., Cromm, P.M., Zimmermann, G., Grossmann, T.N., and Waldmann, H. (2014). Small-molecule modulation of Ras signaling. Nature chemical biology *10*, 613-622.

72   Wang, W., Fang, G., and Rudolph, J. (2012). Ras inhibition via direct Ras binding—is there a path forward? Bioorganic & Medicinal Chemistry Letters *22*, 5766-5776.

73   Grant, B.J., Lukman, S., Hocker, H.J., Sayyah, J., Brown, J.H., McCammon, J.A., and Gorfe, A.A. (2011). Novel Allosteric Sites on Ras for Lead Generation. PloS one *6*.

74   Brenke, R., Kozakov, D., Chuang, G.Y., Beglov, D., Hall, D., Landon, M.R., Mattos, C., and Vajda, S. (2009). Fragment-based identification of druggable 'hot spots' of proteins using Fourier domain correlation techniques. Bioinformatics *25*, 621-627.

75   Shima, F., Yoshikawa, Y., Ye, M., Araki, M., Matsumoto, S., Liao, J., Hu, L., Sugimoto, T., Ijiri, Y., Takeda, A.*, et al.* (2013). In silico discovery of small-molecule Ras inhibitors that display antitumor activity by blocking the Ras-effector interaction. Proceedings of the National Academy of Sciences of the United States of America *110*, 8182-8187.

76   Rosnizeck, I.C., Graf, T., Spoerner, M., Trankle, J., Filchtinski, D., Herrmann, C., Gremer, L., Vetter, I.R., Wittinghofer, A., Konig, B.*, et al.* (2010). Stabilizing a weak binding state for

effectors in the human ras protein by cyclen complexes. Angewandte Chemie (International ed in English) *49*, 3830-3833.

77   Sun, Q., Burke, J.P., Phan, J., Burns, M.C., Olejniczak, E.T., Waterson, A.G., Lee, T., Rossanese, O.W., and Fesik, S.W. (2012). Discovery of Small Molecules that Bind to K-Ras and Inhibit Sos-Mediated Activation. Angew Chem Int Ed *51*, 6140-6143.

78   Ostrem, J.M., Peters, U., Sos, M.L., Wells, J.A., and Shokat, K.M. (2013). K-Ras(G12C) inhibitors allosterically control GTP affinity and effector interactions. Nature *503*, 548-+.

79   Ducker, G.S., Atreya, C.E., Simko, J.P., Hom, Y.K., Matli, M.R., Benes, C.H., Hann, B., Nakakura, E.K., Bergsland, E.K., Donner, D.B.*, et al.* (2014). Incomplete inhibition of phosphorylation of 4E-BP1 as a mechanism of primary resistance to ATP-competitive mTOR inhibitors. Oncogene *33*, 1590-1600.

80   Ostrem, J.M., and Shokat, K.M. (2016). Direct small-molecule inhibitors of KRAS: from structural insights to mechanism-based design. Nature reviews Drug discovery *15*, 771-785.

81   Dhawan, N.S., Scopton, A.P., and Dar, A.C. (2016). Small molecule stabilization of the KSR inactive state antagonizes oncogenic Ras signalling. Nature *537*, 112-116.

82   Hocker, H.J., Cho, K.J., Chen, C.Y., Rambahal, N., Sagineedu, S.R., Shaari, K., Stanslas, J., Hancock, J.F., and Gorfe, A.A. (2013). Andrographolide derivatives inhibit guanine nucleotide exchange and abrogate oncogenic Ras function. Proceedings of the National Academy of Sciences of the United States of America *110*, 10201-10206.

83   Prakash, P., Hancock, J.F., and Gorfe, A.A. (2015). Binding hotspots on K-Ras: consensus ligand binding sites and other reactive regions from probe-based molecular dynamics analysis. Proteins.

84   Scannell, J.W., Blanckley, A., Boldon, H., and Warrington, B. (2012). Diagnosing the decline in pharmaceutical R&D efficiency. Nature reviews Drug discovery *11*, 191-200.

85   Hung, C.L., and Chen, C.C. (2014). Computational approaches for drug discovery. Drug development research *75*, 412-418.

86   Grinter, S., and Zou, X. (2014). Challenges, Applications, and Recent Advances of Protein-Ligand Docking in Structure-Based Drug Design. Molecules *19*, 10150.

87   Lionta, E., Spyrou, G., Vassilatis, D.K., and Cournia, Z. (2014). Structure-based virtual screening for drug discovery: principles, applications and recent advances. Curr Top Med Chem *14*, 1923-1938.

88   Jelsch, C., Teeter, M.M., Lamzin, V., Pichon-Pesme, V., Blessing, R.H., and Lecomte, C. (2000). Accurate protein crystallography at ultra-high resolution: valence electron distribution in crambin. Proc Natl Acad Sci U S A *97*, 3171-3176.

89   Perot, S., Sperandio, O., Miteva, M.A., Camproux, A.C., and Villoutreix, B.O. (2010). Druggable pockets and binding site centric chemical space: a paradigm shift in drug discovery. Drug discovery today *15*, 656-667.

90   Sotriffer, C., and Klebe, G. (2002). Identification and mapping of small-molecule binding sites in proteins: computational tools for structure-based drug design. Farmaco *57*, 243-251.

91   Singla, P., Luxami, V., and Paul, K. (2015). Triazine-benzimidazole hybrids: anticancer activity, DNA interaction and dihydrofolate reductase inhibitors. Bioorganic & medicinal chemistry *23*, 1691-1700.

92   Dietrich, J., Hulme, C., and Hurley, L.H. (2010). The design, synthesis, and evaluation of 8 hybrid DFG-out allosteric kinase inhibitors: a structural analysis of the binding interactions of Gleevec, Nexavar, and BIRB-796. Bioorganic & medicinal chemistry *18*, 5738-5748.

93   Hardy, J.A., and Wells, J.A. (2004). Searching for new allosteric sites in enzymes. Curr Opin Struct Biol *14*, 706-715.

94   Dalpe, G., and Joly, Y. (2014). Opportunities and challenges provided by cloud repositories for bioinformatics-enabled drug discovery. Drug development research *75*, 393-401.

95   Braga, R.C., Alves, V.M., Silva, A.C., Nascimento, M.N., Silva, F.C., Liao, L.M., and Andrade, C.H. (2014). Virtual screening strategies in medicinal chemistry: the state of the art and current challenges. Curr Top Med Chem *14*, 1899-1912.

96   Zhang, X., Betzi, S., Morelli, X., and Roche, P. (2014). Focused chemical libraries--design and enrichment: an example of protein-protein interaction chemical space. Future Med Chem *6*, 1291-1307.

97   Lipinski, C.A., Lombardo, F., Dominy, B.W., and Feeney, P.J. (2001). Experimental and computational approaches to estimate solubility and permeability in drug discovery and development settings. Adv Drug Deliv Rev *46*, 3-26.

98   van de Waterbeemd, H., and Gifford, E. (2003). ADMET in silico modelling: towards prediction paradise? Nature reviews Drug discovery *2*, 192-204.

99   Doak, B.C., Over, B., Giordanetto, F., and Kihlberg, J. (2014). Oral druggable space beyond the rule of 5: insights from drugs and clinical candidates. Chem Biol *21*, 1115-1142.

100   Irwin, J.J., Sterling, T., Mysinger, M.M., Bolstad, E.S., and Coleman, R.G. (2012). ZINC: a free tool to discover chemistry for biology. Journal of chemical information and modeling *52*, 1757-1768.

101   Bolton, E.E., Chen, J., Kim, S., Han, L., He, S., Shi, W., Simonyan, V., Sun, Y., Thiessen, P.A., Wang, J.*, et al.* (2011). PubChem3D: a new resource for scientists. Journal of cheminformatics *3*, 32.

102   Plewczynski, D., Lazniewski, M., Augustyniak, R., and Ginalski, K. (2011). Can we trust docking results? Evaluation of seven commonly used programs on PDBbind database. Journal of computational chemistry *32*, 742-755.

103   Perola, E., Walters, W.P., and Charifson, P.S. (2004). A detailed comparison of current docking and scoring methods on systems of pharmaceutical relevance. Proteins *56*, 235-249.

104   Cosconati, S., Forli, S., Perryman, A.L., Harris, R., Goodsell, D.S., and Olson, A.J. (2010). Virtual Screening with AutoDock: Theory and Practice. Expert opinion on drug discovery *5*, 597-607.

105   Chang, M.W., Ayeni, C., Breuer, S., and Torbett, B.E. (2010). Virtual screening for HIV protease inhibitors: a comparison of AutoDock 4 and Vina. PLoS One *5*, e11955.

106   Morris, G.M., Huey, R., Lindstrom, W., Sanner, M.F., Belew, R.K., Goodsell, D.S., and Olson, A.J. (2009). AutoDock4 and AutoDockTools4: Automated docking with selective receptor flexibility. Journal of computational chemistry *30*, 2785-2791.

107   Morris, G.M., Goodsell, D.S., Halliday, R.S., Huey, R., Hart, W.E., Belew, R.K., and Olson, A.J. (1998). Automated docking using a Lamarckian genetic algorithm and an empirical binding free energy function. Journal of computational chemistry *19*, 1639-1662.

108   Cecchini, M., Kolb, P., Majeux, N., and Caflisch, A. (2004). Automated docking of highly flexible ligands by genetic algorithms: a critical assessment. Journal of computational chemistry *25*, 412-422.

109   Kitchen, D.B., Decornez, H., Furr, J.R., and Bajorath, J. (2004). Docking and scoring in virtual screening for drug discovery: methods and applications. Nature reviews Drug discovery *3*, 935-949.

110   Gray, J.J., Moughon, S., Wang, C., Schueler-Furman, O., Kuhlman, B., Rohl, C.A., and Baker, D. (2003). Protein-protein docking with simultaneous optimization of rigid-body displacement and side-chain conformations. J Mol Biol *331*, 281-299.

111   Salam, N.K., Nuti, R., and Sherman, W. (2009). Novel method for generating structure-based pharmacophores using energetic analysis. Journal of chemical information and modeling *49*, 2356-2368.

112   Yang, H., Zhou, Q., Li, B., Wang, Y., Luan, Z., Qian, D., and Li, H. (2010). GPU acceleration of Dock6's Amber scoring computation. Advances in experimental medicine and biology *680*, 497-511.

113   Wang, R., Lu, Y., and Wang, S. (2003). Comparative evaluation of 11 scoring functions for molecular docking. Journal of medicinal chemistry *46*, 2287-2303.

114   Scior, T., Bender, A., Tresadern, G., Medina-Franco, J.L., Martinez-Mayorga, K., Langer, T., Cuanalo-Contreras, K., and Agrafiotis, D.K. (2012). Recognizing pitfalls in virtual screening: a critical review. Journal of chemical information and modeling *52*, 867-881.

115   Plowman, S.J., Ariotti, N., Goodall, A., Parton, R.G., and Hancock, J.F. (2008). Electrostatic interactions positively regulate K-Ras nanocluster formation and function. Molecular and cellular biology *28*, 4377-4385.

116   Neal, S.E., Eccleston, J.F., Hall, A., and Webb, M.R. (1988). Kinetic Analysis of the Hydrolysis of GTP by p21 N-Ras. J Bio Chem *263*, 19717-19722.

117   Hunter, J.C., Manandhar, A., Carrasco, M.A., Gurbani, D., Gondi, S., and Westover, K.D. (2015). Biochemical and Structural Analysis of Common Cancer-Associated KRAS Mutations. Molecular cancer research : MCR *13*, 1325-1335.

118   Maurer, T., Garrenton, L.S., Oha, A., Pitts, K., Anderson, D.J., Skelton, N.J., Fauber, B.P., Pan, B., Malek, S., Stokoe, D.*, et al.* (2012). Small-molecule ligands bind to a distinct pocket in Ras and inhibit SOS-mediated nucleotide exchange activity. Proceedings of the National Academy of Sciences of the United States of America *109*, 5299-5304.

119   Sayyed-Ahmad, A., Prakash, P., and Gorfe, A.A. (2017). Distinct dynamics and interaction patterns in H- and K-Ras oncogenic P-loop mutants. Proteins *85*, 1618-1632.

120   Irwin, J.J., Sterling, T., Mysinger, M.M., Bolstad, E.S., and Coleman, R.G. (2012). ZINC: A Free Tool to Discover Chemistry for Biology. J Chem Inf Model *52*, 1757-1768.

121   Mott, H.R., and Owen, D. (2015). Structures of Ras superfamily effector complexes: What have we learnt in two decades? Crit Rev Biochem Mol Biol *50*, 85-133.

122   Zhang, S., Kumar, K., Jiang, X., Wallqvist, A., and Reifman, J. (2008). DOVIS: an implementation for high-throughput virtual screening using AutoDock. BMC Bioinformatics *9*, 126.

123   Trott, O., and Olson, A.J. (2010). AutoDock Vina: improving the speed and accuracy of docking with a new scoring function, efficient optimization, and multithreading. Journal of computational chemistry *31*, 455-461.

124   Durrant, J.D., and McCammon, J.A. (2011). BINANA: a novel algorithm for ligand-binding characterization. J Mol Graph Model *29*, 888-893.

125   Clayton, A.H., Hanley, Q.S., and Verveer, P.J. (2004). Graphical representation and multicomponent analysis of single-frequency fluorescence lifetime imaging microscopy data. Journal of microscopy *213*, 1-5.

126   Verveer, P.J., and Bastiaens, P.I.H. (2003). Evaluation of global analysis algorithms for single frequency fluorescence lifetime imaging microscopy data. Journal of microscopy *209*, 1-7.

127   Esposito, A., Gerritsen, H.C., and Wouters, F.S. (2005). Fluorescence lifetime heterogeneity resolution in the frequency domain by lifetime moments analysis. Biophys J *89*, 4286-4299.

128   Burns, M.C., Sun, Q., Daniels, R.N., Camper, D., Kennedy, J.P., Phan, J., Olejniczak, E.T., Lee, T., Waterson, A.G., Rossanese, O.W.*, et al.* (2014). Approach for targeting Ras with small molecules that activate SOS-mediated nucleotide exchange. Proceedings of the National Academy of Sciences of the United States of America *111*, 3401-3406.

129   Gremer, L., Merbitz-Zahradnik, T., Dvorsky, R., Cirstea, I.C., Kratz, C.P., Zenker, M., Wittinghofer, A., and Ahmadian, M.R. (2011). Germline KRAS mutations cause aberrant biochemical and physical properties leading to developmental disorders. Hum Mutat *32*, 33-43.

130   Nakhaeizadeh, H., Amin, E., Nakhaei-Rad, S., Dvorsky, R., and Ahmadian, M.R. (2016). The RAS-Effector Interface: Isoform-Specific Differences in the Effector Binding Regions. PloS one *11*, e0167145.

131   Sarkar-Banerjee, S., Sayyed-Ahmad, A., Prakash, P., Cho, K.J., Waxham, M.N., Hancock, J.F., and Gorfe, A.A. (2017). Spatiotemporal Analysis of K-Ras Plasma Membrane Interactions Reveals Multiple High Order Homo-oligomeric Complexes. J Am Chem Soc *139*, 13466-13475.

132   Singh, H., Longo, D.L., and Chabner, B.A. (2015). Improving Prospects for Targeting RAS. Journal of clinical oncology : official journal of the American Society of Clinical Oncology *33*, 3650-3659.

133   Grant, B.J., Gorfe, A.A., and McCammon, J.A. (2010). Large conformational changes in proteins: signaling and other functions. Curr Opin Struct Biol *20*, 142-147.

134   Spiegel, J., Cromm, P.M., Zimmermann, G., Grossmann, T.N., and Waldmann, H. (2014). Small-molecule modulation of Ras signaling. Nat Chem Biol *10*, 613-622.

135   Xie, C., Li, Y., Li, L.L., Fan, X.X., Wang, Y.W., Wei, C.L., Liu, L., Leung, E.L., and Yao, X.J. (2017). Identification of a New Potent Inhibitor Targeting KRAS in Non-small Cell Lung Cancer Cells. Frontiers in pharmacology *8*, 823.

136   Rudolph, J., and Stokoe, D. (2014). Selective inhibition of mutant Ras protein through covalent binding. Angewandte Chemie (International ed in English) *53*, 3777-3779.

137   Trinh, T.B., Upadhyaya, P., Qian, Z., and Pei, D. (2016). Discovery of a Direct Ras Inhibitor by Screening a Combinatorial Library of Cell-Permeable Bicyclic Peptides. ACS Comb Sci *18*, 75-85.

138   Upadhyaya, P., Qian, Z., Habir, N.A., and Pei, D. (2014). Direct Ras Inhibitors Identified from a Structurally Rigidified Bicyclic Peptide Library. Tetrahedron *70*, 7714-7720.

139   Phillips, J.C., Braun, R., Wang, W., Gumbart, J., Tajkhorshid, E., Villa, E., Chipot, C., Skeel, R.D., Kale, L., and Schulten, K. (2005). Scalable molecular dynamics with NAMD. Journal of computational chemistry *26*, 1781-1802.

140   MacKerell, A.D., Bashford, D., Bellott, M., Dunbrack, R.L., Evanseck, J.D., Field, M.J., Fischer, S., Gao, J., Guo, H., Ha, S.*, et al.* (1998). All-atom empirical potential for molecular modeling and dynamics studies of proteins. Journal of Physical Chemistry B *102*, 3586-3616.

141   Schmidtke, P., Bidon-Chanal, A., Luque, J., and Barril, X. MDpocket : Open Source Cavity Detection and Characterization on Molecular Dynamics Trajectories. Bioinformatics.

142   Jiang, X., Kumar, K., Hu, X., Wallqvist, A., and Reifman, J. (2008). DOVIS 2.0: an efficient and easy to use parallel virtual screening tool based on AutoDock 4.0. Chem Cent J *2*, 18.

143   Ghemtio, L., Perez-Nueno, V.I., Leroux, V., Asses, Y., Souchet, M., Mavridis, L., Maigret, B., and Ritchie, D.W. (2012). Recent Trends and Applications in 3D Virtual Screening. Comb Chem High Throughput Screen *15*, 749-769.

144   Morris, G.M., Huey, R., Lindstrom, W., Sanner, M.F., Belew, R.K., Goodsell, D.S., and Olson, A.J. (2009). AutoDock4 and AutoDockTools4: Automated Docking with Selective Receptor Flexibility. Journal of computational chemistry *30*, 2785-2791.

145   Seeliger, D., and de Groot, B.L. (2010). Ligand docking and binding site analysis with PyMOL and Autodock/Vina. J Comput Aided Mol Des *24*, 417-422.

146   Paul Polakis, F.M. (1993). Structural Requirements for the Interaction of p21 RAS with GAP, Exchange Factors, and Its Biological Effector Targets. J Bio Chem *268*, 9157-9160.

147   Calabrese, E.J. (2005). Cancer biology and hormesis: human tumor cell lines commonly display hormetic (biphasic) dose responses. Critical reviews in toxicology *35*, 463-582.

148   Zhou, Y., and Hancock, J.F. (2015). Ras nanoclusters: Versatile lipid-based signaling platforms. Biochimica et biophysica acta *1853*, 841-849.

149   Fetics, S.K., Guterres, H., Kearney, B.M., Buhrman, G., Ma, B., Nussinov, R., and Mattos, C. (2015). Allosteric effects of the oncogenic RasQ61L mutant on Raf-RBD. Structure *23*, 505-516.

150   Vo, U., Vajpai, N., Flavell, L., Bobby, R., Breeze, A.L., Embrey, K.J., and Golovanov, A.P. (2016). Monitoring Ras Interactions with the Nucleotide Exchange Factor Son of Sevenless (Sos) Using Site-specific NMR Reporter Signals and Intrinsic Fluorescence. The Journal of biological chemistry *291*, 1703-1718.

151   Iversen, L., Tu, H.L., Lin, W.C., Christensen, S.M., Abel, S.M., Iwig, J., Wu, H.J., Gureasko, J., Rhodes, C., Petit, R.S.*, et al.* (2014). Molecular kinetics. Ras activation by SOS: allosteric regulation by altered fluctuation dynamics. Science *345*, 50-54.

152   Allen, N.P., Donninger, H., Vos, M.D., Eckfeld, K., Hesson, L., Gordon, L., Birrer, M.J., Latif, F., and Clark, G.J. (2007). RASSF6 is a novel member of the RASSF family of tumor suppressors. Oncogene *26*, 6203-6211.

153   Overmeyer, J.H., and Maltese, W.A. (2011). Death pathways triggered by activated Ras in cancer cells. Frontiers in bioscience (Landmark edition) *16*, 1693-1713.

154   Pacold, M.E., Suire, S., Perisic, O., Lara-Gonzalez, S., Davis, C.T., Walker, E.H., Hawkins, P.T., Stephens, L., Eccleston, J.F., and Williams, R.L. (2000). Crystal structure and functional analysis of Ras binding to its effector phosphoinositide 3-kinase gamma. Cell *103*, 931-943.

155   Chen, P., Deng, Y.L., Bergqvist, S., Falk, M.D., Liu, W., Timofeevski, S., and Brooun, A. (2014). Engineering of an isolated p110alpha subunit of PI3Kalpha permits crystallization and provides a platform for structure-based drug design. Protein science : a publication of the Protein Society *23*, 1332-1340.

156   Margarit, S.M., Sondermann, H., Hall, B.E., Nagar, B., Hoelz, A., Pirruccello, M., Bar-Sagi, D., and Kuriyan, J. (2003). Structural evidence for feedback activation by Ras.GTP of the Ras-specific nucleotide exchange factor SOS. Cell *112*, 685-695.

Vita

Michael Jonathann McCarthy was born in Detroit, Michigan on September 12th, the son of Catherine McCarthy and Edmund McCarthy. He received a Bachelor of Science in biochemistry from Oakland University in Rochester, Michigan in 2009. For the next year he worked as a teaching assistant at Oakland University. In September 2011 he entered The Unversity of Texas Health Science Center in Houston and MD Anderson Cancer Center as a master student. He received his Master of Science degree in biomedical sciences in August 2013. In August 2013 he entered The Unversity of Texas Health Science Center in Houston & MD Anderson Cancer Center and joined the Department of Integrative Biology and Pharmacology as a Ph.D. student. In 2015 he married Kathryn Beabout a Ph.D. student at Rice University. In 2018 he graduated from The Unversity of Texas Health Science Center in Houston and MD Anderson Cancer Center. He joined the Henry M. Jackson foundation in March 2018 with a position at Wright Patterson Air Force Base as a Biomedical Scientist.